SURFACE PLASMON OPTIMIZATION FOR PHOTOCURRENT ENHANCEMENT IN THIN FILM ORGANIC SOLAR CELLS

OPTIMISATION DES PLASMONS DE SURFACE POUR L'AMÉLIORATION DE PHOTOCOURANT DANS LES CELLULES SOLAIRES ORGANIQUES EN COUCHES MINCES

A Thesis Submitted

to the Division of Graduate Studies of the Royal Military College of Canada

by

Justin Jefferies, BEng
Captain

In Partial Fulfillment of the Requirements for the Degree of

Master's of Physics

22 May 2012

© This thesis may be used within the Department of National Defence but copyright for open publication remains the property of the author.

Library and Archives Canada

Published Heritage Branch

395 Wellington Street
Ottawa ON K1A 0N4
Canada

Bibliothèque et Archives Canada

Direction du Patrimoine de l'édition

395, rue Wellington
Ottawa ON K1A 0N4
Canada

Your file Votre référence
ISBN: 978-0-494-89350-0

Our file Notre référence
ISBN: 978-0-494-89350-0

NOTICE:

The author has granted a non-exclusive license allowing Library and Archives Canada to reproduce, publish, archive, preserve, conserve, communicate to the public by telecommunication or on the Internet, loan, distrbute and sell theses worldwide, for commercial or non-commercial purposes, in microform, paper, electronic and/or any other formats.

The author retains copyright ownership and moral rights in this thesis. Neither the thesis nor substantial extracts from it may be printed or otherwise reproduced without the author's permission.

AVIS:

L'auteur a accordé une licence non exclusive permettant à la Bibliothèque et Archives Canada de reproduire, publier, archiver, sauvegarder, conserver, transmettre au public par télécommunication ou par l'Internet, prêter, distribuer et vendre des thèses partout dans le monde, à des fins commerciales ou autres, sur support microforme, papier, électronique et/ou autres formats.

L'auteur conserve la propriété du droit d'auteur et des droits moraux qui protege cette thèse. Ni la thèse ni des extraits substantiels de celle-ci ne doivent être imprimés ou autrement reproduits sans son autorisation.

In compliance with the Canadian Privacy Act some supporting forms may have been removed from this thesis.

While these forms may be included in the document page count, their removal does not represent any loss of content from the thesis.

Conformément à la loi canadienne sur la protection de la vie privée, quelques formulaires secondaires ont été enlevés de cette thèse.

Bien que ces formulaires aient inclus dans la pagination, il n'y aura aucun contenu manquant.

Canada

This is to certify that the thesis prepared by

Ceci certifie que le mémoire/la thèse rédigé(e) par

JUSTIN JEFFERIES

entitled

Intitulée

SURFACE PLASMON OPTIMIZATION FOR PHOTOCURRENT ENHANCEMENT IN THIN FILM ORGANIC SOLAR CELLS

OPTIMISATION DES PLASMONS DE SURFACE POUR L'AMÉLIORATION DE PHOTOCOURANT DANS LES CELLULES SOLAIRES ORGANIQUE EN COUCHES MINCES

complies with the Royal Military College of Canada regulations and that it meets the accepted standards of the Graduate School with respect to quality and originality for the degree of

satisfait aux règlements du Collège militaire royal du Canada et qu'il (elle) respecte les normes acceptées par la Division des études supérieures quant à la qualité et l'originalité pour le grade universitaire de

Master of Science (MSc)

Maîtrise en sciences (M. Sc.)

The original sheet was signed on the 22 May 2012 by the members of the Oral Defence Thesis Examination Committee.

La feuille originale a été signée le 15 août 2012 par les membres du Comité de l'examen oral du mémoire/de thèse.

Chair / Président

Examiner External to RMC / Examinateur externe au CMR

Examiner External to the department and internal to RMC / Examinateur externe au département et interne au CMR

Examiner Internal to the department / Examinateur interne au département

---

Supervisor(s) / Directeur(s) du mémoire/de thèse

Thesis is approved by the Head of Department / Le mémoire/la thèse est approuvé(e) par le directeur du département

To the Librarian:
This thesis is not to be regarded as classified.
Au/À la bibliothécaire :
Ce mémoire/cette thèse n'est pas considéré(e) comme publication restreinte.

Main Supervisor of thesis /
Directeur principal de thèse/du mémoire

To my wife, Courtney and our two daughters, Siena and Adley.

Thank you for your endless love and support.

ACKNOWLEDGEMENTS

I would like to thank my thesis advisor, Dr. Georges Sabat, for his guidance and support throughout this thesis. His counsel and enthusiasm provided a continual source of focus and motivation. I consider him to be not only a great teacher and mentor, but also a friend.

I would also like to thank Dr. Luc Levesque and Dr. Paul Rochon for entertaining my many queries and engaging in discussions on related subject matter. I express much gratitude for their patience and expert insight.

To my office mate, 2Lt Maxime Bernier-Brideau, for being a willing sounding board to my many ideas and explanations. It was a pleasure studying and socializing with him, and I wish him nothing but the best throughout his promising military career.

Finally, I would like to thank Mr. Steve Lockridge and Mr. Dave Watts for their technical support. Their noble efforts enable science, and are certainly appreciated.

ABSTRACT

Jefferies, JG; M.Sc (Physics); Royal Military College of Canada; May 2012; Surface Plasmon Optimization for Photocurrent Enhancement in Thin Film Organic Solar Cells; Supervisor: Dr. R.G. Sabat.

Surface plasmons (SPs) are a light induced phenomenon resulting in desirable electromagnetic (EM) field enhancements concentrated at the surface of an appropriate dielectric-metal interface. One of the most promising applications of these SPs exists in the world of photovoltaics (PV), more specifically in organic solar cells (OSCs). By exploiting SPs at the polymer-electrode interface of an OSC, enhanced photocurrent can be generated around the wavelength(s) satisfying the SP resonance conditions.

Methodical and intensive SP excitation trials were carried out on various, non-PV, dielectric-metal interfaces in order to examine and evaluate SP behaviour. The SPs were optically excited via the diffraction grating method using single, crossed and parallel grating schemes, with trials yielding optimal grating and film thickness parameters. These optimal parameters were applied to the design and fabrication of SP-based, poly (3-hexylthiophene) (P3HT):[6,6]-phenyl C_{61}-butyric (PCBM) OSCs.

A single, P3HT:PCBM layer was sandwiched between two harvesting electrodes, with aluminum (Al) being used at the bottom, and gold (Au) being used at the top. The Al electrode doubled as an excitation grating. Optical scans of varying parameters were carried out on all samples, with photocurrent enhancements up to 364% being demonstrated. Enhancements for transverse magnetic (TM) polarized incident light were present on single and parallel grating structures, and similar enhancements for both TM

and transverse electric (TE) polarized incident light were present on crossed grating structures.

When compared to the photocurrent enhancements seen on single grating structures, those seen on parallel gratings were comparable in magnitude, but shown over a much broader optical band. This broadening of the optical band was centered on the theoretical SP resonance peak of the second grating contained within the parallel scheme.

RÉSUMÉ

Jefferies, JG; M.Sc (Physique); Collège militaire royal du Canada; mai 2012; Optimisation des plasmons de surface pour l'amélioration de photocourant dans les cellules solaires organiques en couches minces; Superviseur: Dr. RG Sabat.

Les plasmons de surface (PS) est un phénomène de résonance de la lumière résultant en des améliorations souhaitables dans la concentration des champs électromagnétiques à l'interface entre un diélectrique et un métal. Une des applications les plus prometteuses de ces PS existe dans le monde de l'énergie photovoltaïque (PV), et plus précisément dans les cellules solaires organiques (CSO). En exploitant les PS à l'interface polymère-électrode d'un CSO, une augmentation du photocourant généré peut être obtenue dans la gamme de longueurs d'onde satisfaisant les conditions de résonance du PS.

Des essais méthodiques et intensifs sur les PS ont été effectués sur diverses interfaces diélectrique-métal afin d'examiner et d'évaluer le comportement des PS. Les PS ont été optiquement excités avec des réseaux de diffraction simples, croisés et parallèles, afin d'identifier les paramètres optimaux pour la génération des PS dans les cellules photovoltaïques. Ces paramètres optimaux ont été appliqués à la conception et la fabrication des CSO basées sur le polymère (3-hexylthiophène) (P3HT): [6,6]-phényl C61-butyrique (PCBM).

Une couche de P3HT: PCBM a été mise en sandwich entre deux électrodes de récolte. L'aluminium (Al) était utilisé à la base, tandis que l'or (Au) était utilisé dans la partie supérieure de la cellule solaire. L'électrode Al a été mise par-dessus les réseaux de diffraction pour générer les PS. Des balayages optiques de paramètres variables ont été

effectués sur tous les échantillons, avec des améliorations de photocourant attenant à un maximum de 364%. Des améliorations pour une lumière incidente polarisée transverse magnétique (TM) étaient présentes sur les structures de réseau simples et parallèles, et des améliorations similaires pour les lumières incidente polarisées TM et transverse électrique (TE) étaient présentes sur les structures de réseaux croisées.

Lorsque comparées à des améliorations de photocourant vues sur les structures de réseaux simples, celles observées sur les réseaux parallèles étaient d'une ampleur comparable, mais sur une bande optique beaucoup plus large. Cet élargissement de la bande optique a été centré sur le pic du PS théorique du second réseau dans le système de réseaux parallèles.

TABLE OF CONTENTS

DEDICATION		I
ACKNOWLEDGEMENTS		II
ABSTRACT		III
RÉSUMÉ		V
TABLE OF CONTENTS		VII
LIST OF TABLES		X
LIST OF FIGURES		XI
LIST OF ABREVIATIONS AND SYMBOLS		XIII
CHAPTER 1 – INTRODUCTION		1
1.1	Definitions, Properties and Excitation Methods	1
1.2	Early History	4
1.3	General Applications	6
1.4	Photovoltiac Applications	8
1.5	Goal of Research	10
1.6	Thesis Structure	12
References		14
CHAPTER 2 – THEORY		21
2.1	Electro-Magnetic Fundamentals	21
2.1.1	Light as an Electro-Magnetic Plane Wave	21
2.1.2	Maxwell's Equations and Dielectric Permittivity	23
2.1.3	Classification of Media	24
2.1.4	Polarization of Light	25
2.1.5	Mathematical Description of Light	27
2.2.	Light at a Boundary	28
2.2.1	Laws of Reflection and Refraction	28
2.2.2	Fresnel Equations for TM and TE Polarized Light	31
2.3.	Diffraction of Light	34
2.3.1	Irradiance, Superposition and Interference of Light	34
2.3.2	Single-Slit Diffraction	35
2.3.3	Multiple-Slit Diffraction	38
2.3.4	Diffraction Gratings and the Grating Equation	41

2.4. Surface Plasmon Grating Excitation 45
2.4.1 Mathematical Description of Surface Plasmons 45
2.4.2 Surface Plasmon Dispersion Relation 47
2.4.3 Drude Model for Dielectric Permittivity 50
2.4.4 Surface Plasmon Dispersion Curve 51
2.4.5 Surface Plasmon Excitation Condition 53
References 56
CHAPTER 3 – SURFACE PLASMON OPTIMIZATION 59
3.1. Test Sample Fabrication Process 59
3.1.1. Azopolymers and Grating Inscription 59
3.1.2. Grating Verification and Considerations 62
3.1.3. Dielectric-Metal Interface 66
3.2. Test Sample Analysis 68
3.2.1. Test Sample Analysis Apparatus 68
3.2.2. Test Sample Irradiance Response 70
3.3. Analysis of an Air-Silver Interface 71
3.3.1. Single Grating Air-Silver Interface 71
3.3.2. Crossed Grating Air-Silver Interface 78
3.3.3. Parallel Grating Air-Silver Interface 84
3.4. Analysis of a Polyvinyl Alcohol-Silver Interface 90
3.4.1. Single Grating Polyvinyl Alcohol-Silver Interface 90
3.4.2. Crossed Grating Polyvinyl Alcohol-Silver Interface 94
3.4.1. Parallel Grating Polyvinyl Alcohol-Silver Interface 100
References 104
CHAPTER 4 –THIN FILM ORGANIC SOLAR CELLS 105
4.1. Organic Solar Cell Fabrication Process 105
4.1.1. Grating Inscription and Verification 105
4.1.2. Metal Deposits 106
4.1.3. P3HT:PCBM Photoactive Blend 107
4.1.4. Organic Solar Cell Architecture 108
4.2. Organic Solar Cell Analysis 109
4.2.1. Organic Solar Cell Analysis Apparatus 109
4.2.2. Organic Solar Cell Photocurrent Response 110
4.2.3. Single Grating Analysis 111

4.2.4. Crossed Grating Analysis 116
4.2.3. Parallel Grating Analysis 118
References 124
CHAPTER 5 – CONCLUSION 127
References 130
BIBLIOGRAPHY 131
CURRICULUM VITAE 133

LIST OF TABLES

Chapter 3

Table 3.1	Theoretical and experimental comparison of λ_{SP} at $\theta_i = 0$.	72
Table 3.2	PVA thin film parameters.	91

LIST OF FIGURES

Chapter 1

Figure 1.1	Evanescent field of a SP at a dielectic-metal interface.	2
Figure 1.2	SP excitation configurations.	3
Figure 1.3	Architecture of a basic SC.	9

Chapter 2

Figure 2.1	EM plane wave propagating in the x-direction.	22
Figure 2.2	Transverse EM plane wave propagating in the x-direction.	22
Figure 2.3	Loss angle of a lossy medium.	25
Figure 2.4	Linearly polarized light.	26
Figure 2.5	Right-circularly polarized light.	27
Figure 2.6	Light at a boundary as (a) a single ray and (b) successive rays.	29
Figure 2.7	TM polarized light at a boundary.	32
Figure 2.8	TE polarized light at a boundary	33
Figure 2.9	Single-slit geometry.	36
Figure 2.10	Single-slit diffraction pattern.	38
Figure 2.11	Double-slit diffraction geometry.	38
Figure 2.12	Double-slit diffraction pattern (a) separated and (b) combined.	39
Figure 2.13	Four-slit diffraction pattern.	41
Figure 2.14	Diffraction of light using both reflective and transmissive gratings.	42
Figure 2.15	Successive element reflective grating geometry.	42
Figure 2.16	Schematic of the grating equation in light momentum space.	44
Figure 2.17	TM polarized incident light on a dielectric-metal interface at y = 0.	46
Figure 2.18	Relative dielectric permittivity plot for a dielectric and a metal.	51
Figure 2.19	SP dispersion relation plot.	52
Figure 2.20	SP excitation matching condition plot.	55

Chapter 3

Figure 3.1	Overview of grating inscription apparatus.	60
Figure 3.2	Overview of rotating sample mount.	61
Figure 3.3	Overview of grating spacing verification apparatus.	62
Figure 3.4	Single grating ($\Lambda \approx 640$ nm) in (a) 2-D and (b) 3-D.	63
Figure 3.5	Crossed grating ($\Lambda_{TM} = \Lambda_{TE} \approx 640$ nm) in (a) 2-D and (b) 3-D.	64
Figure 3.6	Parallel grating ($\Lambda_1 \approx 280$ nm, $\Lambda_2 \approx 240$ nm) in (a) 2-D and (b) 3-D.	65
Figure 3.7	Single grating ($\Lambda \approx 640$ nm) sputtered with Ag in (a) 2-D and (b) 3-D.	66
Figure 3.8	Architecture of an air-Ag test sample.	67
Figure 3.9	Architecture of a PVA-Ag test sample.	68
Figure 3.10	Overview of test sample analytical set-up.	69
Figure 3.11	Side view of test sample analytical set-up for circled stage.	69
Figure 3.12	Relative irradiance response due to SP excitation.	70
Figure 3.13	SPs at an air-Ag interface at $\theta_i = 0$ for varied grating spacing.	71

Figure 3.14 SPs at an air-Ag interface at $\theta_i = 0$ for varied grating depths. 73
Figure 3.15 SPs at a single grating air-Ag interface for varied θ_i. 74
Figure 3.16 SPs at a single grating air-Ag interface for varied θ_i contour. 75
Figure 3.17 SPs at a single grating air-Ag interface for varied θ_i colour. 76
Figure 3.18 Explanation of zones (a) 1, (b) 2 and (c) 3 as highlighted in figure 3.17. 77
Figure 3.19 TM SPs at a crossed grating air-Ag interface for varied θ_i. 79
Figure 3.20 TM SPs at a crossed grating air-Ag interface for varied θ_i contour. 80
Figure 3.21 TM SPs at a crossed grating air-Ag interface for varied θ_i colour. 81
Figure 3.22 TE SPs at a crossed grating air-Ag interface for varied θ_i. 82
Figure 3.23 TE SPs at a crossed grating air-Ag interface for varied θ_i contour. 83
Figure 3.24 TE SPs at a crossed grating air-Ag interface for varied θ_i colour. 84
Figure 3.25 SPs at a parallel grating air-Ag interface for varied θ_i. 85
Figure 3.26 SPs at a parallel grating air-Ag interface for varied θ_i contour. 87
Figure 3.27 SPs at a parallel grating air-Ag interface for varied θ_i colour. 88
Figure 3.28 Parallel grating SP excitation plot. 90
Figure 3.29 SPs at a PVA-Ag interface at $\theta_i = 0$ for varied film thicknesses. 92
Figure 3.30 SP $\vec{E}$-field decay into the dielectric, δ_d. 93
Figure 3.31 TM SPs at a crossed grating PVA-Ag interface for varied θ_i. 95
Figure 3.32 TM SPs at a crossed grating PVA-Ag interface for varied θ_i contour. 96
Figure 3.33 TM SPs at a crossed grating PVA-Ag interface for varied θ_i colour. 97
Figure 3.34 TE SPs at a crossed grating PVA-Ag interface for varied θ_i. 98
Figure 3.35 TE SPs at a crossed grating PVA-Ag interface for varied θ_i contour. 99
Figure 3.36 TE SPs at a crossed grating PVA-Ag interface for varied θ_i colour. 100
Figure 3.37 SPs at a parallel grating PVA-Ag interface for varied θ_i. 101
Figure 3.38 SPs at a parallel grating air-Ag interface for varied θ_i. 102
Figure 3.39 SPs at a parallel grating air-Ag interface for varied θ_i colour. 103

Chapter 4

Figure 4.1 Dimensions of metal deposit. 106
Figure 4.2 P3HT:PCBM bulk hetero-junction blend. 108
Figure 4.3 Architecture of a SP-based, P3HT-PCBM OSC. 109
Figure 4.4 Overview of OSC analytical set-up. 110
Figure 4.5 Photocurrent response of a single grating, P3HT:PCBM OSC at $\theta_i = 0$. 112
Figure 4.6 Relative photocurrent response at $\theta_i = 0$ for single grating spacings. 113
Figure 4.7 Photocurrent response of a single grating OSC for varied θ_i. 115
Figure 4.8 Photocurrent response of a crossed grating OSC at $\theta_i = 0$. 117
Figure 4.9 Relative photocurrent response of a crossed grating OSC. 118
Figure 4.10 Photocurrent response of a parallel grating, P3HT:PCBM OSC. 119
Figure 4.11 Relative photocurrent response at $\theta_i = 0$ for a single versus parallel OSC. 120
Figure 4.12 Photocurrent response of a single versus parallel grating OSC. 121
Figure 4.13 Relative photocurrent response of a single versus parallel grating OSC. 122

LIST OF ABBREVIATIONS AND SYMBOLS

2-D	two-dimensional
3-D	three-dimensional
A	amperes
AFM	atomic force microscope
Ag	silver
Al	aluminum
AM	air mass
Au	gold
BK7	borosilicate crown glass
c	speed of light in free-space
CCW	counterclockwise
cm	centimeter
CO_2	carbon dioxide
CW	clockwise
DNA	deoxyribonucleic acid
δ_d	dielectric 1/e decay length
δ_m	metal 1/e decay length
δ_{SP}	surface plasmon propagation length
E	energy
$\vec{E}$	electric field vector
EM	electromagnetic
$\vec{E}_o$	electric field amplitude vector
ε	dielectric permittivity
ε_o	permittivity of free-space
ε_r	relative dielectric permittivity
$\tilde{\varepsilon}$	effective dielectric permittivity
f	frequency
φ	phase of a plane wave
h	Planck's constant
$\vec{H}$	magnetic field vector
I	irradiance
IR	infrared
k	wave number of light
K	grating vector
$\vec{k}$	wave vector of light
k_o	wave number of light in free-space
LED	light emitting diodes
λ	wavelength of light
λ_o	wavelength of light in free space
λ_{SP}	surface plasmon excitation wavelength
Λ	grating spacing
m	order of diffraction
μ	magnetic permeability

μm	micrometer
μ_o	permeability of free-space
μ_r	relative magnetic permeability
n	refractive index
N_2	nitrogen
nm	nanometer
O_2	oxygen
OSC	organic solar cell
Ω	ohm
P3HT:PCBM	poly (3-hexylthiophene):[6,6]-phenyl C_{61}-butyric
pDR1M	poly[4-nitrophenyl-4′-[[2-(methacryloyloxy)ethyl]ethyl-amino]phenyldiazene]
PV	photovoltaic
PVA	polyvinyl alcohol
r	Fresnel reflection coefficient
R	resistance
$\vec{r}$	position vector
RPM	revolution per minute
ρ	resistivity
SC	solar cell
secs	seconds
SP	surface plasmon
σ	conductivity
t	Fresnel transmission coefficient
TE	transverse electric
TM	transverse magnetic
θ_c	critical angle
θ_m	angle of diffraction
UV	ultraviolet
v	speed of light
W	watts
$W \cdot m^{-2}$	watts per meter squared
ω	angular frequency
ω_p	plasma angular frequency

CHAPTER 1: INTRODUCTION

1.1 Definitions, Properties and Excitation Methods

A metal can be described as an arrangement of fixed, positive ions surrounded by dense, delocalized, free electron clouds, resulting in desirable conductivity [1]. These free electron clouds can be viewed as plasma [2] – a collection of charged particles taking the form of gas-like clouds which respond strongly and collectively to electromagnetic (EM) fields [3]. If one were to subject a piece of metal to an external EM field, the Coulomb interactions between the EM field and the free electron clouds would give rise to electron density fluctuations, also known as plasma oscillations, within the metal. A plasmon is a quantization of these plasma oscillations, and can be defined as the collective oscillations of free electron density with respect to the fixed positive ions within a metal [4].

Surface plasmons (SPs) are light induced *surface* electron density fluctuations that collectively and coherently oscillate at the interface between any two materials, in which the real portion of the frequency-dependent dielectric permittivity changes sign across the interface [5]. An example of such an interface would be that between a dielectric medium such as air or glass, and a metallic medium, such as silver or aluminum. Surface plasmons result from a hybridized excitation in which the incident light photons couple with the oscillating surface electrons. During this excitation, the free electrons within the metal collectively oscillate at the surface in resonance with the incident light, yielding surface-bound light waves. These surface-bound light waves are always shorter in wavelength than the incident light, and will propagate along the interface until all the energy is eventually attenuated due to absorption in the metal and/or radiation into free-space [5]. On a perfectly flat surface in the visible regime, the SP propagation length is

generally on the order of micrometers (μm). In contrast to the propagating nature of SPs along the surface, the electric ($\vec{E}$) field perpendicular to the surface decays exponentially into the adjacent media. This adjacent $\vec{E}$-field is said to be evanescent or near-field in nature, and is a result of the bound, non-radiative nature of SPs, which prevent power from propagating away from the surface. Typically, the decay length at which the $\vec{E}$-field falls to $1/e$ of its initial value into the dielectric material, δ_d, is on the order of half the wavelength of incident light, whereas the decay length into the metal, δ_m, is between one and two orders of magnitude smaller than the incident light [6]. These compressed dimensions lead to an enhancement of the EM field at the interface [7], and have given rise to the discipline of sub-wavelength optics [5], [6]. Figure 1.1 illustrates the evanescent nature of the SP at the dielectric-metal interface.

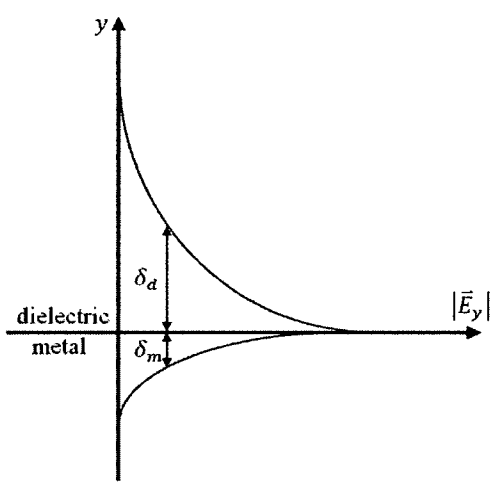

Figure 1.1. Evanescent field of a SP at a dielectic-metal interface.

Optical excitation of SPs can be realized using numerous configurations, each of which remedies the mismatch between the tangential wave vector of the incident light photons and that of the SPs [8], [9]. Historically, one of the most popular excitation techniques employs a prism to achieve total internal reflection, boosting the wave vector

of the incident light photons via contributions from the resultant evanescent wave. This excitation method was first demonstrated, albeit in slightly different configurations, in the late 1960's by both Kretchman [10] and Otto [11]. Another common practice makes use of incident light photon scattering from metallic surface roughness, in order to provide the photons with the necessary wave vector increase. While it is difficult to pinpoint who exactly pioneered this method, significant early contributions were made by both Stern [12] and Fedders [13], among others [14]. This surface roughness can be structured on the nanoscale, giving rise to the term localized surface plasmon resonance [15]. A third technique, which is of most interest, involves using a metallic grating to diffract the incident light, and thus, match the wave vectors. This excitation method, by large the elder of the three [16], will only excite SPs when the incident $\vec{E}$-field has a component along the grating vector. The grating method was first discovered, albeit accidently and inexplicably, as anomalous behavior [16]. It was not until the late 1960's however, that this method could be explained and demonstrated in a controlled manner [17]. Technical advances have also allowed gratings to be structured on the nanoscale, giving rise to renewed interest. Figure 1.2 illustrates the different SP excitation configurations discussed above.

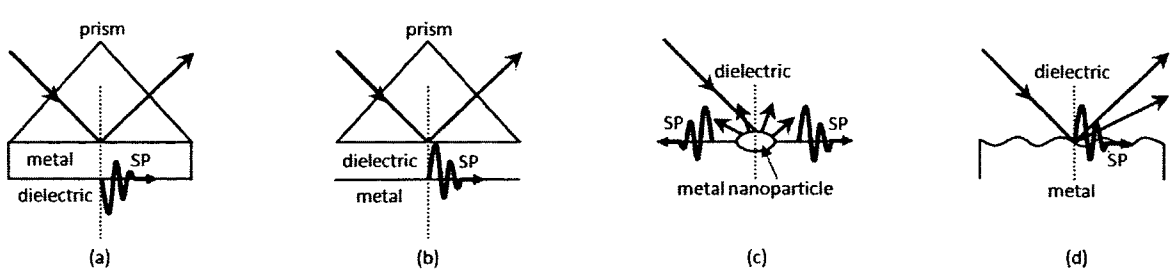

Figure 1.2. SP excitation configurations: (a) Kretchman geometry, (b) Otto geometry, (c) surface roughness (nanoparticle), and (d) diffraction grating.

In the literature, SPs have been referred to by a variety of names [18]. For example, the term surface plasmon polariton [19], [20] is sometimes used to highlight the hybrid, polarizing nature of the excitation. Other terminologies include surface plasmon resonance [18], surface plasma waves [21] and surface plasma oscillations [22]. For the sake of consistency and simplicity, when possible, the term surface plasmons (SPs) shall be used within this thesis.

1.2 Early History

In 1902, while examining polarized light incident on a metallic diffraction grating, R.W. Wood – an optical physicist at John Hopkins University – noticed a mysterious case of uneven distribution of light in the reflected spectrum [16]. He noted that these significant variations in diffraction intensities occurred over very minor angular and spectral ranges, and only when the $\vec{E}$-field vector was perpendicular to the grating ruling. When the $\vec{E}$-field vector was parallel to the grating ruling, the light returned to the traditional, 'accepted' distribution. At the time, conventional grating theory could not explain what was being observed, and Wood was left perplexed. He speculated, among other things, that the introduction of polarization into grating theory may account for such puzzling results; however an obvious explanation could not be given. This anomalous behaviour became known as Wood's Anomalies, and is considered to be the birthplace of the SP. The first theoretical treatment of these anomalies was initiated by Lord Rayleigh in 1907 [23]. His dynamical theory of gratings was based on an expansion of the scattered EM field in terms of outgoing waves only. With this assumption, he found that the scattered field was singular at wavelengths for which one of the spectral orders emerged from the grating at the grazing angle. These singularities appeared again only when the

$\vec{E}$-field vector was perpendicular to the grating ruling, and corresponded to Wood's Anomalies. Wood's later papers further discussed the anomalies [24], [25], however no significant advances were made until the 1940's. In 1941, Italian American physicist Ugo Fano refined Lord Rayleigh's anomalous diffraction grating theory, incorporating such elements as the geometry of the grating and the optical properties of the metal [26]. He found that when the surface tangential component of the diffracted wave vector approached some value, the phenomenon occurred. He went on to describe the phenomenon as being comparable to the resonance of a mechanical oscillating system excited with its proper frequency.

A series of experiments in the 1940's by Ruthemann [27], [28], and later Lang [29], on electron beams shot through thin metallic films found that while most of the beam penetrated the metal without an appreciable energy loss; there were a distinct group of electrons which lost energy. This characteristic energy loss differed from metal to metal, and could not be fully explained. The suggestion of Pines and Bohm [30], [31], [32] that some of the energy losses were due to the excitation of plasma oscillations in the sea of conduction electrons – which they referred to as plasmons – was a great step forward. Although surface EM waves were first discussed nearly five decades earlier by Zenneck [33] and Sommerfeld [34], Ritchie was the first to predict the existence of collective 'surface' oscillations in thin metal films [35], when in 1957 he suggested that their existence may account for some of the low-lying energy losses previously observed in thin metal films. Two years later, a series of electron energy loss experiments by Powell and Swan [36], [37] demonstrated the existence of these collective surface excitations, the quanta of which Stern and Ferrell [38] referred to as the surface plasmon (SP). Further

research revealed that the energy loss resulted from the excitation of SPs in which part of the restoring $\vec{E}$-field extended beyond the specimen boundary [39]. Therefore, SPs could be affected by the presence of any film or contaminant on the specimen surface. This effect was later described in terms of excitation of EM evanescent waves at the surface of the metal [40].

As discussed earlier, in the late 1960's optical excitation of SPs became possible. This proved to be a monumental discovery since until then, all related experimental work had been conducted using an electron beam as a means to excite the SPs. Now it was possible to use common, visible day light to excite SPs. This completely changed their practicality, and made them much more accessible to the scientific community.

1.3 General Applications

Surface plasmons (SPs) are very much a near-field phenomenon, and due to their confining nature, the EM field is enhanced and concentrated at the surface of the metal. This enhancement of the EM field, along with its evanescent nature, result in extraordinary sensitivity of SPs to surface conditions, making them an attractive focus to an assortment of scientists, including physicists, chemists, biologists and material scientists. Their properties have been exploited over a wide range of disciplines, including applications within sensing, spectroscopy, microscopy, communications, data storage, and light generation, among others. In fact, the field has expanded so much that the term plasmonics has been developed to represent the multi-faceted and vast nature of SP applications.

Notorious for being the original and most popular application, SP-based optical sensors detect, measure, and identify the molecular adsorption and binding of chemical and biological quantities, such as polymers, DNA or proteins. First generation sensors were based on changes in SP resonance conditions, and were developed for measuring CO_2 and O_2 concentration [41]. Shortly thereafter, these sensors were used for characterization of thin films [42], monitoring processes at metal interfaces [43], and gas detection and biosensing [44]. Subsequent generation sensors incorporated additional optical methods, such as spectroscopy, ellipsometry and interferometry [45], and later nanotechnology [46]. In the medicinal context, these sensors have been used to study a drug's protein and lipid-binding efficiencies [47], as well as to detect respiratory virus molecular signatures [48], casein allergens in milk [49], and Alzheimer disease biomarkers [50]. Companies such as Biocore® have commercialized SP-based sensors [51], and recent trends have seen much effort placed in versatile, multi-channel sensors, aimed at enhancing sensor throughput, providing multi-analyte detection capability [52], [53].

Surface plasmons (SPs) can also be used to enhance the surface sensitivity of several spectroscopic measurements, including fluorescence [54] and Raman scattering [55], with the enhancement factor of the latter having been shown to be as much as 10^{11} [56], allowing for the detection of single molecules [57]. Another use has been to improve upon the classical limits of resolution within optical microscopy [58]. By using the evanescent SPs to illuminate the sample and provide image contrast, enhanced super-resolution of ~ 0.33 nanometers (nm) has been demonstrated [59].

In the digital age, optical communication systems have become quite common. The need for these systems to be integrated onto nanoscale electronic chips has led to SP-

based devices which have both the capacity of traditional photonics, yet the miniaturization of electronics [60]. Examples of such electro-optical devices include SP waveguides [61], switches [62], couplers [63], and modulators [64]. Surface plasmons (SPs) have also been explored for their potential to improve upon conventional optical data storage methods, such as dvd and blu-ray. Recently, a SP-based data storage medium was proposed on which optical data could be recorded with less than one-quarter of the exposure power of blu-ray disc, and with 1.8 times the data storage capacity [65].

Another application of SPs involves their use in improving upon the low light-emission efficiencies of light emitting diodes (LEDs). Scientists have found that by coating very thin (nm) silver or aluminum films over the quantum wells, a new class of super-bright LEDs comparable to fluorescent tubes were made possible [60]. In addition to what we have already discussed, many other SP-based applications currently exist, with others continuously being developed and explored. Such exploratory applications include a cancer treatment employing plasmonic effects to heat and destroy tumor cells, as well as a cloaking device employing SP resonances and metamaterials [66].

1.4 Photovoltaic Applications

As seen, SPs are extremely versatile with their applications being found throughout the sciences in numerous fields. While the applications discussed thus far have been very impressive, arguably their greatest potential lies within the field of photovoltaics (PVs). Photovoltaic (PVs), also known as solar electricity, is the direct conversion of solar radiation into electricity through the use of a solar cell (SC) [67]. In its simplest form, a SC is a layer of photoactive material sandwiched between two metal

electrodes, all resting upon a substrate. The photoactive material converts absorbed light into photocurrent, which in turn is harvested by the electrodes. Figure 1.3 depicts the architecture of a basic SC. Note that the top electrode is meant to be very thin such that light can freely pass through.

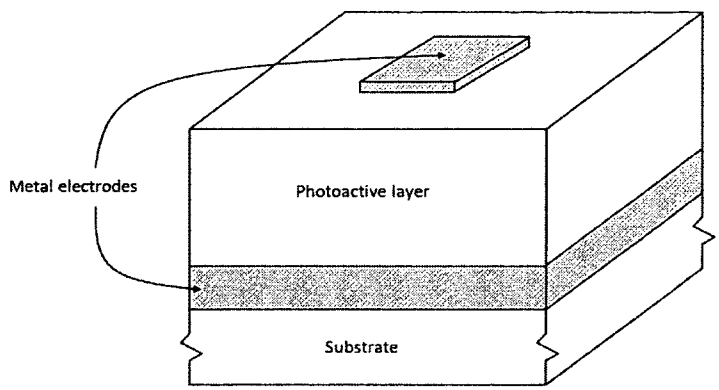

Figure 1.3. Architecture of a basic SC.

The first practical use of SCs was in the generation of electricity onboard the orbiting satellite Vanguard 1 in 1958 [67]. These first generation SCs used bulk crystalline silicon to convert photons into electrical energy. This bulk crystalline silicon however, proved very expensive and in order to decrease the costs, thin-film SCs were developed. In addition to silicon, second generation thin-film SCs were developed that employed other photoactive materials, including those based on organic dyes and polymers. These organic materials have proven less expensive than their alternatives, and have given rise to a specific class of SC called organic solar cells (OSCs) [68].

While second generation SCs were based on cost effectiveness, third generation SCs have been focused on enhancing the photocurrent generation of existing SCs. One method to achieve this enhancement is to exploit SPs at the polymer/electrode interface.

In doing so, enhanced photocurrent is generated around the wavelength satisfying the SP resonance conditions. Surface plasmon (SP)-based OSCs have been shown to enhance photocurrent generation for a number of different architectures [69], involving a variety of polymer materials [70], [71], [72]. The bulk hetero-junction blend of the polymer poly (3-hexylthiophene) (P3HT) and the fullerene [6,6]-phenyl C_{61}-butyric (PCBM) has shown much potential as an OSC material [73], [74]. Surface plasmon (SP)-based OSCs have been fabricated using both nanoparticles [75] and nanogratings [76] as the excitation methods, with modest success. Photocurrent enhancements of 2.72 times have been demonstrated for incident light upon an OSC using a single-grating system [77]. Similarly, photocurrent enhancements have also been demonstrated for both TM and TE polarized light incident upon OSCs structured on a cross-grating system [78], [79]. No work however, could be found on SP-based OSCs structured on a parallel-grating system – that is two parallel gratings of different spacing superimposed on each other.

1.5 Goal of Research

Coal, oil, or natural gas – fossil fuels have persistently dominated the Earth's energy consumption. Much attention is being placed on the rate at which these non-sustainable energy reserves are being depleted, not to mention the harmful environmental effects associated with their production and usage. Under the assumption that the Earth's population does not change drastically, and its energy consumption remains at the current level, fossil fuel reserves will be exhausted within 320 years [67]. With the World's population expected to reach 10 billion in the next century, alternate energy sources – which are both sustainable and environmentally friendly – are critical to the survival of mankind.

Photovoltaics (PVs) represent one such energy source. With 1000 $W \cdot m^{-2}$ of terrestrial solar energy available (AM 1.5 standard) [67], great potential lies within harnessing this radiation and converting it directly into electricity via SCs. While impressive strides have already been made, currently the efficiencies of SCs in converting solar radiation into electricity is about 28% for inorganic and 10% for OSCs [80]. This conversion efficiency must increase considerably if further progress is to be made. Surface plasmon (SP)-based SCs display much promise in improving upon this conversion efficiency. Integrated into existing SC technologies, SP-based systems have demonstrated a keen ability to increase optical absorption, thus enhancing photocurrent generation within the photoactive material.

Due to their relatively low-cost synthesis and ease of fabrication, SP-based, P3HT:PCBM OSCs excited via the grating method will be explored in this thesis. Organic solar cells (OSCs) structured on single, crossed and parallel grating systems, will be fabricated and examined, with photocurrent enhancements being shown for each. When compared to the enhanced photocurrent response of a single-grating system, that of a parallel-grating will be shown to be over a broader range of wavelengths. No current technical literature could be found on SP-based, P3HT:PCBM OSCs structured on a parallel-gating system. Hopefully, this research will offer a novel contribution to the field of SP-based OSCs, and potentially provide some assistance in the resolution of the World's impending energy crisis. It should be noted that while the application of SPs within P3HT:PCBM OSCs are of eventual interest, the majority of thesis-related research is focused within chapter 3 on the optimization of SPs.

1.6 Thesis Structure

This thesis is divided into 5 chapters. Chapter 1 is an introduction into the field of SPs. Following some necessary definitions, the properties and optical excitation methods of SPs are introduced. An overview of the early history of SPs is then provided, followed by a discussion of some of the applications found throughout the world today, focusing on those related to PVs, specifically OSCs. It concludes with a brief discussion detailing the goal of research, and the expected contribution to the field of SP-based OSCs.

Chapter 2 mainly discusses the theory associated with SPs. Relevant properties of light are initially discussed before proceeding to examine its behavior at a boundary. Following an introduction to diffraction gratings, the SP dispersion relation is derived using the appropriate Maxwell's equation and boundary conditions. Finally, SP excitation is discussed, and the matching condition required for incident light to excite SPs via the grating method is given.

Chapter 3 discusses the fabrication methods and experimental procedures used in building and measuring SP test samples, as well as the accompanying results. First, SPs generated from an air-silver (Ag) interface using single, crossed, and parallel gratings of various spacings and depths are examined. Then, SPs generated from a thin film polyvinyl alcohol (PVA)-Ag interface, using the same grating configurations, but slightly different spacings are examined. From these results, optimal grating depths and film thicknesses with which to fabricate the OSCs are determined.

Chapter 4 discusses the fabrication methods and experimental procedures used in building and measuring SP-based, P3HT:PCBM OSC samples, as well as the

accompanying results. The photocurrent response of OSCs fabricated using single, crossed, and parallel grating systems are examined. Enhanced photocurrent responses owing to SPs are shown for all grating schemes.

Chapter 5 offers concluding remarks and observations on the experimental procedures used and the subsequent results.

REFERENCES

[1] R. Kooyman, "Chapter 2 - Physics of Surface Plasmon Resonance," in *Handbook of Surface Plasmon Resonance*, Cambridge, The Royal Society of Chemistry, 2008, pp. 15-34.

[2] H. Reather, "Chapter 1 - Introduction," in *Surface Plasmons on Smooth and Rough Surfaces and on Gratings*, London, Springer-Verlag, 1988, pp. 1-3.

[3] J. Bittencourt, "Chapter 1 - Introduction," in *The Fundamentals of Plasma Physics*, New York, Springer-Verlag, 2004, pp. 1-32.

[4] D. Sarid and W. Challener, "Chapter 1 - Introduction," in *Modern Introduction to Surface Plasmons*, Cambridge, Cambridge University Press, 2010, pp. 1-4.

[5] W. Barnes, "Surface Plasmon Subwavelength Optics," *Nature,* vol. 424, no. 6950, pp. 824-830, 2003.

[6] W. Barnes, "Surface Plasmon-Polariton Length Scales: A Route to Sub-Wavelength Optics," *Journal of Optics A: Pure and Applied Optics,* vol. 8, pp. S87-S93, 2006.

[7] F. Yu, "Surface Plasmon Fluorescence Spectroscopy and Surface Plasmon Diffraction in Bimolecular Interaction Studies," Max Planck Institute for Polymer Research , Mainz, 2004.

[8] D. Beaglehole, "Optical Excitation of Surface Plasmons," *IEEE Transcations on Electron Devices,* vol. 17, no. 3, pp. 240-244, 1970.

[9] J. Scambles, G. Bradbery and F. Yang, "Optical Excitation of Surface Plasmons: An Introduction," *Contemporary Physics,* vol. 32, no. 3, pp. 173-183, 1991.

[10] E. Kretschmann and H. Raether, "Radiative Decay of Non-Radiative Surface Plasmon Excited by Light," *Zeitschrift für Naturforschung,* vol. 23A, pp. 2135-2136, 1968.

[11] A. Otto, "Excitation of Non-Radiative Surface Plasma Waves in Silver by the Method of Frusterated Total Reflection," *Zeitschrift ffir Physik,* vol. 216, pp. 398-410, 1968.

[12] E. Stern, "Plasma Radiation by Rough Surfaces," *Physical Review Letters,* vol. 19, no. 23, pp. 1321-1324, 1967.

[13] P. Fedders, "Indirect Coupling of Photons to the Surface Plasmon," *Physics Review,* vol. 165, no. 2, pp. 580-587, 1968.

[14] J. Elson and R. Ritchie, "Photon Interactions at a Rough Metal Surface," *Physical Review B,* vol. 4, no. 12, p. 4129–4138, 1971.

[15] A. Zayats, I. Smolyaninov and A. Maradudin, "Nano-Optics of Surface Plasmon Polaritons," *Physics Reports,* vol. 408, no. 3-4, pp. 131-314, 2005.

[16] R. Wood, "On a Remarkable Case of Uneven Distribution of Light in a Diffraction Grating Spectrum," *Proceedings of the Physical Society of London* , vol. 18, pp. 269-275, 1902.

[17] Y. Teng, "Plasma Radiation from Metal Grating Surfaces," *Physical Review Letters,* vol. 19, no. 9, pp. 511-514, 1967.

[18] A. Tudos and R. Schasfoort, "Chapter 1 - Introduction to Surface Plasmon Resonance," in *Handbook of Surface Plasmon Resonance*, Cambridge, The Royal Society of Chemistry, 2008, pp. 1-14.

[19] K. Welford, "Surface Plasmon-Polaritons and their Uses," *Optical and Quantum Electronics,* vol. 23, no. 1, pp. 1-27, 1991.

[20] J. Pitarke, V. Silkin, E. Chulkov and P. Echenique, "Theory of Surface Plasmons and Surface-Plasmon Polaritons," *Reports on Progress in Physics,* vol. 70, pp. 1-87, 2007.

[21] S. Zaidi, M. Yousaf and S. Brueck, "Grating Coupling to Surface Plasma Waves. I. First-Order Coupling," *Optical Society of America,* vol. 8, no. 4, pp. 770-779, 1991.

[22] H. Raether, "Surface Plasma Oscillations and their Applications," in *Physics of Thin Films, Vol. 9*, New York, Academic Press, 1977, pp. 145-261.

[23] L. Rayleigh, "On the Dynamical Theory of Gratings," *Proceedings of the Royal Society of London Series A,* vol. 79, no. 532, pp. 399-416, 1907.

[24] R. Wood, "Diffraction Gratings with Controlled Groove Form and Abnormal Distribution of Intensity," *Philosophical Magazine Series 6,* vol. 23, no. 134, pp. 310-317, 1912.

[25] R. Wood, "Anomalous Diffraction Gratings," *Physical Review,* vol. 48, no. 12, pp. 928-936, 1935.

[26] U. Fano, "The Theory of Anomalous Diffraction Gratings and of Quasi-Stationary Waves on Metallic Surfaces (Sommerfeld's Waves)," *J. Opt. Soc. Am. 31,* vol. 31, no. 3, pp. 213-222, 1941.

[27] G. Ruthemann, "Diskrete Energieverluste schneller Elektronen in Festkörpern," *Naturwissenschaften,* vol. 29, no. 42-43, p. 648, 1941.

[28] G. Ruthemann, "Elektronenbremsung an Röntgenniveaus," *Naturwissenschaften,* vol. 30, no. 9, p. 145, 1942.

[29] W. Lang, "Geschwindigkeitsuerluste mittleschneller elektronen keine durchgang durch dinne

metallfolien," *Optik,* vol. 3, p. 233, 1948.

[30] D. Pines and D. Bohm, "A Collective Description of Electron Interactions: I. Magnetic Interactions," *Physical Review,* vol. 82, no. 5, pp. 625-634, 1951.

[31] D. Bohm and D. Pines, "A Collective Description of Electron Interactions: II. Collective vs Individual Particle Aspects of the Interactions," *Physical Review,* vol. 85, no. 2, pp. 338-353, 1952.

[32] D. Bohm and D. Pines, "A Collective Descrition of Electron Interaction: III. Couloumb Interactions in a Degenerate Electron Gas," *Physical Review,* vol. 92, no. 3, pp. 609-625, 1953.

[33] J. Zenneck, "Über die Fortpflanzung ebener elektromagnetischer Wellen längs einer ebenen Leiterfläche und ihre Beziehung zur drahtlosen Telegraphie," *Allanen der Physik,* vol. 23, pp. 846-866, 1907.

[34] A. Sommerfeld, "Über die Ausbreitlung der Wellen in der drahtlosen Telegraphie," *Annalen der Physik,* vol. 28, pp. 665-736, 1909.

[35] R. Ritchie, "Plasma Losses by Fast Electron in Thin Films," *Physical Review,* vol. 106, no. 5, pp. 874-881, 1957.

[36] C. Powell and J. Swan, "Origin of the Characteristic Electron Energy Losses in Aluminum," *Physical Review,* vol. 115, no. 4, p. 869–875, 1959.

[37] C. Powell and J. Swan, "Origin of the Characteristic Electron Energy Losses in Magnesium," *Physical Review,* vol. 116, no. 1, pp. 81-83, 1959.

[38] E. Stern and R. Ferrell, "Surface Plasma Oscillations of a Degenerate Electron Gas," *Physical Review,* vol. 120, no. 1, pp. 130-136, 1960.

[39] C. Powell and J. Swan, "Effect of Oxidation on the Characteristic Loss Spectra of Aluminum and Magnesium," *Physical Review,* vol. 118, no. 3, pp. 640-643, 1960.

[40] E. Burstein, W. Chen, Y. Chen and A. Hartstein., "Surface Polaritons—Propagating Electromagnetic Modes at Interfaces," *Journal of Vacuum Science and Technology,* vol. 11, no. 6, pp. 1004-1019, 1974.

[41] D. Lubbers and N. Opitz, "Eine neue pCO2-bzw: pO2-Messonde zur Messung des pCO2 oder pO2 von Gasen und Flüssigkeiten," *Zeitschrift Für Naturforschung C,* vol. 30, pp. 532-533, 1975.

[42] I. Pockrand, J. Swalen, J. Gordon and M. Philpott, "Surface Plasmon Spectroscopy of Organic Monolayer Assemblies," *Surface Science,* vol. 74, no. 1, pp. 237-244, 1978.

[43] J. Gordon and S. Ernst, "Surface Plasmons as a Probe of the Electrochemical Interface," *Surface Science,* vol. 101, no. 1-3, pp. 499-506, 1980.

[44] B. Liedberg, C. Nylander and I. Lunström, "Surface Plasmon Resonance for Gas Detection and Biosensing," *Sensors and Actuators,* vol. 4, pp. 299-304, 1983.

[45] J. Homola, S. Yee and G.Gauglitz, "Surface Plasmon Resonance Sensors: Review," *Sensors and Actuators B: Chemical,* vol. 54, no. 1-2, pp. 3-15, 1999.

[46] A. Haes and R. VanDuyne, "A Nanoscale Optical Biosensor: Sensitivity and Selectivity of an Approach Based on the Localized Surface Plasmon Resonance Spectroscopy of Triangular Silver Nanoparticles," *Journal of the American Chemical Society,* vol. 124, no. 35, pp. 10596-10604, 2002.

[47] M. Cooper, "Optical Biosensors in Drug Discovery," *Nature Reviews: Drug Discovery* , vol. 1, pp. 515-528, 2002.

[48] S. Shanmukh, L. Jones, J. Driskell, Y. Zhao, R. Dluhy and R. Tripp, "Rapid and Sensitive Detection of Respiratory Virus Molecular Signatures Using a Silver Nanorod Array SERS Substrate," *Nano Letters,* vol. 6, no. 11, p. 2630–2636, 2006.

[49] H. Hiep, T. Endo, K. Kerman, M. Chikae, D. Kim, S. Yamamura, Y. Takamura and E. Tamiya, "A Localized Surface Plasmon Resonance Based Immunosensor for the Detection of Casein in Milk," *Science and technology of Advanced Materials,* vol. 8, no. 4, pp. 331-338, 2007.

[50] K. Hegnerová, M. Bocková, H. Vaisocherová, Z. Krištofiková, J. Říčný, D. Řípová and J. Homola, "Surface Plasmon Resonance Biosensors for Detection of Alzheimer Disease Biomarker," *Sensors and Actuators B: Chemical,* vol. 139, no. 1, pp. 69-73, 2009.

[51] "Biocore Life Sciences," Biocore, [Online]. Available: http://www.biacore.com/lifesciences/index.html. [Accessed 26 January 2012].

[52] B. Sutapun, A. Somboonkaew, R. Amrit, N. Houngkamhang and T. Srikhirin, "A Multichannel Surface Plasmon Resonance Sensor using a New Spectral Readout System without Moving Optics," *Sensors and Actuators B: Chemical,* vol. 156, no. 1, pp. 312-318, 2011.

[53] S. Grego, K. Gilchrist, J. Carlson and B. Stoner, "A Compact and Multichannel Optical Biosensor based on a Wavelength Interrogated Input Grating Coupler," *Sensors and Actuators B: Chemical,* vol. 161, no. 1, pp. 721-727, 2012.

[54] T. Liebermann and W. Knoll, "Surface-Plasmon Field-Enhanced Fluorescence Spectroscopy," *Colloids and Surfaces A: Physicochemical and Engineering Aspects,* vol.

171, no. 1-3, pp. 115-130, 2000.

[55] A. Campion and P. Kambhampati, "Surface-Enhanced Raman Scattering," *Chemical Society Reviews,* vol. 27, no. 4, pp. 241-250, 1998.

[56] E. Blackie, E. LeRu and P. Etchegoin, "Single-Molecule Surface-Enhanced Raman Spectroscopy of Nonresonant Molecules," *Journal of the American Chemical Society,* vol. 131, no. 40, p. 14466–14472, 2009.

[57] E. LeRu, M. Meyer and P. Etchegoin, "Proof of Single-Molecule Sensitivity in Surface Enhanced Raman Scattering (SERS) by Means of a Two-Analyte Technique," *The Journal of Physical Chemistry B,* vol. 110, no. 4, pp. 1944-1948, 2006.

[58] S. Kawata, "Near-Field Microscope Probes Utilizing Surface Plasmon Polaritons," *Topics in Applied Physics,* vol. 81, pp. 15-27, 2001.

[59] K. Watanabe, M. Ryosuke, G. Terakado, T. Okazaki, K. Morigaki and H. Kano, "High Resolution Imaging of Patterned Model Biological Membranes by Localized Surface Plasmon Microscopy," *Applied Optics,* vol. 49, no. 5, pp. 887-891, 2010.

[60] E. Ozbay, "Plasmonics: Merging Photonics and Electronics at Nanoscale Dimensions," *Science,* vol. 311, no. 5758, pp. 189-193, 2006.

[61] S. Maier and H. Atwater, "Plasmonics: Localization and Guiding of Electromagnetic Energy in Metal/Dielectric Structures," *Journal of Applied Physics,* vol. 98, no. 1, p. 011101, 2005.

[62] Y. Zheng, Y. Yang, L. Jensen, L. Fang, B. Juluri, A. Flood, P. Weiss, J. F. Stoddart and T. Huang, "Active Molecular Plasmonics: Controlling Plasmon Resonances with Molecular Switches," *Nano Letters,* vol. 9, no. 2, pp. 819-825, 2009.

[63] J. Krenn and J. Weeber, "Surface Plasmon Polaritons in Metal Stripes and Wires," *Philosophical Transactions: The Royal Society of London Series A,* vol. 362, no. 1817, pp. 739-756, 2004.

[64] J. Dionne, K. Diest, L. Sweatlock and H. Atwater, "PlasMOStor: A Metal–Oxide–Si Field Effect Plasmonic Modulator," *Nano Letters,* vol. 9, no. 2, pp. 897-902, 2009.

[65] S. Park and J. Hahn, "Plasmonic Data Storage Medium with Metallic Nano-Aperture Array Embedded in Dielectric Material," *Optics Express,* vol. 17, no. 22, pp. 20203-20210, 2009.

[66] H. Atwater, "The Promise of Plasmonics," *Scientific American,* vol. 296, no. 4, pp. 56-63, 2007.

[67] M. Zeman, "Delft University of Technology Solar Cell Course Reading - Chapter 1: Introduction to Photovoltiac Solar Energy," [Online]. Available:

http://ocw.tudelft.nl/courses/microelectronics/solar-cells/readings/1-introduction-to-photovoltaic-solar-energy/. [Accessed 20 May 2011].

[68] S. Günes, H. Neugebauer and N. Sariciftci, "Conjugated Polymer-Based Organic Solar Cells," *Chemical Reviews,* vol. 107, no. 4, pp. 1324-1338, 2007.

[69] M. Niggemann, M. Glatthaar, A. Gombert, A. Hinsch and V. Wittwer, "Diffraction Gratings and Buried Nano-Electrodes—Architectures for Organic Solar Cells," *Thin Solid Films,* Vols. 451-452, pp. 619-623, 2004.

[70] N. Lindquist, W. Luhman, R. Holmes and S. Oh, "Plasmonic Nanocavity Arrays for Enhanced Efficiency in Organic Photovoltaic Cells," *Applied Physics Letters,* vol. 93, no. 12, pp. 123308-123308, 2008.

[71] D. Duche, P. Torchio, L. Escoubas, F. Monestier, J. Simon, F. Flory and G. Mathian, "Improving Light Absorption in Organic Solar Cells by Plasmonic Contribution," *Solar Energy Materials and Solar Cells,* vol. 93, no. 8, pp. 1377-1382, 2009.

[72] K. Le, A. Abass, B. Maes, P. Bienstman and A. Alù, "Comparing Plasmonic and Dielectric Gratings for Absorption Enhancement in thin-film Organic Solar Cells," *Optics Express,* vol. 20, no. S1, pp. A39-A50, 2012.

[73] G. Li, V. Shrotriya, J. Huang, Y. Yao, T. Moriarty, K. Emery and Y. Yang, "High-Efficiency Solution Processable Polymer Photovoltaic Cells by Self-Organization of Polymer Blends," *Nature Materials,* vol. 4, no. 11, pp. 864 - 868, 2005.

[74] K. Kim, J. Liu, M. Namboothiry and D. Carroll, "Roles of Donor and Acceptor Nanodomains in 6% Efficient Thermally Annealed Polymer Photovoltiacs," *Applied Physics Letters,* vol. 90, no. 16, p. 163511, 2007.

[75] S. Kim, S. Na, J. Jo, D. Kim and Y. Nah, "Plasmon Enhanced Performance of Organic Solar Cells using Electrodeposited Ag Nanoparticles," *Applied Physics Letters,* vol. 93, no. 7, p. 073307, 2008.

[76] K. Tvingstedt, N. Persson and O. Inganäs, "Surface Plasmon Increase Absorption in Polymer Photovoltaic Cells," *Applied Physics Letters,* vol. 91, no. 11, p. 113514, 2007.

[77] R. Sabat, M. Santos and P. Rochon, "Surface Plasmon-Induced Band Gap in the Photocurrent Response of Organic Solar Cells," *International Journal of Photoenergy,* vol. 2010, p. 698718, 2010.

[78] S. Na, S. Kim, J. Jo, S. Oh, J. Kim and D. Kim, "Efficient Polymer Solar Cells with Surface Relief Gratings Fabricated by Simple Soft Lithography," *Advanced functional Materials,* vol. 18, no. 24, p. 3956–3963, 2008.

[79] M. Sefunc, A. Okyay and H. Demir, "Plasmonic Backcontact Grating for P3HT:PCBM Organic Solar Cells Enabling Stong Optical Absorption Increased in all Polarization," *Optics Express,* vol. 19, no. 15, pp. 14200-14209, 2011.

[80] M. Green, K. Emery, Y. Hishikawa, W. Warta and E. Dunlop, "Solar Cell Efficiency Tables (version 39)," *Progress in Photovoltaics: Research and Applications,* vol. 20, no. 1, pp. 12-20, 2012.

CHAPTER 2: THEORY

Chapter two is designed to provide the reader with a collection of the theory encountered during the experimental portion of this thesis. It is intended to start at a fundamental level, and progressively mature to more complex concepts. Any notations and assumptions will be highlighted and explained, and when deemed necessary, full derivations of equations will be provided. For the sake of practicality and ease, and given the nature of this research, most derivations will be approximations, purposely excluding most irregularities and losses. In the instances where full derivations of equations are not given, a brief statement highlighting the origin and nature of the derivation will be provided. Theory specific to an experimental technique or device will be presented in later chapters in conjunction with its purpose.

2.1 Electro-Magnetic (EM) Fundamentals

2.1.1 Light as an Electro-Magnetic (EM) Plane Wave

For the purpose of this thesis, light will be evaluated as a monochromatic, harmonic, coherent EM plane wave. Monochromatic meaning the wave has only a single-frequency component, harmonic meaning the wave is purely sinusoidal, and coherent meaning that the phase between the constituent waves can be reliably predicted. A plane wave refers to a wave whose wave front has no curvature, but instead is considered completely planar, with its origin assumed to be an infinite distance away. It consists of an infinite number of these parallel planes of constant peak-to-peak amplitude normal to the direction of wave travel. All points on a plane are of constant phase. Figure

2.1 provides an illustration of such an EM plane wave propagating through free-space in the x-direction.

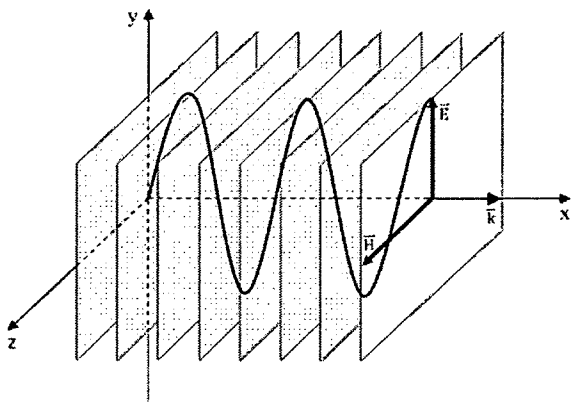

Figure 2.1. EM plane wave propagating in the x-direction.

The EM plane wave is assumed to have both electric and magnetic field components, known as $\vec{E}$- and $\vec{H}$-fields respectively, orthogonal to each other, and to the direction of wave propagation. This is known as a transverse plane wave. Figure 2.2 illustrates the $\vec{E}$- and $\vec{H}$-fields of a transverse EM plane wave propagating through free-space in the x-direction, with its oscillations occurring in the y-z plane.

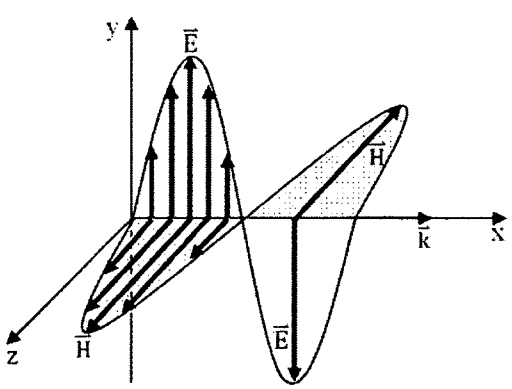

Figure 2.2. Transverse EM plane wave propagating in the x-direction.

2.1.2 Maxwell's Equations and Dielectric Permittivity

The relationship between the $\vec{E}$- and $\vec{H}$-fields of an EM wave are given by Maxwell's equations, with one being easily derived from the other. These fundamental equations govern the propagation of EM fields in the presence of charges, current and media. Maxwell's equations for a charge-free medium written in their time-harmonic form are given by equations 2.1a – 2.1d [1], [2]:

$$\nabla \cdot \varepsilon \vec{E} = 0 \tag{2.1a}$$

$$\nabla \cdot \mu \vec{H} = 0 \tag{2.1b}$$

$$\nabla \times \vec{E} = i\omega\mu\vec{H} \tag{2.1c}$$

$$\nabla \times \vec{H} = \sigma\vec{E} - i\omega\varepsilon\vec{E} = -i\omega\left[\varepsilon + i\frac{\sigma}{\omega}\right]\vec{E} = -i\omega\tilde{\varepsilon}\vec{E} \tag{2.1d}$$

where σ is a measure of the material's ability to conduct electric current, known as its conductivity, while ε and μ are parameters describing the material's ability to store electrical and magnetic energy, known as its dielectric permittivity and magnetic permeability respectively. Both ε and μ are frequency and medium dependent, but are assumed to be independent of the fields, position and direction (i.e. media assumed to be linear, homogeneous and isotropic, respectively). Intuitively, they represent how a specific medium influences the $\vec{E}$- and $\vec{H}$-fields of an EM wave, and are given by equations 2.2a and 2.2b [1]:

$$\varepsilon = \varepsilon_o\varepsilon_r \tag{2.2a}$$

$$\mu = \mu_o\mu_r \tag{2.2b}$$

where ε_r is the relative dielectric permittivity, ε_o is the permittivity of free-space, also known as the dielectric constant, μ_r is the relative magnetic permeability, and μ_o is the

permeability of free-space. From equation 2.2.a one can easily see that the relative dielectric permittivity represents the ratio of the dielectric permittivity relative to that of free-space ($\varepsilon_r = \varepsilon/\varepsilon_o$). While the same can be said about the relative magnetic permeability, the point becomes moot since all media within this thesis are assumed non-magnetic (i.e. $\mu_r = 1$). If the medium is anisotropic, the dielectric permittivity will be a tensor. The ˜ designator is simply used to represent the effective dielectric permittivity and is given by equation 2.3:

$$\tilde{\varepsilon} = \left[\varepsilon + i\frac{\sigma}{\omega}\right] = \tilde{\varepsilon}' + i\tilde{\varepsilon}'' \tag{2.3}$$

where $\tilde{\varepsilon}'$ denotes the real portion of the effective dielectric permittivity, which is related to the energy stored within the medium, and $\tilde{\varepsilon}''$ denotes the imaginary portion of the effective dielectric permittivity, which is related to the loss of energy within the medium.

2.1.3 Classification of Media

Media can often be classified according to their dielectric permittivity and conductivity. Those with a large amount of loss inhibit the propagation of EM waves, and are considered good conductors. Alternatively, lossless or low loss materials which allow the propagation of EM waves are considered good dielectrics. Delineation between a good conductor and a lossy dielectric is not easily made. As such, one often relies on a ratio known as the loss tangent in order to properly classify and evaluate a material. The loss tangent of a medium is given by equation 2.4 [1]:

$$tan(\theta) = \frac{\tilde{\varepsilon}''}{\tilde{\varepsilon}'} = \frac{\sigma}{\omega\varepsilon} \tag{2.4}$$

where θ is the loss angle of the medium as illustrated by figure 2.3.

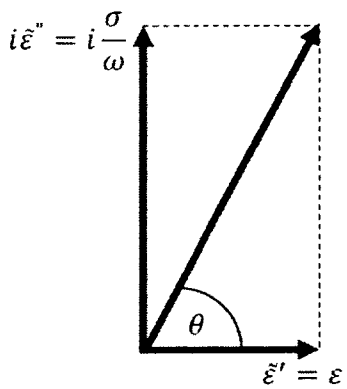

Figure 2.3. Loss angle of a lossy medium.

A medium is said to be a good conductor if the loss tangent is very large ($\sigma/\omega\varepsilon \gg 1$), and conversely a good dielectric (lossless or low loss) if the loss tangent is very small ($\sigma/\omega\varepsilon \ll 1$). In the latter case, the conductivity of the material is negligible, and thus the imaginary portion of the effective dielectric permittivity is ignored (i.e. $\tilde{\varepsilon} = \tilde{\varepsilon}' = \varepsilon$).

2.1.4 Polarization of Light

The polarization of light is a characteristic which describes the orientation of its $\vec{E}$-field vector in a plane perpendicular to the direction of propagation. If one were to trace the tip of the $\vec{E}$-field vector in a fixed plane as the wave propagates, the shape traced out in the plane would indicate the polarization of the light. If the $\vec{E}$-field vector is oriented in a single direction, a straight line will be traced – this is known as linear polarization. Figure 2.4 illustrates linearly polarized light as the vector sum of two orthogonal, in phase, constituent waves.

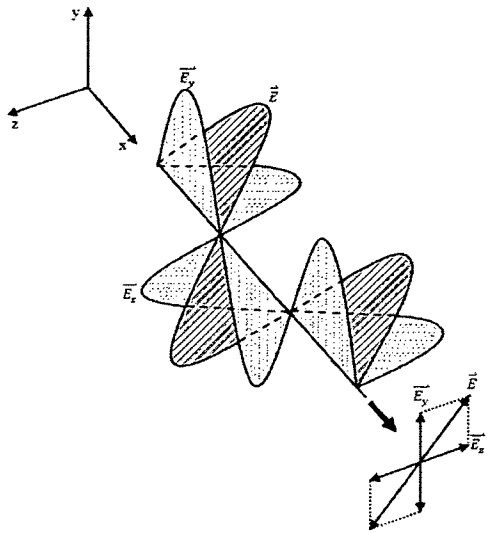

Figure 2.4. Linearly polarized light.

If the $\vec{E}$-field vector rotates as the wave travels, tracing the tip will produce a circle or ellipse – this is known as circular or elliptical polarization. When the constituent waves contributing to the $\vec{E}$-field vector are equal in amplitude, but out of phase by $\pi/2$, the resulting net $\vec{E}$-field vector will rotate in a circular pattern, yielding circularly polarized light. The $\vec{E}$-field vector will make one complete rotation as the wave advances one wavelength. Circularly polarized light can be obtained by passing linearly polarized light through a $\lambda/4$ plate. A $\lambda/4$ plate is a retarding device consisting of a birefringent, double refracting material, with both an extraordinary (fast) and ordinary axis. In order for the linear-to-circular polarization conversion to occur, the $\vec{E}$-field vector of the linearly polarized light must be incident at an angle of 45° to the fast axis. Intuitively, light passing through the fast axis will travel more quickly than that passing through the ordinary axis. In the case of a $\lambda/4$ plate, the constituent light waves will emerge a $\lambda/4$ (i.e. $\pi/2$) out of phase, thus producing circularly polarized light. The reverse is also true,

with circularly polarized incident light yielding linearly polarized light. Depending on which polarization component is retarded, the circularly polarized light can further be classified as either right or left polarized. If one were to view the wave as propagating *towards* oneself, clockwise (CW) $\vec{E}$-field vector rotation would be known as right polarized, whereas counterclockwise (CCW) rotation would be known as left polarized. Figure 2.5 illustrates right-circularly polarized light as the vector sum of two orthogonal, constituent waves of equal amplitudes, but out of phase by $\pi/2$.

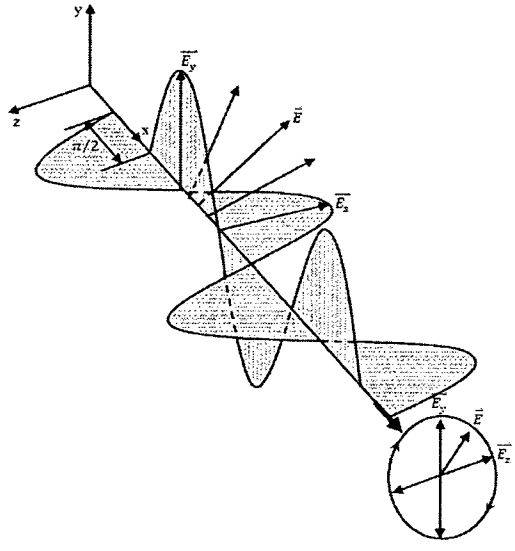

Figure 2.5. Right-circularly polarized light.

2.1.5 Mathematical Description of Light

Solutions to the wave equation for a linearly polarized, harmonic EM plane wave propagating in an arbitrary direction in a charge-free, lossless or low loss dielectric medium will take the form given by equation 2.5 [1], [3]:

$$\vec{E}(\vec{r},t) = Re\{\vec{E}(\vec{r})e^{-i\omega t}\} \tag{2.5}$$

where $\vec{E}(\vec{r})$ is the phasor of $\vec{E}(\vec{r},t)$, $e^{-i\omega t}$ is the time dependence factor, $\vec{r}$ is the position vector ($\vec{r} = x\vec{a}_x + y\vec{a}_y + z\vec{a}_z$), and ω is the angular frequency ($\omega = 2\pi f$). For ease of derivation, the time dependence factor in equation 2.5 can be ignored, since it will remain constant throughout. This yields the phasor form of the EM plane wave as given by equation 2.6 [1], [3]:

$$\vec{E}(\vec{r}) = \vec{E} = \vec{E}_o e^{i(\vec{k}\cdot\vec{r}-\varphi)} \tag{2.6}$$

where $\vec{E}_o$ is the $\vec{E}$-field directional amplitude, $\vec{k}$ is the wave vector ($\vec{k} = k_x\vec{a}_x + k_y\vec{a}_y + k_z\vec{a}_z$) along the direction of propagation, and φ is some initial phase shift (which can be zero). The magnitude of the wave vector is known as the wave number, $|\vec{k}| = k = 2\pi/\lambda$, where λ is the wavelength of light in the medium.

2.2 Light at a Boundary

2.2.1 Laws of Reflection and Refraction

When light is incident upon a boundary between two different media, a portion of it is reflected back into the first medium, and a portion of it is transmitted, or refracted, into the second medium. This is illustrated in the geometrical sense in terms of light rays by figure 2.6(a). A ray is a line drawn in space corresponding to the direction of flow of radiant energy [4]. The incident, reflected and refracted rays all lie within the plane of incidence – defined by the incident wave vector, $\vec{k}_i$, and the normal to the surface – and are all perpendicular to their respective wave fronts.

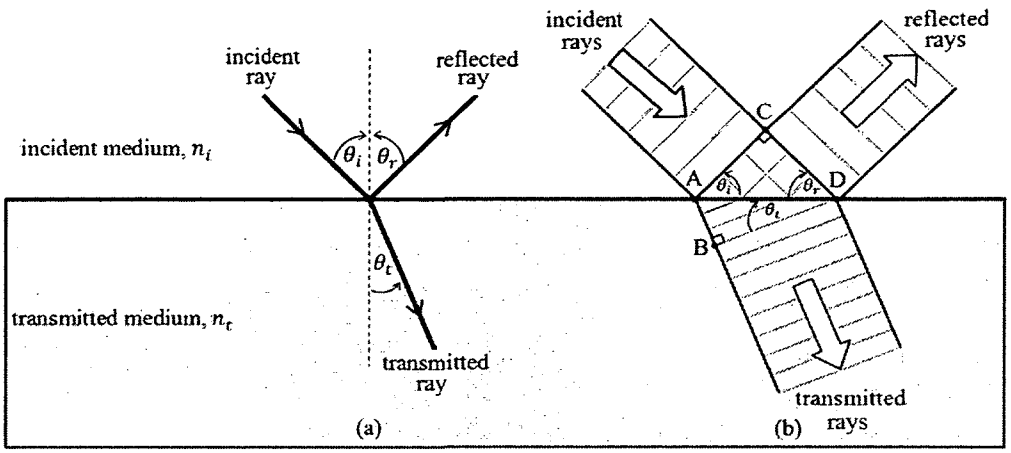

Figure 2.6. Light at a boundary as (a) a single ray and (b) successive rays.

Here, the media are classified in terms of its refractive index, n, with n_i being that of the incident medium, and n_t being that of the transmitting medium. The refractive index of a medium is defined as the ratio of the speed of light in free-space, c, to the speed of light in the medium, v (i.e. $n = c/v$). The speed of light in both free-space and the medium are given by equations 2.7a and 2.7b [3]:

$$c = f\lambda_o = \frac{\omega}{k_o} = \frac{1}{\sqrt{\varepsilon_o \mu_o}} \tag{2.7a}$$

$$v = f\lambda = \frac{\omega}{k} = \frac{1}{\sqrt{\varepsilon \mu}} \tag{2.7b}$$

where λ_o is the wavelength of the light in free-space, and k_o is the wave number of light in free-space ($k_o = 2\pi/\lambda_o$). Considering the relationships highlighted in equations 2.7a and 2.7b, the refractive index of a medium can be further defined as given by equation 2.8.

$$n = \frac{c}{v} = \frac{\lambda_o}{\lambda} = \sqrt{\varepsilon_r \mu_r} \tag{2.8}$$

It should be noted that the last portion of equation 2.8, which defines the refractive index of a medium in terms of its dielectric permittivity and magnetic permeability, only holds true at optical frequencies [3].

The laws governing the reflection and refraction of light at a boundary are known as the Laws of Reflection and Refraction, respectively. The former simply states that the angle of incidence equals the angle of reflection and can be geometrically derived by looking at the incident and reflected rays of figure 2.6(b). Recalling that all points on a plane wave front are of constant phase, and applying trigonometry, one obtains $\frac{\sin\theta_i}{CD} = \frac{\sin\theta_r}{AC}$. Since both the incident and reflected rays travel in the same medium, and thus at the same speed, v, it follows that in the time (Δt) it takes for point C on the incident wave front to reach point D on the surface, point A the surface reaches point C on the reflected wave front. In other words, $CD = v\Delta t = AC$, which yields the Law of Reflection as given by equation 2.9.

$$\theta_i = \theta_r \tag{2.9}$$

Similarly, looking at the incident and transmitted rays of figure 2.6(b), one obtains $\frac{\sin\theta_i}{CD} = \frac{\sin\theta_t}{AB}$. In this case, both the incident and transmitted rays travel in different media, and thus at different speeds (i.e. v_i and v_t). In the time (Δt) it takes for point C on the incident wave front to reach point D on the surface, point A the surface reaches point B on the transmitted wave front (i.e. $CD = v_i\Delta t$ and $AB = v_t\Delta t$). Substituting these conditions into the original expression, and multiplying both sides by c, yields the Law of Refraction, otherwise known as Snell's Law, as given by equation 2.10.

$$n_i \sin\theta_i = n_t \sin\theta_t \tag{2.10}$$

From this law, it follows that light entering a higher index medium (i.e. $n_i < n_t$), will bend towards the normal, whereas light entering a lower index medium (i.e. $n_i > n_t$), will bend away from the normal. In the latter case, a phenomenon known as total internal reflection occurs when the incident angle, θ_i, surpasses some critical angle, θ_c, such that its transmitted angle, θ_t, equals 90°. This is a special case of Snell's Law and is given by equation 2.11.

$$\sin\theta_c = \frac{n_t}{n_i} \tag{2.11}$$

For incident angles greater than the critical angle (i.e. $\theta_i > \theta_c$), the wave is said to undergo total internal reflection, however in reality an evanescent wave is transmitted.

2.2.2 Fresnel Equations for TM and TE Polarized Light

For the purpose of this thesis, all light incident upon an interface will be linearly polarized. A mathematical description of its incident, reflected and transmitted waves, respectively, for light incident upon a dielectric-dielectric interface are given by equations 2.12a – 2.12c [4].

$$\vec{E}_i = \vec{E}_{oi} e^{i(\vec{k}_i \cdot \vec{r})} \tag{2.12a}$$

$$\vec{E}_r = \vec{E}_{or} e^{i(\vec{k}_r \cdot \vec{r})} \tag{2.12b}$$

$$\vec{E}_t = \vec{E}_{ot} e^{i(\vec{k}_t \cdot \vec{r})} \tag{2.12c}$$

Furthermore, the boundary conditions, which follow from Maxwell's equations, state that the components of the $\vec{E}$- and $\vec{H}$-fields that are tangential to the surface are continuous across the interface, whereas the components that are normal are discontinuous [1], [4]. These are given by equations 2.13a – 2.13d:

$$E_{T1} = E_{T2} \tag{2.13a}$$

$$H_{T1} = H_{T2} \tag{2.13b}$$

$$\varepsilon_1 E_{N1} = \varepsilon_2 E_{N2} \tag{2.13c}$$

$$\mu_1 H_{N1} = \mu_2 H_{N2} \tag{2.13d}$$

where the subscripts T and N represent tangential and normal, respectively, while 1 and 2 represent medium one and two, respectively.

When dealing with a flat interface between two different materials, linearly polarized light can be further defined based on which field ($\vec{E}$ or $\vec{H}$) is transverse to the plane of incidence. When the $\vec{H}$-field is transverse to the plane of incidence, light is said to be transverse-magnetic (TM) polarized. Similarly, when the $\vec{E}$-field is transverse to the plane of incidence, light is said to be transverse-electric (TE) polarized. Figure 2.7 provides an illustration of incident TM polarized light, and its corresponding reflected and transmitted waves.

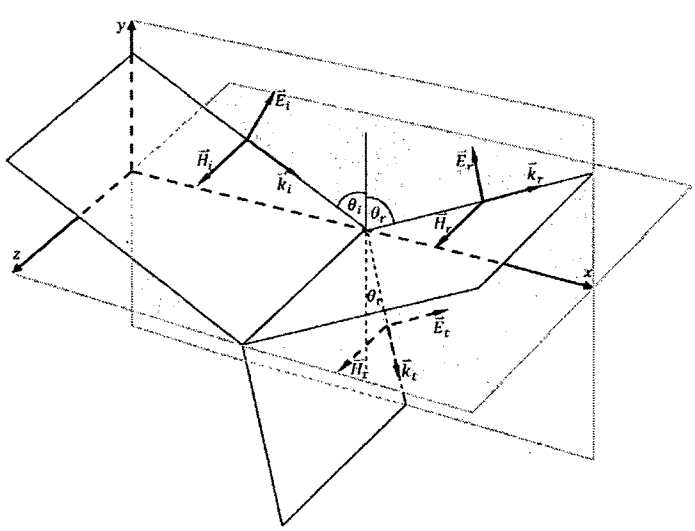

Figure 2.7. TM polarized light at a boundary.

As seen in figure 2.7, the plane of incidence lies within the x-y plane, while the boundary lies within the x-z plane (y= 0). The incident, reflected and transmitted waves as illustrated in figure 2.7 are given by equations 2.14a – 2.14c.

$$\vec{E}_i = \left(E_{oi}\cos\theta_i\,\vec{a}_x + E_{oi}\sin\theta_i\,\vec{a}_y\right)e^{i(\vec{k}_i\cdot\vec{r})} \tag{2.14a}$$

$$\vec{E}_r = \left(-E_{or}\cos\theta_r\,\vec{a}_x + E_{or}\sin\theta_r\,\vec{a}_y\right)e^{i(\vec{k}_r\cdot\vec{r})} \tag{2.14b}$$

$$\vec{E}_t = \left(E_{ot}\cos\theta_t\,\vec{a}_x + E_{ot}\sin\theta_t\,\vec{a}_y\right)e^{i(\vec{k}_t\cdot\vec{r})} \tag{2.14c}$$

Applying the continuity boundary conditions along with Maxwell's curl equations, and solving the resultant expressions to determine the amplitude effects of the reflected and transmitted waves (i.e. E_{or}/E_{oi} and E_{ot}/E_{oi}), yields the reflection and transmission coefficients (r_{TM} and t_{TM} respectively), otherwise known as Fresnel equations. For TM polarized light, these are given by equations 2.15a and 2.15b.

$$r_{TM} = \left(\frac{E_{or}}{E_{oi}}\right)_{TM} = \frac{n_t\cos\theta_i - n_i\cos\theta_t}{n_t\cos\theta_i + n_i\cos\theta_t} \tag{2.15a}$$

$$t_{TM} = \left(\frac{E_{ot}}{E_{oi}}\right)_{TM} = \frac{2n_i\cos\theta_i}{n_t\cos\theta_i + n_i\cos\theta_t} \tag{2.15b}$$

Figure 2.8 provides an illustration of TE polarized light, with the plane of incidence and the boundary again lying within the x-y and x-z planes, respectively.

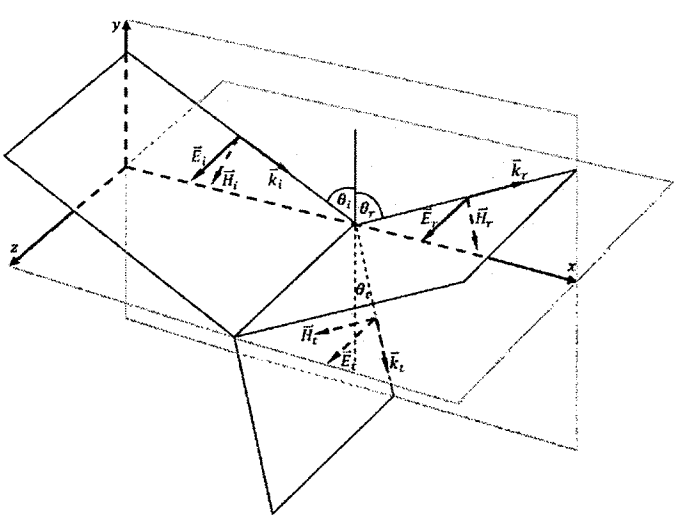

Figure 2.8. TE polarized light at a boundary.

Just as the Fresnel equations were obtained for TM polarized light, so too can they be obtained for TE polarized light, and are given by equations 2.16a and 2.16b.

$$r_{TE} = \left(\frac{E_{or}}{E_{oi}}\right)_{TE} = \frac{n_i \cos\theta_i - n_t \cos\theta_t}{n_i \cos\theta_i + n_t \cos\theta_t} \tag{2.16a}$$

$$t_{TE} = \left(\frac{E_{ot}}{E_{oi}}\right)_{TE} = \frac{2n_i \cos\theta_i}{n_i \cos\theta_i + n_t \cos\theta_t} \tag{2.16b}$$

From the reflection coefficients given by equations 2.15a and 2.16a, one can see that when the incident medium has a lower index than the transmitting medium, the reflection coefficient will always be negative. This accounts for the π radians (180°) phase shift seen in such reflected waves.

2.3 Diffraction of Light

2.3.1 Irradiance, Superposition and Interference of Light

When one talks about the amount of light illuminating a surface, one is referring to its irradiance. The irradiance of light is defined as its average energy per unit area per unit time given in $W \cdot m^{-2}$. The irradiance at point p, for a free-space, harmonic EM light wave is given by equation 2.17 [3]:

$$I_p = \varepsilon_o c \langle \vec{E}_p^2 \rangle = \varepsilon_o c \langle \vec{E}_p \cdot \vec{E}_p \rangle = \frac{\varepsilon_o c E_o^2}{2} \tag{2.17}$$

where $\langle \vec{E}_p^2 \rangle$ is the time-average of the square of the $\vec{E}$-field at point p, and E_o is the $\vec{E}$-field amplitude. The time average of the square of a sinusoidal function accounts for the factor of $1/2$.

Considering the case in which two mutually coherent light waves, $\vec{E}_1$ and $\vec{E}_2$, of the same frequency illuminate a surface, the *principle of superposition* states that when two or more waves are incident upon the same point, the net $\vec{E}$-field at any given point is

the vector sum of the constituent wave $\vec{E}$-fields at that point (i.e. $\vec{E}_p = \vec{E}_{p1} + \vec{E}_{p2}$). The irradiance at point p is then given by equation 2.18:

$$I_p = \varepsilon_o c\langle \vec{E}_{p1} \cdot \vec{E}_{p1} + \vec{E}_{p2} \cdot \vec{E}_{p2} + 2\vec{E}_{p1} \cdot \vec{E}_{p2} \rangle = I_{p1} + I_{p2} + I_{p12} \tag{2.18}$$

where I_{p1} and I_{p2} are the irradiances at point p due to the individual waves, while I_{p12} is the irradiance at point p due to the interference of the waves, given by equation 2.19 [4]:

$$I_{p12} = 2\sqrt{I_{p1} I_{p2}} \cos\varphi \tag{2.19}$$

where φ is the phase difference between the two waves, $\vec{E}_1$ and $\vec{E}_2$. If the waves originate from the same source, this phase difference accumulates as a result of a difference in path lengths travelled by the respective waves. Typically, $\cos\varphi$ will take on alternating maximum and minimum values, and interference fringes will appear in the observation plane. When $\cos\varphi = +1$ ($\varphi = 2m\pi$), constructive interference yields the maximum irradiance, $I_{p,max} = I_{p1} + I_{p2} + 2\sqrt{I_{p1} I_{p2}}$, whereas when $\cos\varphi = -1$ ($\varphi = (2m+1)\pi$), destructive interference yields the minimum irradiance, $I_{p,min} = I_{p1} + I_{p2} - 2\sqrt{I_{p1} I_{p2}}$. Here m represents some integer number. Furthermore, if the two waves have equal amplitudes, their irradiances are equal (i.e. $I_{p1} = I_{p2} = I_o$) and equation 2.18 will take the form given by equation 2.20.

$$I_p = 4I_o \cos^2\left(\frac{\varphi}{2}\right) \tag{2.20}$$

2.3.2 Single-Slit Diffraction

Diffraction of light occurs when a light wave encounters an obstacle within its path of comparable size to its wavelength. If the obstacle is much larger than the wavelength of light, the desired effect will not occur. The *Huygens-Fresnel principle* states that every unobstructed point of a wave front, at a given instant, serves as a source

of spherical secondary wavelets (with the same frequency as that of the primary wave). The amplitude of the optical field at any point beyond is the superposition of all these wavelets (considering their amplitude and relative phases) [3]. Thus, when a light wave encounters a fitting obstacle such as a single-slit opening, all but one of the effective wavelet sources are blocked, and the light coming through the slit behaves as a single point source, emerging in all directions instead of passing straight through.

Consider the free-space, EM plane wave passing through a single-slit of length much larger than width, b, as illustrated in figure 2.9. The Fraunhofer, or far-field, diffraction pattern can be derived by dividing the single-slit point source into infinitesimal lengths, ds.

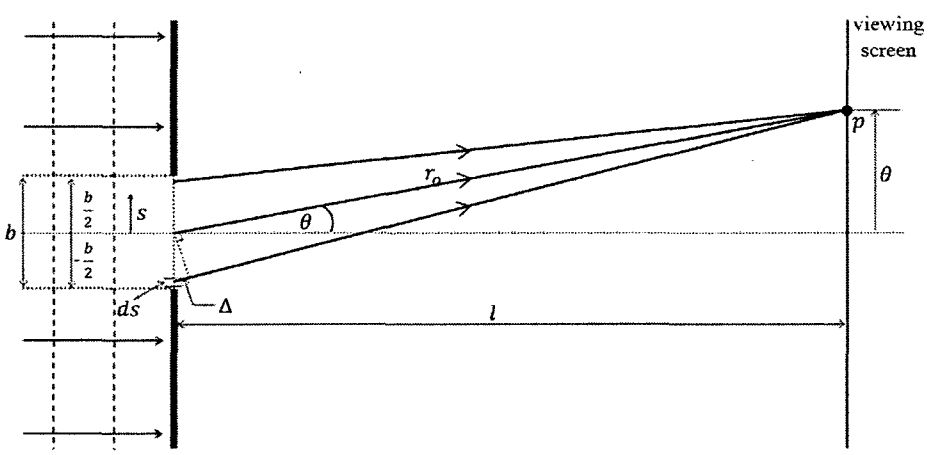

Figure 2.9. Single-slit diffraction geometry.

The change in the resultant $\vec{E}$-field at point p, along a viewing screen located a very large distance, l, from the slit opening, is given by equation 2.21:

$$dE_\theta = \left(\frac{E_l ds}{r_o}\right) e^{i[\vec{k}\cdot(\vec{r}_o + \vec{\Delta})]} \tag{2.21}$$

where E_l is a constant representing the $\vec{E}$-field strength of the point source, r_o is the reference optical path length from the center of the slit ($s = 0$), to point p, and Δ is the optical path length difference from the reference (which is ignored within the amplitude factor, since $\Delta << r_o$). Each length, ds, contributes to the wave at point p, thus by substituting the optical path length difference, $\Delta = s \sin\theta$, into equation 2.21, integrating over the entire slit width, b, substituting $\beta = \frac{1}{2} kb \sin\theta$ into the solution, and applying Euler's formula, an expression for the resultant $\vec{E}$-field at point p, is obtained and given by equation 2.22.

$$\vec{E}_\theta = \frac{E_l b}{r_o}\left(\frac{\sin\beta}{\beta}\right) e^{i(\vec{k}\cdot\vec{r}_o)} \tag{2.22}$$

Substituting this equation into equation 2.17, yields the irradiance at point p, given by equation 2.23:

$$I_\theta = \left(\frac{\varepsilon_o c}{2}\right) E_o^2 = \left(\frac{\varepsilon_o c}{2}\right)\left(\frac{E_l b}{r_o}\right)^2 \left(\frac{\sin^2\beta}{\beta^2}\right) = I_o\left(\frac{\sin^2\beta}{\beta^2}\right) \tag{2.23}$$

where I_o includes all constants. A plot of this equation is illustrated in figure 2.10. One can see that the single-slit diffraction pattern is given by the $\frac{\sin^2\beta}{\beta^2}$ function, with the primary maximum occurring at $\beta = 0$ (i.e. $\theta = 0$). Since the $lim_{\beta\to 0}\frac{\sin^2\beta}{\beta^2} = 1$, at the angle $\theta = 0$, the irradiance will be equal to $I_\theta = I_o$.

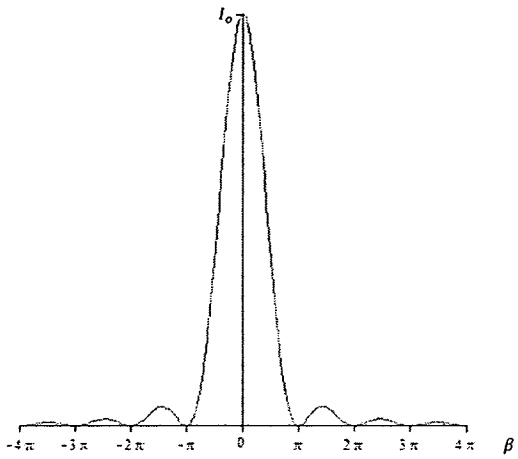

Figure 2.10. Single-slit diffraction pattern.

Subsequent maxima coincide with the maxima of the sinc function, as solutions to equation 2.24, whereas the minima coincide with the solutions to $\sin\beta = 0$ (with the exception of $\beta = 0$).

$$\frac{\partial}{\partial\beta}\left(\frac{\sin^2\beta}{\beta^2}\right) = \frac{\beta\cos\beta - \sin\beta}{\beta^2} = 0 \tag{2.24}$$

2.3.3 Multiple-Slit Diffraction

Now consider the same conditions as with the single-slit, but with a double-slit of spacing, a, as illustrated in figure 2.11.

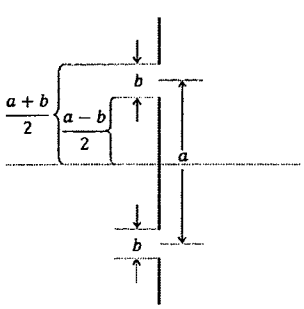

Figure 2.11. Double-slit diffraction geometry.

Integrating equation 2.21 over the slit widths, substituting β and $\alpha = \frac{1}{2}ka\sin\theta$ into the solution, and applying Euler's formula, an expression for the resultant $\vec{E}$-field at point p, is obtained and given by equation 2.25.

$$E_\theta = \frac{2E_l b}{r_o}\left(\frac{\sin\beta}{\beta}\right)(\cos\alpha)e^{i(\vec{k}\cdot\vec{r}_o)} \tag{2.25}$$

The irradiance at point p, is then given by equation 2.26.

$$I_\theta = 4I_o\left(\frac{\sin^2\beta}{\beta^2}\right)\cos^2\alpha \tag{2.26}$$

One can see that the double-slit diffraction pattern is the product of the single-slit diffraction envelope, $\frac{\sin^2\beta}{\beta^2}$, and the double-slit interference pattern, $\cos^2\alpha$. Figure 2.12(a) illustrates separate plots of both the single-slit diffraction envelope (dashed) and the double-slit interference pattern (solid), whereas figure 2.12(b) illustrates a single plot of the product.

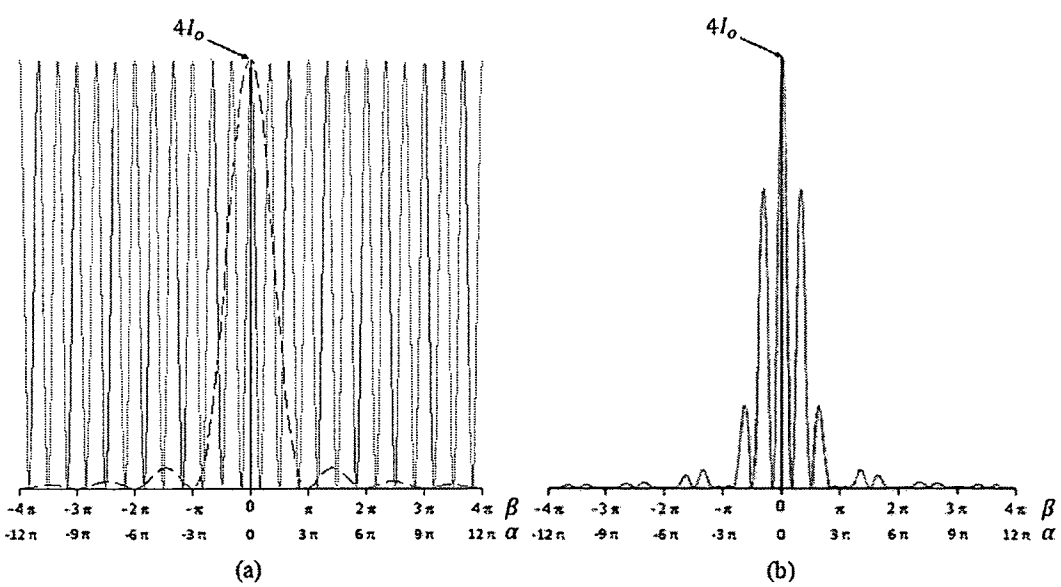

Figure 2.12. Double-slit diffraction pattern (a) separated and (b) combined.

The maximum irradiance of the double-slit configuration, occurring at an angle, $\theta = 0$, has a value of $4I_o$, compared to the I_o maximum of the single-slit. This is expected when the two $\vec{E}$-fields are in phase and interfere constructively. The interference maxima are also known as diffraction orders, and occur when $\alpha = m\pi$. This corresponds to the maxima condition given by equation 2.27:

$$m\lambda = a \sin \theta_m \tag{2.27}$$

where θ_m is the angle of diffraction of the diffracted order, m. The slit-width, b, does not affect the position of these interference maxima, only the envelope function. When the diffraction envelope minima correspond to the interference maxima, missing orders will exist in the diffraction pattern.

The irradiance at point p, for the generic case of N-slits, derived in a similar manner as above, is given by equation 2.28 [4]:

$$I_\theta = I_o \left(\frac{\sin^2\beta}{\beta^2}\right)\left(\frac{\sin^2 N\alpha}{\sin^2\alpha}\right) \tag{2.28}$$

where $\frac{\sin^2 N\alpha}{\sin^2\alpha}$ is the multiple-slit interference pattern. When $N = 1$ and $N = 2$, equation 2.28 will reduce to equations 2.23 and 2.26, respectively. Figure 2.13 illustrates a plot of equation 2.28 for $N = 4$. The maximum irradiance of the multiple-slit configuration, once again occurring at an angle, $\theta = 0$, has a value of $N^2 I_o$.

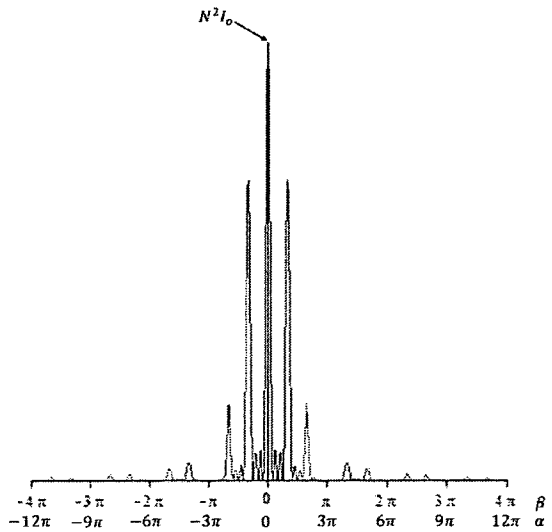

Figure 2.13. Four-slit diffraction pattern.

The principal interference maxima (i.e. diffraction orders) occur for the same conditions given earlier by equation 2.27. In between these successive maxima, there exist $N-2$ secondary interference peaks and $N-1$ interference minima [4].

2.3.4 Diffraction Gratings and the Grating Equation

The multiple-slits discussed above are in fact collectively known as a diffraction grating – a repetitive array of transmitting or reflecting elements separated by a distance comparable to the wavelength of light under study [5]. Figure 2.14 illustrates the diffraction of light at oblique incidence into multiple orders using both reflective (dashed lines) and transmissive (solid lines) gratings. The 0th order of interference ($m = 0$), occurs at $\theta_0 = -\theta_i$, and does not diffract. Subsequent orders of light however, will be diffracted, and are classified based on their position with respect to the 0th order. Beams diffracted to the right of the 0th order are considered positive orders, whereas beams to the left are considered negative orders.

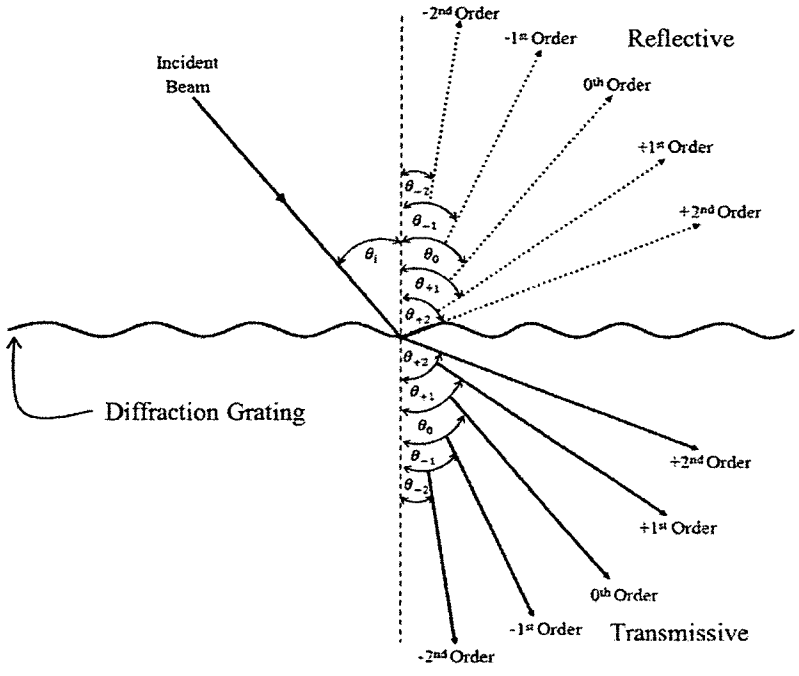

Figure 2.14. Diffraction of light using both reflective and transmissive gratings.

The directions of the diffracted orders are dependent upon the grating spacing, Λ, the wavelength of the incident light, λ, and the incident angle, θ_i, and can be found by applying simple geometry to successive elements within a grating. Figure 2.15 illustrates this geometry applied to successive elements of a reflective grating.

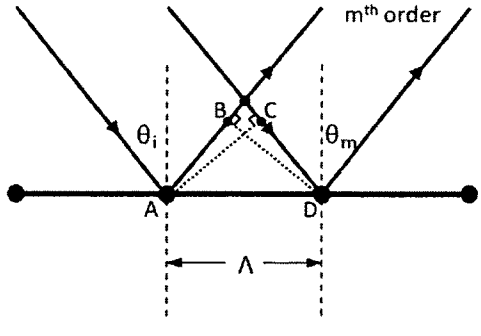

Figure 2.15. Successive element reflective grating geometry.

One can see that the net path difference between rays from successive elements equals $AB - CD$. Applying the proper trigonometric relations, one obtains equation 2.29.

$$AB - CD = \Lambda(sin\,\theta_m - sin\,\theta_i) \tag{2.29}$$

When the incident and diffracted rays are on the same side of the grating normal, θ_m takes on the same sign convention as θ_i, whereas if they are on opposite sides, the reverse is true. In order for the resultant interference pattern to be maximum, the net path difference must equal some order of interference (i.e. $AB - CD = m\lambda$). Isolating the diffracted angle, one obtains equation 2.30.

$$sin\,\theta_m = sin\,\theta_i \pm \frac{m\lambda}{\Lambda} \tag{2.30}$$

This equation can also be thought of in terms of the wave vector, $\vec{k}$. Recall that for an EM plane wave, the wave vector points in the direction of propagation and has a magnitude of $|\vec{k}| = k = 2\pi/\lambda$. Including the wave vector contribution in equation 2.30, yields equation 2.31:

$$k\sin\theta_m = k\,sin\,\theta_i \pm \frac{2\pi m}{\Lambda} \tag{2.31}$$

where $\frac{2\pi}{\Lambda}$ represents the magnitude of the grating vector, K, defined in a direction perpendicular to the grating ruling, while $k\sin\theta_m$ and $k\,sin\,\theta_i$ represent the diffracted and reflected wave vector components of the light along this grating vector, respectively. Substituting the parameters k_{light} and K for $k\sin\theta_m$ and $\frac{2\pi}{\Lambda}$ respectively, yields equation 2.32.

$$k_{light} = k\,sin\,\theta_i \pm mK \tag{2.32}$$

This equation is known as the grating equation, and represents the wave vector component of the diffracted light along the grating vector. It is valid for both transmissive and reflective diffraction gratings.

Figure 2.16 provides a schematic of the grating equation in light momentum space for a reflective grating at oblique incidence, with the 0th, $\pm 1^{st}$, and -2nd orders being shown. As one can see, k_{light} has contributions from both the wave vector component of the reflected wave along the grating vector as well as the grating vector itself.

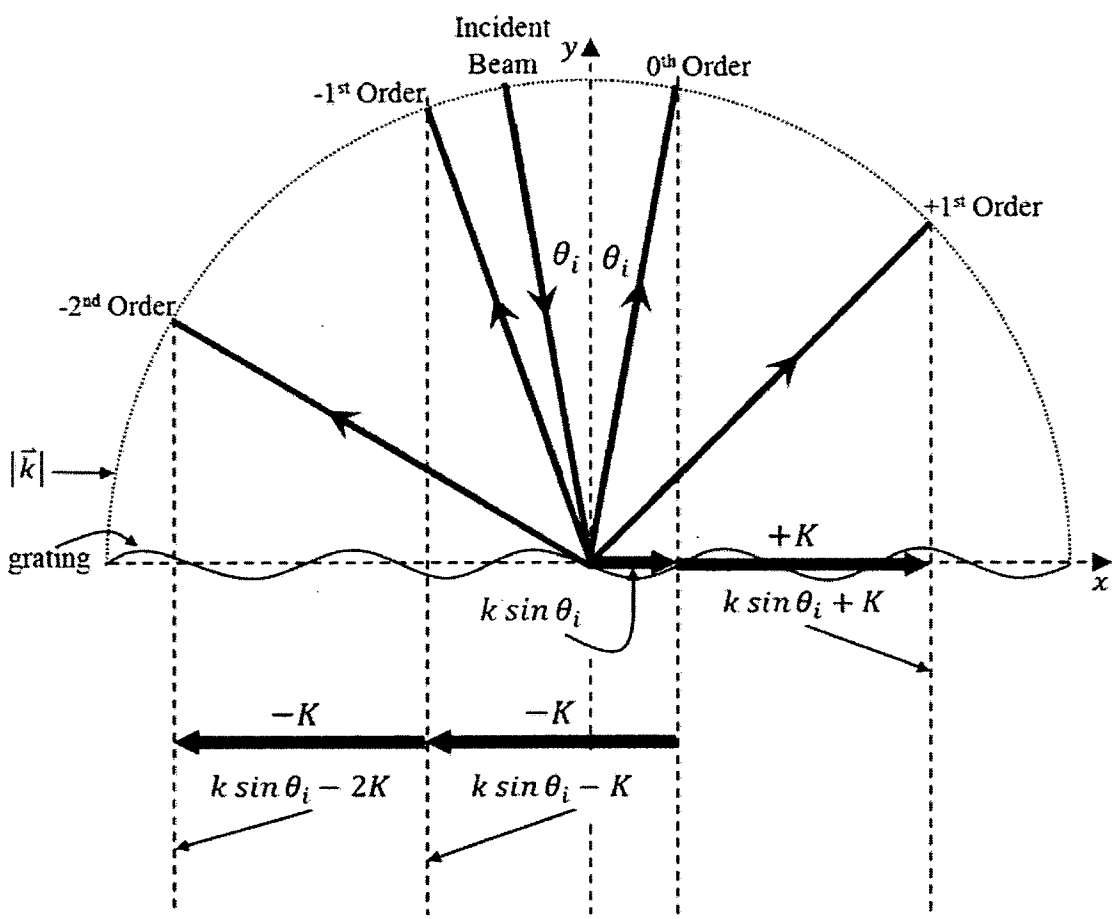

Figure 2.16. Schematic of the grating equation in light momentum space.

For a reflective grating, if the grating spacing was fixed, but the angle of incidence was increased, all orders would sweep in a CW-direction, whereas if the angle of incidence was decreased, all orders would sweep in a CCW-direction. Conversely, if the angle of incidence was fixed, but the grating spacing was increased (i.e. K decreased), all orders would sweep in a CCW-direction, whereas if the grating spacing was decreased (i.e. K increased), all orders would sweep in a CW-direction. Since each wavelength is diffracted at a slightly different angle, if the incident light is polychromatic in nature, it will be dispersed into its constituent wavelengths.

It should be noted that reflective gratings with spacings on the order of the wavelength of light will be used throughout this thesis. As such, at normal incidence as $\lambda/\Lambda \rightarrow 1$, then $\sin\theta_m \rightarrow 1$ for $m = 1$, and the position of the non-zero orders would spread out, until only the $\pm 1^{st}$ orders remain. Therefore, only the $\pm 1^{st}$ orders are of real concern.

2.4 Surface Plasmon (SP) Grating Excitation

2.4.1 Mathematical Description of Surface Plasmons (SPs)

Recall from chapter 1 that SPs are defined as light induced surface electron density fluctuations that collectively and coherently oscillate in resonance with the incident light along the interface between any two materials in which the real portion of the dielectric permittivity changes sign across the interface. These collective oscillations yield a combined EM wave and surface charge character as shown in figure 2.17 [6], [7].

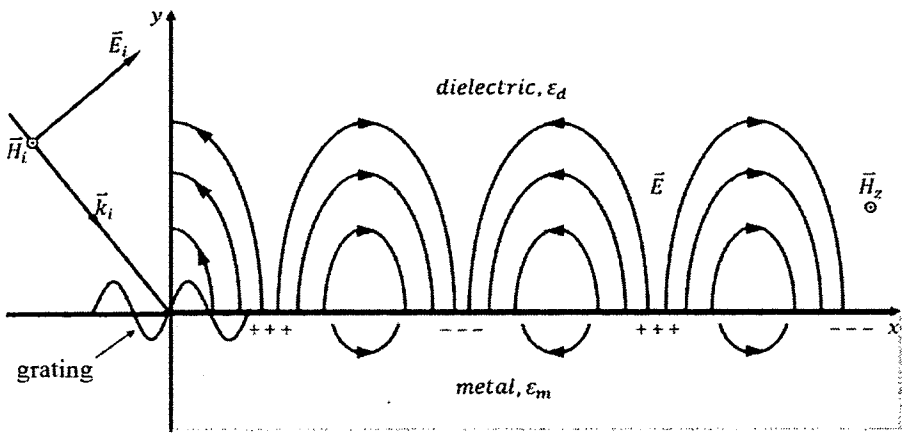

Figure 2.17. TM polarized light incident upon a dielectric-metal interface at y = 0.

Furthermore, it is known that when using the grating method for SP excitation, only incident light with an $\vec{E}$-field component along the grating vector will excite SPs [8]. This condition will be satisfied with both TM and TE polarized incident light, *provided* the grating is oriented properly. Figure 2.17 illustrates the grating orientation for TM polarized light.

Due to the evanescent nature of SPs, the surface-propagating waves will be enhanced near the surface, but decay with distance away from it. As seen in figure 2.17, this translates into an $\vec{E}$-field that propagates along the x-axis, has its maximum at $y = 0$, and vanishes at $|y| \to \infty$ within both media. Mathematically, evanescent waves are characterized by the fact that as least one component of the wave vector is imaginary [9]. In this case the wave vector is $\vec{k} = k_x + ik_y$, and the evanescent EM fields within the dielectric ($y > 0$) are given by equations 2.33a and 2.33b [10], [11].

$$y > 0\text{: } \vec{E}_d = \left(E_{x,d}, E_{y,d}, 0\right)e^{i\left(k_{x,d}x + ik_{y,d}y\right)} \tag{2.33a}$$

$$y > 0\text{: } \vec{H}_d = \left(0, 0, H_{z,d}\right)e^{i\left(k_{x,d}x + ik_{y,d}y\right)} \tag{2.33b}$$

Similarly, the fields within the metal ($y < 0$) can be given by equations 2.34a and 2.43b.

$$y < 0\text{:}\ \vec{E}_m = \left(E_{x,m}, E_{y,m}, 0\right)e^{i\left(k_{x,m}x + ik_{y,m}y\right)} \tag{2.34a}$$

$$y < 0\text{:}\ \vec{H}_m = \left(0, 0, H_{z,m}\right)e^{i\left(k_{x,m}x + ik_{y,m}y\right)} \tag{2.34b}$$

2.4.2 Surface Plasmon (SP) Dispersion Relation

The angular frequency, ω, of these electron density fluctuations is tied to its wave vector component, k_x, by a dispersion relation, $\omega(k_x)$. The wave number, previously written as $|\vec{k}| = k = 2\pi/\lambda$, can also be expressed in terms of the angular frequency, ω, dielectric permittivity, ε, and magnetic permeability, μ, as given by equation 2.35 [8].

$$k^2 = \omega^2\mu\varepsilon \tag{2.35}$$

Re-writing Maxwell's curl equation as given by equation 2.1d to account for changing media, one obtains equation 2.36, where the subscript med is simply used to denote the applicable medium (i.e. dielectric or metal).

$$\nabla \times \vec{H}_{med} = -i\omega\tilde{\varepsilon}_{med}\vec{E}_{med} \tag{2.36}$$

It is known that an evanescent wave (SP) which propagates along the interface and extends into each adjacent media exists [8], [7], therefore the metal is assumed to be a *non-perfect* conductor. As such, the boundary conditions stating the continuity and discontinuity of the tangential and normal components, respectively, of the $\vec{E}$- and $\vec{H}$-fields of the evanescent wave are expressed by equations 2.37a – 2.37c.

$$E_{x,d} = E_{x,m} \tag{2.37a}$$

$$H_{z,d} = H_{z,m} \tag{2.37b}$$

$$\varepsilon_d E_{y,d} = \tilde{\varepsilon}_m E_{y,m} \tag{2.37c}$$

Applying equation 2.36 to equations 2.33 and 2.34, one obtains the relationship given by equation 2.38.

$$\left(ik_{y,med}H_{z,med}, -ik_{x,med}H_{z,med}, 0\right) = \left(-i\omega\tilde{\varepsilon}_{med}E_{x,med}, -i\omega\tilde{\varepsilon}_{med}E_{y,med}, 0\right) \quad (2.38)$$

This relationship separated for both the dielectric and metal, yields equations 2.39a – 2.39d.

$$ik_{y,d}H_{z,d} = -i\omega\varepsilon_d E_{x,d} \quad (2.39a)$$

$$ik_{y,m}H_{z,m} = -i\omega\tilde{\varepsilon}_m E_{x,m} \quad (2.39b)$$

$$-ik_{x,d}H_{z,d} = -i\omega\varepsilon_d E_{y,d} \quad (2.39c)$$

$$-ik_{x,m}H_{z,m} = -i\omega\tilde{\varepsilon}_m E_{y,m} \quad (2.39d)$$

Applying the boundary conditions given by equations 2.37a and 2.37b to equations 2.39a and 2.39b, yields equation 2.40.

$$\frac{k_{y,d}}{\varepsilon_d} = \frac{k_{y,m}}{\tilde{\varepsilon}_m} \quad (2.40)$$

Likewise, applying the boundary conditions given by equations 2.39b and 2.39c to equations 2.39c and 2.39d, yields equation 2.41.

$$k_{x,d} = k_{x,m} \equiv k_x \quad (2.41)$$

Combining equations 2.35 and 2.41, yields equation 2.42:

$$k_{med}^2 = k_x^2 + k_{y,med}^2 = \omega^2\mu_{med}\varepsilon_{med} \quad (2.42)$$

Finally, manipulating equations 2.40 and 2.42 for non-magnetic media, and solving for k_x, one obtains the SP dispersion relation for a *flat interface* as given by equation 2.43:

$$k_{SP} = k_x = \frac{\omega}{c}\sqrt{\frac{\varepsilon_{r,d}\tilde{\varepsilon}_{r,m}}{\varepsilon_{r,d}+\tilde{\varepsilon}_{r,m}}} = k_x' + ik_x'' \tag{2.43}$$

where the subscript r is used to denote the relative dielectric permittivity. Since the dielectric-metal interface used in this thesis has the sinsusoidal profile of the diffraction grating, this SP dispersion relation is considered an approximation (i.e. grating depth $\ll$ SP propagation length along the interface).

Similarly, an approximation for the normal component of the wave vector into the applicable medium can be derived as given by equations 2.44a and 2.44b.

$$k_{y,d} = \frac{\omega}{c}\sqrt{\frac{\varepsilon_{r,d}^2}{\varepsilon_{r,d}+\tilde{\varepsilon}_{r,m}}} = k_{y,d}' + ik_{y,d}'' \tag{2.44a}$$

$$k_{y,m} = \frac{\omega}{c}\sqrt{\frac{\tilde{\varepsilon}_{r,m}^2}{\varepsilon_{r,d}+\tilde{\varepsilon}_{r,m}}} = k_{y,m}' + ik_{y,m}'' \tag{2.44b}$$

Recall from equation 2.3 that the effective dielectric permittivity of a metal, has both real and imaginary components (i.e. $\tilde{\varepsilon}_{r,m} = \tilde{\varepsilon}_{r,m}' + i\tilde{\varepsilon}_{r,m}''$). Therefore, equations 2.43 and 2.44 will have both a real component, k', representing wave propagation and an imaginary component, k'', representing wave attenuation. The *real* portion of equations 2.43 and 2.44 are given by equations 2.45 and 2.46, respectively [12], [13].

$$k_{SP}' = k_x' = \frac{\omega}{c}\sqrt{\frac{\varepsilon_{r,d}\tilde{\varepsilon}_{r,m}'}{\varepsilon_{r,d}+\tilde{\varepsilon}_{r,m}'}} \tag{2.45}$$

$$k_{y,d}' = \frac{\omega}{c}\sqrt{\frac{\varepsilon_{r,d}'^2}{\varepsilon_{r,d}+\tilde{\varepsilon}_{r,m}'}} \tag{2.46a}$$

$$k_{y,m}' = \frac{\omega}{c}\sqrt{\frac{\tilde{\varepsilon}_{r,m}'^2}{\varepsilon_{r,d}+\tilde{\varepsilon}_{r,m}'}} \tag{2.46b}$$

As discussed earlier, in order for an evanescent wave to exist along the interface, k'_x must remain real, whereas $k'_{y,med}$ must be purely imaginary. This condition represents the EM wave, propagating strictly along the interface, with evanescent tails extending into both sides of the interface. Looking at equations 2.45 and 2.46, and knowing that $\varepsilon_{r,d}$ is positive, the dielectric permittivity conditions required for SPs to exist are given by equations 2.47a and 2.47b .

$$\tilde{\varepsilon}'_{r,m} < 0 \tag{2.47a}$$

$$\tilde{\varepsilon}'_{r,m} < -\varepsilon_{r,d} \tag{2.47b}$$

The SP wavelength, λ, and the SP propagation length, δ_{SP}, can be found using the real and imaginary portions of equation 2.43, respectively [12]. Similiarly, the SP dielectric decay length, δ_d, and the SP metal decay length, δ_m, can be found using equations 2.44a and 2.44b, respectively [12], [14].

2.4.3 Drude Model for Dielectric Permittivity

At optical frequencies, an approximation for the real portion of the relative effective dielectric permittivity of a metal, $\tilde{\varepsilon}'_{r,m}$, as predicted by the Drude model, is given by equation 2.48 [2], [7], [8], [15], [16]:

$$\tilde{\varepsilon}'_{r,m} \approx 1 - \frac{\omega_P^2}{\omega^2} \tag{2.48}$$

where ω_P is the characteristic plasma frequency of the metal. In the infrared and visible regions, the optical frequency is usually significantly lower than the plasma frequency [2]. Thus, the $-\omega_P^2/\omega^2$ term is predominant in the right-hand side of equation 2.48, yielding a negative real number (i.e. condition given by equation 2.47a). Applying the condition

given by equation 2.47b to equation 2.48, one can obtain the maximum angular frequency for which SPs will exist as given by equation 2.49.

$$\tilde{\varepsilon}'_{r,m} = 1 - \frac{\omega_P^2}{\omega^2} = -\varepsilon_{r,d} \rightarrow \omega = \omega_{max} = \frac{\omega_P}{\sqrt{1+\varepsilon_{r,d}}} \tag{2.49}$$

A plot of the relative dielectric permittivities of both a dielectic and a metal are illustrated in figure 2.18 [13].

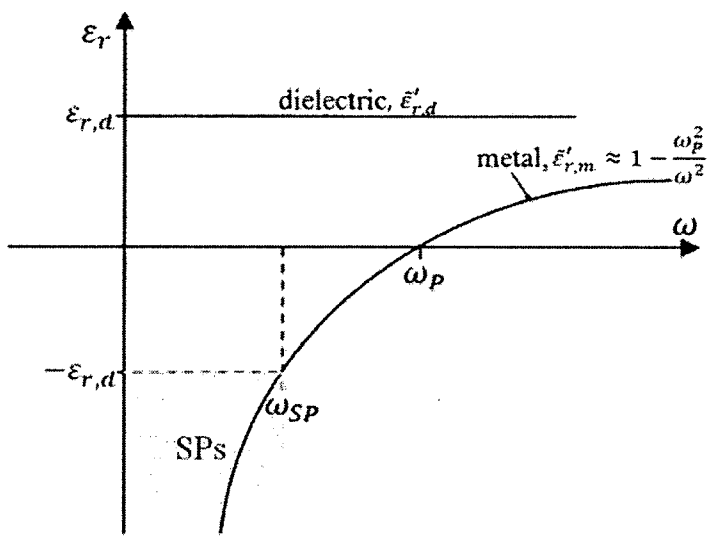

Figure 2.18. Relative dielectric permittivity plot for a dielectric and a metal.

2.4.4 Surface Plasmon (SP) Dispersion Curve

An illustration of the SP dispersion relation, along with its dielectric permittivity conditions and corresponding limitations, as given by equation 2.45 is provided in figure 2.19. Note that the plot is symmetrical about the ω-axis.

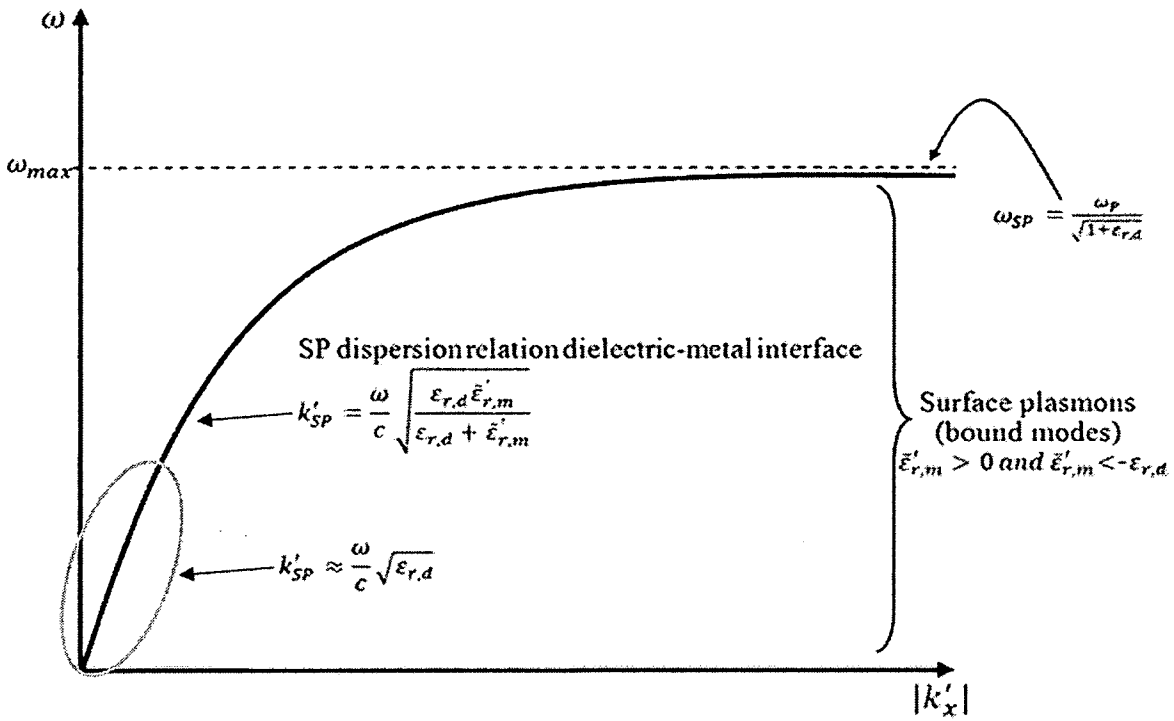

Figure 2.19. SP dispersion relation plot.

In order to examine how the SP dispersion relation will behave at both its upper and lower limits, the limits of k'_{SP} as $\tilde{\varepsilon}'_{r,m}$ approaches $-\infty$ and $-\varepsilon_{r,d}$ are taken, respectively, and given by equations 2.50a and 2.50b.

$$\lim_{\tilde{\varepsilon}'_{r,m}\to-\infty} k'_{SP} = \frac{\omega}{c}\lim_{\tilde{\varepsilon}'_{r,m}\to-\infty}\sqrt{\frac{\varepsilon_{r,d}\tilde{\varepsilon}'_{r,m}}{\varepsilon_{r,d}+\tilde{\varepsilon}'_{r,m}}} \approx \frac{\omega}{c}\sqrt{\varepsilon_{r,d}} \tag{2.50a}$$

$$\lim_{\tilde{\varepsilon}'_{r,m}\to-\varepsilon_{r,d}} k'_{SP} \to \infty \tag{2.50b}$$

One can see from both figure 2.19 and equation 2.50 that at lower frequencies, the SP dispersion relation *approaches* that of light in a dielectric [14] (i.e. as $\tilde{\varepsilon}'_{r,m} \to -\infty$, $k'_{SP} \to \frac{\omega}{c}\sqrt{\varepsilon_{r,d}}$), whereas at higher frequencies, it approaches infinity (i.e. as $\tilde{\varepsilon}'_{r,m} \to$

$-\varepsilon_{r,d}$, $k_{SP} \rightarrow \infty$). The maximum frequency for which SPs will exist, ω_{max}, is shown in figure 2.19 as a horizontal asymptote dashed line.

2.4.5 Surface Plasmon (SP) Excitation Condition

While the SP dispersion relation approaches that of light at lower frequencies, the two will never intersect (i.e. SPs will never be excited), without some boost to the tangential wave vector, k_x, of the incident light. As discussed earlier, light diffracted from a grating will acquire a boost its wave vector component along the direction of the grating vector. Recall from equation 2.32 that the magnitude of the diffracted wave vector has contributions from both the wave vector component of the reflected wave along the grating vector, as well as the grating vector itself. Considering a diffraction grating that is oriented with its grating vector along the x-axis, and incident light that is oriented such that it has an $\vec{E}$-field component along the grating vector (x-axis), as previously illustrated in figure 2.17. By matching the k_{light} given by equation 2.32 to that of $k_{SP}^{'}$ given by equation 2.45 one will obtain the relationship governing the excitation of SPs via the grating method. Assuming $\pm 1^{st}$ order diffraction, equation 2.32 can be re-written as equation 2.51.

$$k_{light} = k \sin \theta_i \pm K \tag{2.51}$$

Since $k_o = \frac{\omega}{c}$ and $n_d = \sqrt{\varepsilon_{r,d}}$, equation 2.45 can be re-written as equation 2.52.

$$k_{SP}^{'} = k_o n_d \sqrt{\frac{\tilde{\varepsilon}_{r,m}^{'}}{n_d^2 + \tilde{\varepsilon}_{r,m}^{'}}} \tag{2.52}$$

Equating equation 2.51 to equation 2.52, one obtains equation 2.53.

$$k_{SP}^{'} = k_o n_d \sqrt{\frac{\tilde{\varepsilon}_{r,m}^{'}}{n_d^2 + \tilde{\varepsilon}_{r,m}^{'}}} = k \sin\theta_i \pm K \tag{2.53}$$

Therefore, the SP excitation wavelength, λ_{SP}, is given in terms of the refractive index of the dielectric, n_d, the real portion of the relative dielectric permittivity of the metal, $\tilde{\varepsilon}_{r,m}^{'}$, the incident angle, θ_i, and the grating spacing, Λ, by equation 2.54 [17], [18], [19].

$$\lambda_{SP} = n_d \left(\sqrt{\frac{\tilde{\varepsilon}_{r,m}^{'}}{n_{r,d}^2 + \tilde{\varepsilon}_{r,m}^{'}}} \mp \sin\theta_i \right) \Lambda \tag{2.54}$$

Here the equation takes on the form of $-\sin\theta_i$, for $+K$, and vice versa.

For an air-silver (dielectric-metal) interface at 650 nm, $n_d \approx 1$, and $\tilde{\varepsilon}_{r,m}^{'} \approx -19.552$ [20], equation 2.54 becomes $\lambda_{SP} \approx (1.027 \mp \sin\theta_i)\Lambda$. Thus, for an air-silver interface at normal incidence, with a grating spacing of $\Lambda = 640$ nm, the SP excitation wavelength is $\lambda_{SP} \approx 657$ nm. Similarly, for a PVA-silver interface at 650 nm, $n_d \approx 1.525$ [21], and $\lambda_{SP} \approx 1.525(1.065 \mp \sin\theta_i)\Lambda$. For this interface at normal incidence, with a grating spacing of $\Lambda = 400$ nm, the SP excitation wavelength becomes $\lambda_{SP} \approx 650$ nm. Figure 2.20 provides an illustration of the matching condition required for the excitation of SPs via the grating method. At normal incidence the $k \sin\theta_i$ terms dissappear, yielding a single λ_{SP}.

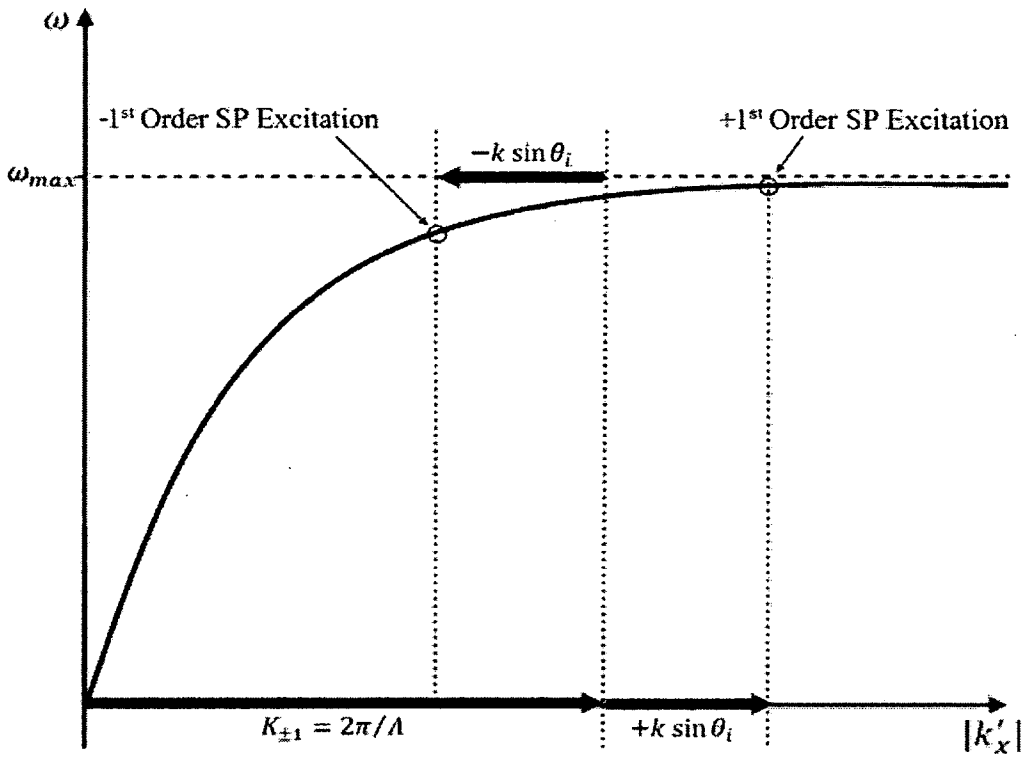

Figure 2.20. SP excitation matching condition plot.

The SP excitation points highlighted above represent the intersection of the $\pm 1^{st}$ order diffracted light lines with the SP dispersion curve. This corresponds to the matching condition, $k'_{SP} = k_{light}$, which is satisfied by the free-space SP wavelength, λ_{SP}, given by equation 2.54.

REFERENCES

[1] M. Sadiku, Elements of Electromagnetics, 4th Ed., New York: Oxford University Press, 2007.

[2] J. Lourtioz, H. Benisty, D. Pagnoux, V. Berger, J. Gerard and D. Maystre, "Photonic Crystals: Towards Nanoscale Photonic Devices, 2nd Ed.," Springer-Verlag, Berlin, 2008.

[3] E. Hecht, Optics, 4th Ed., San Francisco: Pearson Addison-Wesley, 2002.

[4] F. Pedrotti, L. Pedrotti and L. Pedrotti, Introduction to Optics, 3rd Ed., San Francisco: Pearson Addison-Wesley, 2007.

[5] C. Palmer, Diffraction Grating Handbook, 5th Ed., Rochester: Richardson Grating Laboratory, 2002.

[6] W. Barnes, "Surface Plasmon Subwavelength Optics," *Nature,* vol. 424, no. 6950, pp. 824-830, 2003.

[7] H. Reather, "Chapter 2 - Surface Plasmons on Smooth Surfaces," in *Surface Plasmons on Smooth and Rough Surfaces and on Gratings*, London, Springer-Verlag, 1988, pp. 4-39.

[8] R. Kooyman, "Chapter 2 - Physics of Surface Plasmon Resonance," in *Handbook of Surface Plasmon Resonance*, Cambridge, The Royal Society of Chemistry, 2008, pp. 15-34.

[9] L. Novotny and B. Hecht, Principles of Nano-Optics, Cambridge: Cambridge University Press, 2006.

[10] J. Pitarke, V. Silkin, E. Chulkov and P. Echenique, "Theory of Surface Plasmons and Surface-Plasmon Polaritons," *Reports on Progress in Physics,* vol. 70, pp. 1-87, 2007.

[11] A. Zayats, I. Smolyaninov and A. Maradudin, "Nano-Optics of Surface Plasmon Polaritons," *Physics Reports,* vol. 408, no. 3-4, pp. 131-314, 2005.

[12] W. Barnes, "Surface Plasmon-Polariton Length Scales: A Route to Sub-Wavelength Optics," *Journal of Optics A: Pure and Applied Optics,* vol. 8, pp. S87-S93, 2006.

[13] V. Shalaev, "ECE 695s Lecture 9: Introduction to Metal Optics," Purdue University, 5 October 2006. [Online]. Available: http://nanohub.org/resources/1850/play. [Accessed 20 December 2011].

[14] F. Yu, "Surface Plasmon Fluorescence Spectroscopy and Surface Plasmon Diffraction in Bimolecular Interaction Studies," Max Planck Institute for Polymer Research , Mainz, 2004.

[15] C. Sönnichsen., "Plasmons in Metal Nanostructures," Ludwig Maximilian University of Munich, Munich, 2001.

[16] K. Welford, "Surface Plasmon-Polaritons and their Uses," *Optical and Quantum Electronics,* vol. 23, no. 1, pp. 1-27, 1991.

[17] R. Sabat, M. Santos and P. Rochon, "Surface Plasmon-Induced Band Gap in the Photocurrent Response of Organic Solar Cells," *International Journal of Photoenergy,* vol. 2010; p. 698718, 2010.

[18] R. Sabat, N. Rochon and a. P. Rochon, "Dependence of Surface Plasmon Polarization Conversion on the Grating Pitch," *Journal of the Optical Society of America A,* vol. 27, no. 3, pp. 518-522, 2010.

[19] L. Levesque and P. Rochon, "Surface Plasmon Photonic Bandgap in Azopolymer Gratins Sputtered with Gold," *Journal of the optical Society of America A,* vol. 22, no. 11, pp. 2564-2568, 2005.

[20] M. Weber, Handbook of Optical Materials, Boca Raton: CRC Publishing, 2003.

[21] R. Kumar, A. Singh, A. Kapoor and K. Tripathi, "Fabrication and Characterization of Polyvinyl-Alcohol-based Thin-Film Optical Waveguides," *Optical Engineering,* vol. 43, no. 9, pp. 2134-2142, 2004.

CHAPTER 3: SURFACE PLASMON (SP) OPTIMIZATION

Chapter three is designed to provide the reader with the methodology used, and results obtained, during the SP optimization trials. The entire experimental procedure will be discussed, beginning with the fabrication and continuing through to test sample result analysis. Generic manufacturing considerations and techniques will be discussed, followed by the presentation and discussion of results. The results will be arranged based on sample structure, with those relating to SP generation at an air-silver (Ag) interface being provided first, followed by those relating to SP generation at a PVA-Ag interface. All manufacturing and analytical related apparatuses will be illustrated and discussed.

3.1 Test Sample Fabrication Process

3.1.1 Azopolymers and Grating Inscription

Azopolymers have for some time proven to be an attractive basis for the single-step, optical formation of surface-relief diffraction gratings [1]. Due to its availability and proven success in producing such gratings [2], [3], the compound poly[4-nitrophenyl-4′-[[2-(methacryloyloxy)ethyl]ethyl-amino]phenyldiazene] (pDR1M) was the azopolymer of choice for grating fabrication within this thesis. The pDR1M azopolymer was first dissolved in dichloromethane with a mix ratio of 3% weight/weight before being thoroughly mixed using a mechanical shaker. Once completely dissolved, the solution was passed through a 0.45 μm nylon syringe filter. An ~200 nm thin film of the solution was then spin-coated onto a clean BK7 glass slide, and subsequently baked at 90°C for 1 hour to remove any remaining solvent. The thickness of the film was regulated by controlling the RPM of the spin-coater, and verified after being baked using a Sloan

Dektak II surface profiler. A surface-relief diffraction grating was then optically inscribed into the azopolymer film using the apparatus outlined in figure 3.1. Light from a Verdi-V5 diode-pumped laser with a wavelength of 532 nm and output power of 4 W was passed through a spatial filter and collimated to ~4.8 cm in diameter, yielding a plane wave writing beam with an irradiance of ~221 $mW \cdot cm^{-2}$. A $\lambda/4$ plate was subsequently used to create circularly polarized light, with the size of the beam being regulated to a diameter of ~1 cm using a variable iris. The beam was then incident on a rotating sample mount, which was adjusted so that half of the beam was incident on the mirror, and the other half was incident on the sample directly. The mirror and sample had an angular separation of 90°.

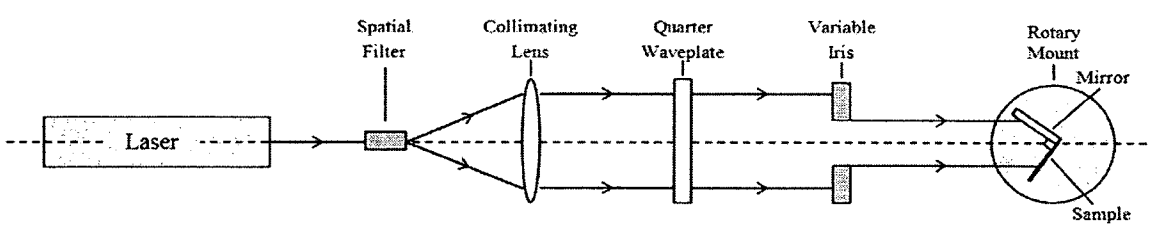

Figure 3.1. Overview of grating inscription apparatus.

The portion of the beam striking the mirror was reflected back onto the sample, interfering with the direct beam [1]. Due to the photo-sensitivity of the azopolymer, this interference pattern was inscribed onto the thin film in the form of a surface-relief diffraction grating. The grating spacing, Λ, was dependent upon both the wavelength of the laser light, λ, and angle of incidence, θ, as defined in figure 3.2, while the grating depth was dependent upon both the writing beam irradiance and exposure time.

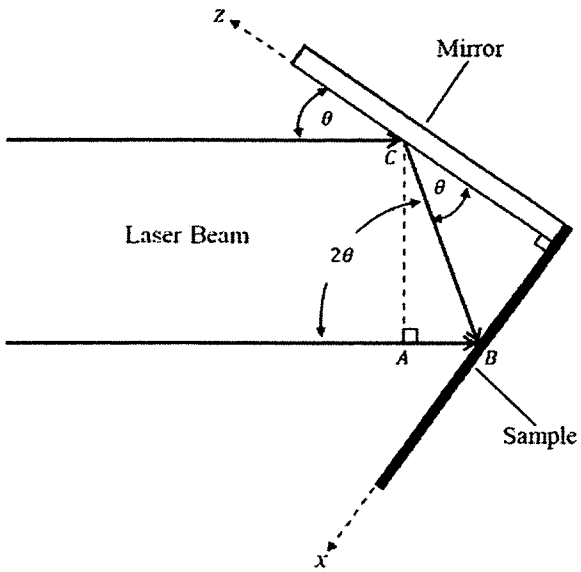

Figure 3.2. Overview of rotating sample mount.

The equation governing the grating spacing can be derived using figure 3.2. In order to have constructive interference, the net path difference between the two beam halves, $CB - AB$, must equal some integer of wavelength, $m\lambda$, plus the phase change due to the mirror reflection, $\lambda/2$. This relationship is highlighted by equation 3.1.

$$CB - AB = \lambda\left(m + \frac{1}{2}\right) \tag{3.1}$$

Using basic trigonometry, the expressions $CB = x/\sin\theta$ and $AB = CB\cos 2\theta$ were obtained, and substituted into equation 3.1, yielding the relation for constructive interference pattern maxima in terms of the wavelength of the laser light, λ, and angle of incidence, θ, as given by equation 3.2.

$$x = \frac{\lambda}{2\sin\theta}\left(m + \frac{1}{2}\right) \tag{3.2}$$

Therefore the distance between any two consecutive maxima, also known as the grating spacing, Λ, is given by equation 3.3.

$$\Lambda = \frac{\lambda}{2\sin\theta} \tag{3.3}$$

3.1.2 Grating Verification and Considerations

Diffraction gratings written using the above technique could be optically verified using the apparatus shown in figure 3.3. A low-power Helium-Neon laser, with a wavelength of 632.8 nm, passed through a $\lambda/4$ plate and a semi-transparent mirror, before being incident upon the grating sample. The semi-transparent mirror was positioned at a slight incline in order to reflect the diffracted orders above the sample and onto a viewing screen.

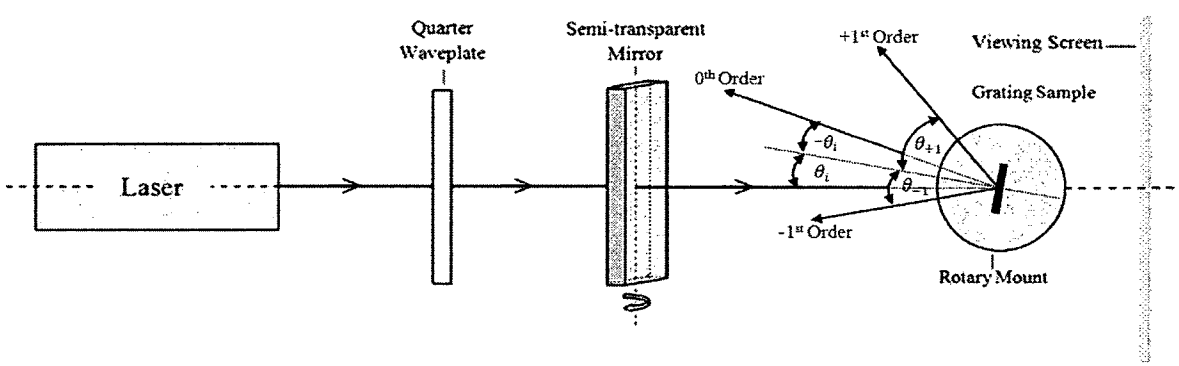

Figure 3.3. Overview of grating spacing verification apparatus.

The sample was originally mounted at normal incidence, with its 0th order position highlighted on the viewing screen. It was then rotated CW until the -1st order illuminated the original 0th order position on the viewing screen. At this position the -1st order angle of diffraction, θ_{-1}, was equal to the negative angle of incidence, $-\theta_i$. When $\theta_m = -\theta_i$, the grating equation (2.31) yields equation 3.4, and thus the grating spacing can be found.

$$\Lambda = \frac{\lambda}{2\sin\theta_m} \tag{3.4}$$

This procedure was then repeated for CCW rotation with the +1st order, and the grating spacing was determined to be the average of the two. Predicted grating spacings proved to be in very close agreement with optical measurements. A grating written with spacing, $\Lambda = 640$ nm, yielded small discrepancies of $\Lambda = 640.8 \pm 0.8$ nm. Gratings with spacings less than ~400 nm, could not be measured using this technique due to the limitations of both the wavelength ($\lambda = 632.8$ nm) and angle of incidence (θ_i). In such cases, an atomic force microscope (AFM) was used to measure spacings.

Both grating spacings and depths were measured using an AFM. Atomic force microscope (AFM) grating spacing measurements, while not considered as accurate as those measured by optical means, were nonetheless in close agreement with those expected. Figure 3.4 illustrates an AFM image of a single grating with spacing, $\Lambda \approx 640$ nm in both (a) 2-D and (b) 3-D. For a grating of spacing, $\Lambda \approx 640$ nm, it was found that an exposure time of ~70 secs yielded a grating depth of ~50 nm.

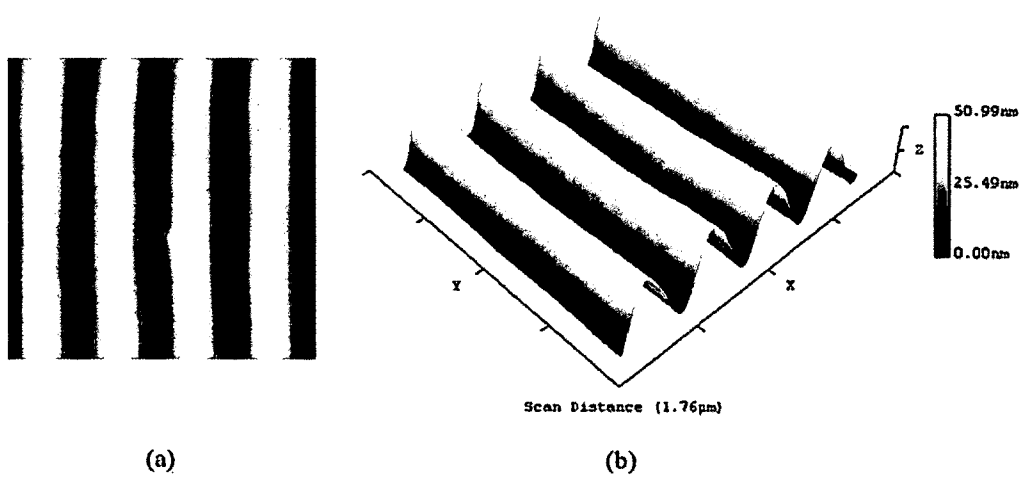

Figure 3.4. Single grating ($\Lambda \approx 640$ nm) in (a) 2-D and (b) 3-D.

Crossed gratings were fabricated by first writing a single grating, and then rotating the sample 90° in order to write a second (crossed) grating on top of the first grating. The spacings of both gratings were kept constant, however the exposure time of the second grating was such that it yielded $\pm 1^{st}$ order diffraction intensities comparable to those of the first grating. Generally, this corresponded to an exposure time of $\sim 1/3$ of that used to write the first of the two crossed gratings. Exposure times beyond $\sim 1/3$ resulted in grating degradation. Figure 3.5 illustrates an AFM image of a crossed grating with spacing, $\Lambda_{TM} = \Lambda_{TE} \approx 640$ nm in both (a) 2-D and (b) 3-D.

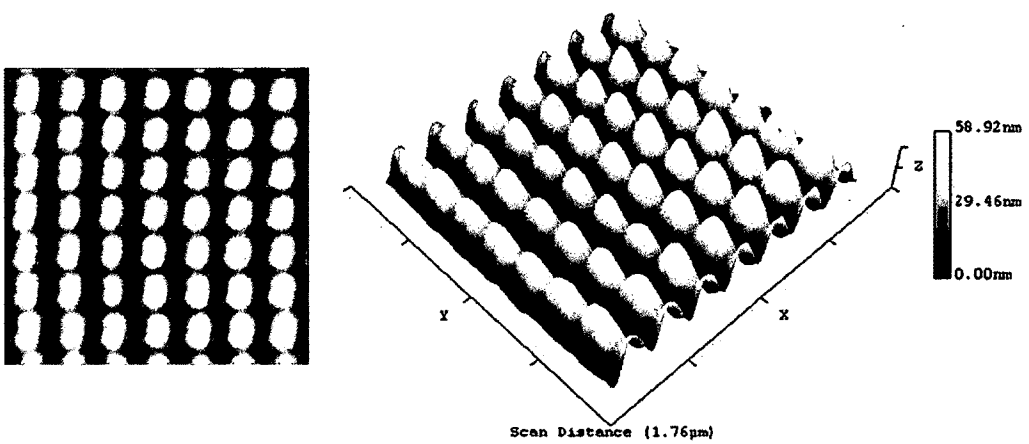

(a) (b)

Figure 3.5. Crossed grating ($\Lambda_{TM} = \Lambda_{TE} \approx 640$ nm) in (a) 2-D and (b) 3-D.

Parallel gratings were fabricated by writing a grating of spacing, Λ_2, on top of another grating of spacing, Λ_1. The grating with the larger spacing was written first, i.e. $\Lambda_1 > \Lambda_2$. Again, the exposure time of the second grating was such that it yielded $\pm 1^{st}$ order diffraction intensities comparable to those of the first grating. Generally, this corresponded to an exposure time of $\sim 1/2$ of that used to write the first of the two parallel gratings. Exposure times beyond $\sim 1/2$ resulted in grating degradation. After

the first grating was written, the test sample was slightly raised via the sample mount adjusting knob in order to vertically offset the two gratings. This made it possible to optically measure one grating spacing at a time. Figure 3.6 illustrates an AFM image of a parallel grating with spacing, $\Lambda_1 \approx 280$ nm and $\Lambda_2 \approx 240$ nm in both (a) 2-D and (b) 3-D. This grating was written using an Argon laser at $\lambda = 458$ nm.

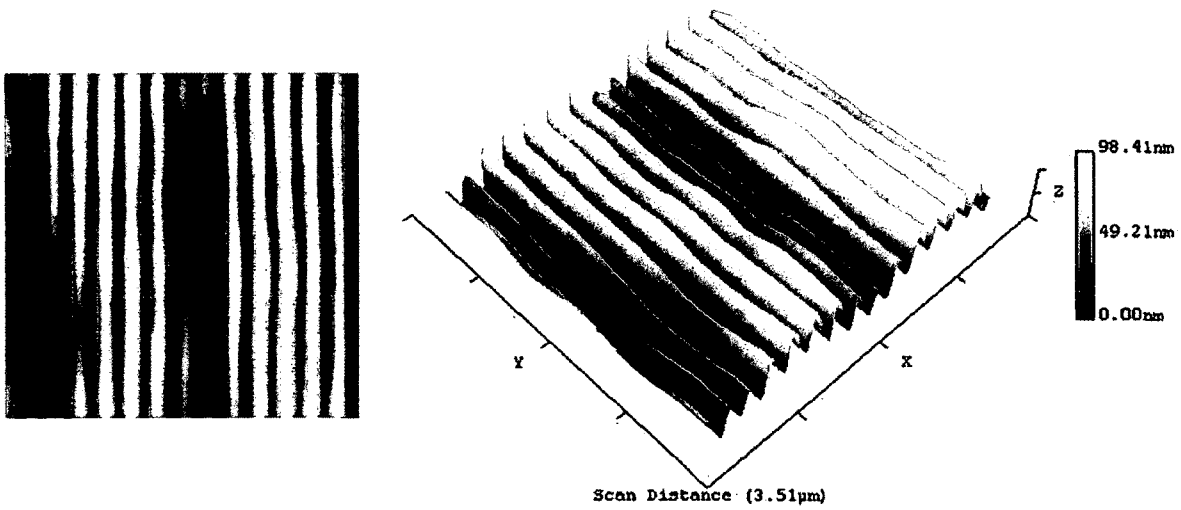

(a) (b)

Figure 3.6. Parallel grating ($\Lambda_1 \approx 280$ nm, $\Lambda_2 \approx 240$ nm) in (a) 2-D and (b) 3-D.

In the case of parallel gratings, two grating vectors are present and the grating equation can be modified as given by equation 3.5:

$$k_{light} = k \sin\theta_i \pm m_1 K_1 \pm m_2 K_2 \tag{3.5}$$

where m_1 and m_2 are the diffracted orders (limited to $\pm 1^{st}$) for grating vectors K_1 and K_2, respectively. The surface profile $s(x)$ shown in figure 3.6 is given by equation 3.6:

$$s(x) = d_1 \sin(K_1 x) + d_2 \sin(K_2 x + \varphi_2) \tag{3.6}$$

where x is the spatial coordinate, d_1 and d_2 are the amplitudes of the two harmonic components, and φ_2 is their relative phase [4].

3.1.3 Dielectric-Metal Interface

Once the desired gratings were inscribed onto the azopolymer, an ~100 nm thin layer of Ag was sputter coated onto the sample using a BAL-TEC SCD050 sputter coater. The layer thickness was controlled by adjusting the sputtering time, and made thick enough such that it was completely opaque to the majority of incident light being reflected. Since gold (Au) absorbs strongly below the wavelength of $\lambda = 600$ nm, it was found better to use a metal such as Ag or aluminum (Al) to generate SPs [5]. This thin metal layer assumed the shape of the grating, thus serving as both the metal portion of the interface, as well as a reflective diffraction grating. Figure 3.7 illustrates an AFM image of the single grating shown in figure 3.4, sputter coated with an ~100 nm thin layer of ag in both (a) 2-D and (b) 3-D.

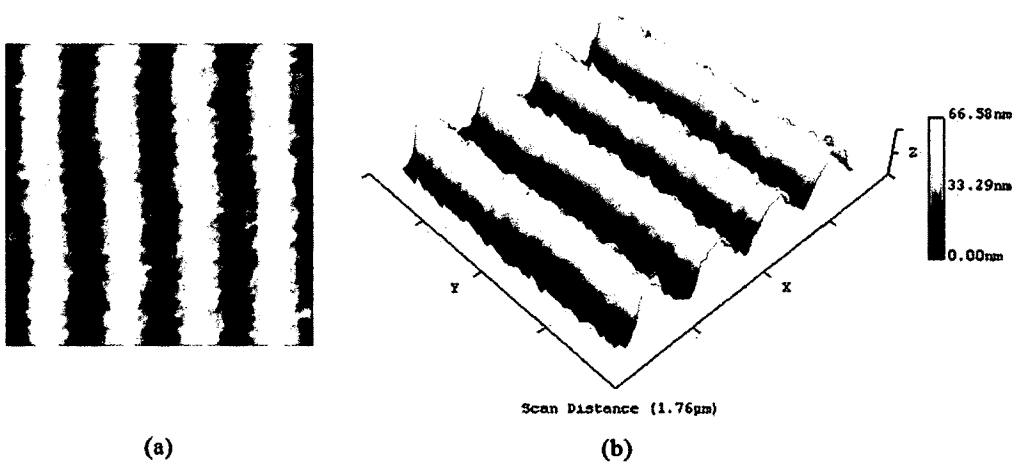

Figure 3.7. Single grating ($\Lambda \approx 640$ nm) sputtered with Ag in (a) 2-D and (b) 3-D.

Once the Ag had been sputter coated, it was time to complete the interface and deposit the dielectric. It was determined that it would be beneficial to first examine SPs in their purest form at an air-Ag interface, and thus during initial analysis no dielectric deposit was necessary. In this case the air served as the dielectric, and the completed test sample architecture was as illustrated in figure 3.8.

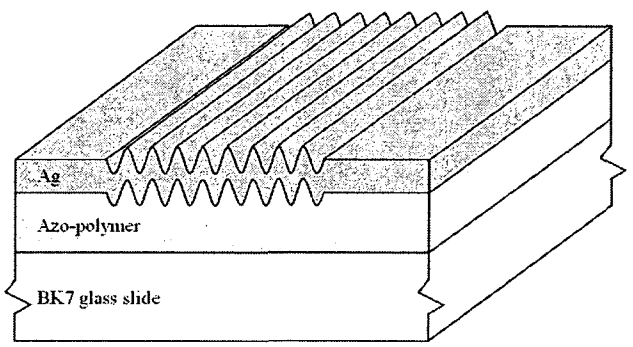

Figure 3.8. Architecture of an air-Ag test sample.

Following the air-Ag analysis, test samples were designed and fabricated with a thin film dielectric deposited upon the Ag. In order to avoid coupling effects in the dielectric film, thin layers ($\leq$ 180 nm) were used. This analysis closely resembled what could be expected when dealing with OSCs. Based upon availability, good adhesiveness, and demonstrated success in optical applications [6], polyvinyl alcohol (PVA) was chosen as the thin film dielectric. Using distilled water as the solvent, a clear, viscous solution was made. Depending on the desired thickness of the thin film, mix ratios were varied from 3 to 5% weight/weight. Once the PVA was completely dissolved, the solution was passed through a 0.45 μm nylon syringe filter. A thin film layer of the solution was then spin-coated onto the Ag grating, and subsequently baked at 90°C for 1 hour to remove

any remaining water. The architecture of the PVA-Ag sample was as illustrated in figure 3.9.

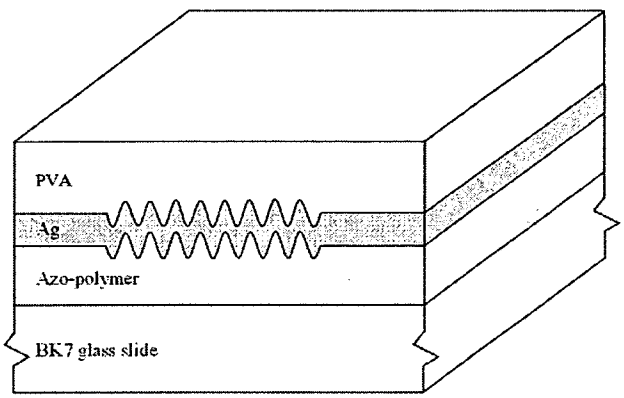

Figure 3.9. Architecture of a PVA-Ag test sample.

3.2 Test Sample Analysis

3.2.1 Test Sample Analysis Apparatus

Once the test samples were fabricated, they were placed on an analyzer as illustrated in figure 3.10. Light from a spectrometer was passed through a mechanical chopper and circularly polarized using a $\lambda/4$ plate. It was then collimated and reflected off of a concave mirror and through a polarizer, before being incident upon the test sample, which was located on a computer-controlled rotary mount. Light reflected from the test sample was directed to a second mirror, before finally being reflected into a photo detector. The signal from the test sample was amplified using a lock-in amplifier and recorded on a computer. This allowed for spectral scans at fixed angles of incidence.

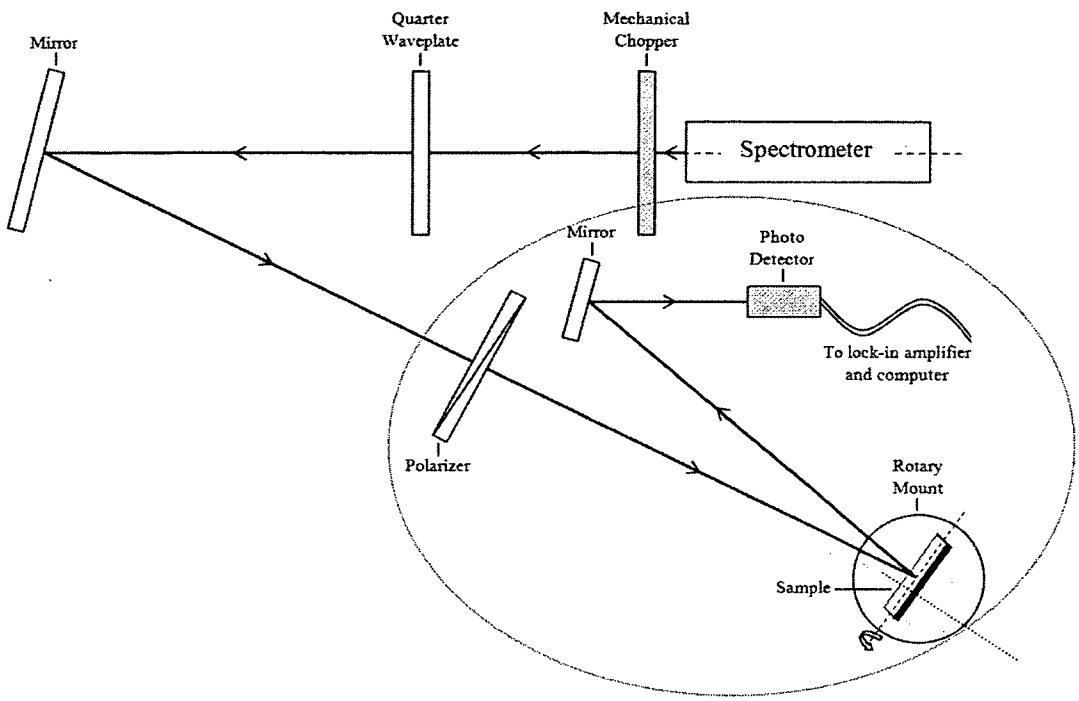

Figure 3.10. Overview of test sample analytical set-up.

The test sample was slightly tilted such that its reflected light near normal incidence would bypass above the polarizer. Figure 3.11 illustrates a side view of the circled stage of figure 3.10. Notice the slight tilt of the test sample. This tilting had no effect on the plane of incidence and sample analysis for TM and TE polarized light, except in the case of crossed gratings. In such cases for 'TE' analysis, the test sample had to be physically turned 90° in order to get a valid 'TE' response.

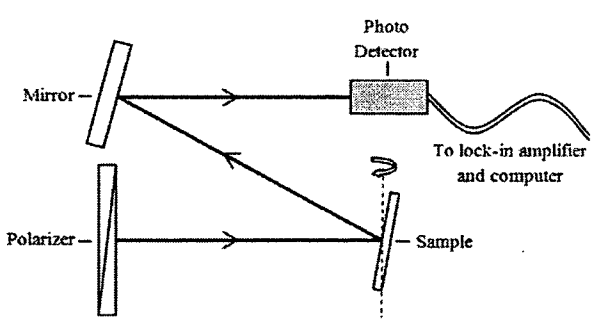

Figure 3.11. Side view of test sample analytical set-up for circled stage.

3.2.2 Test Sample Irradiance Response

The $\pm 1^{st}$ orders of diffraction are responsible for the SP excitation. When these orders skim the surface of the metal, they oscillate in resonance with the surface electron density fluctuations. The excitation of SPs causes light to be re-radiated in all directions. The interference of this re-radiated light with the 0th order accounts for the response. Recall that for gratings oriented with the grating vector parallel to the plane of incidence (along the x-axis), only TM polarized incident light will excite SPs. Thus, when measuring the relative (TM/TE) irradiance of a test sample, one can expect SP excitation to yield sharp increases in the transmitted response due to the constructive interference of the two, and sharp decreases in the reflected response due to the destructive interference of the two. This destructive interference is due to the characteristic 180° phase shift seen in reflected waves incident from a low side index. These responses are illustrated in figure 3.12.

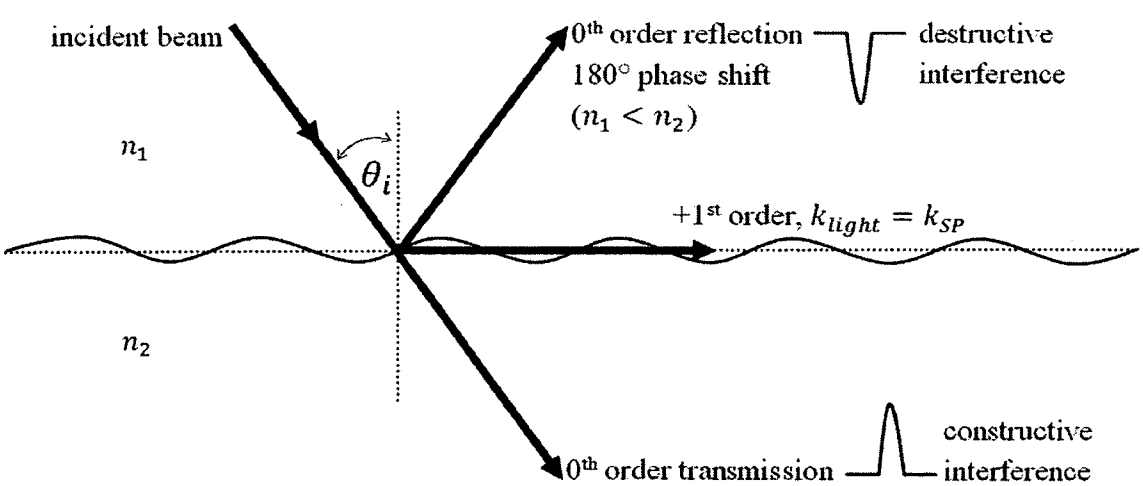

Figure 3.12. Relative irradiance response due to SP excitation.

3.3 Analysis of an Air-Silver (Ag) Interface

3.3.1 Single Grating Air-Silver (Ag) Interface

First, a single grating air-Ag interface was analyzed. For an air-Ag (dielectric-metal) interface at 650 nm, $n_d \approx 1$, and $\tilde{\varepsilon}'_{r,m} \approx -19.552$ [7], and thus the SP excitation wavelength equation (2.54) took the form $\lambda_{SP} \approx (1.027 \mp \sin\theta_i)\Lambda$. Initially, grating spacings were varied at normal incidence in order to verify their agreement with the above approximation, as well as to visualize their behaviour. Figure 3.13 illustrates a plot of the relative (TM/TE) reflected irradiance at normal incidence for varied grating spacings at an air-ag interface.

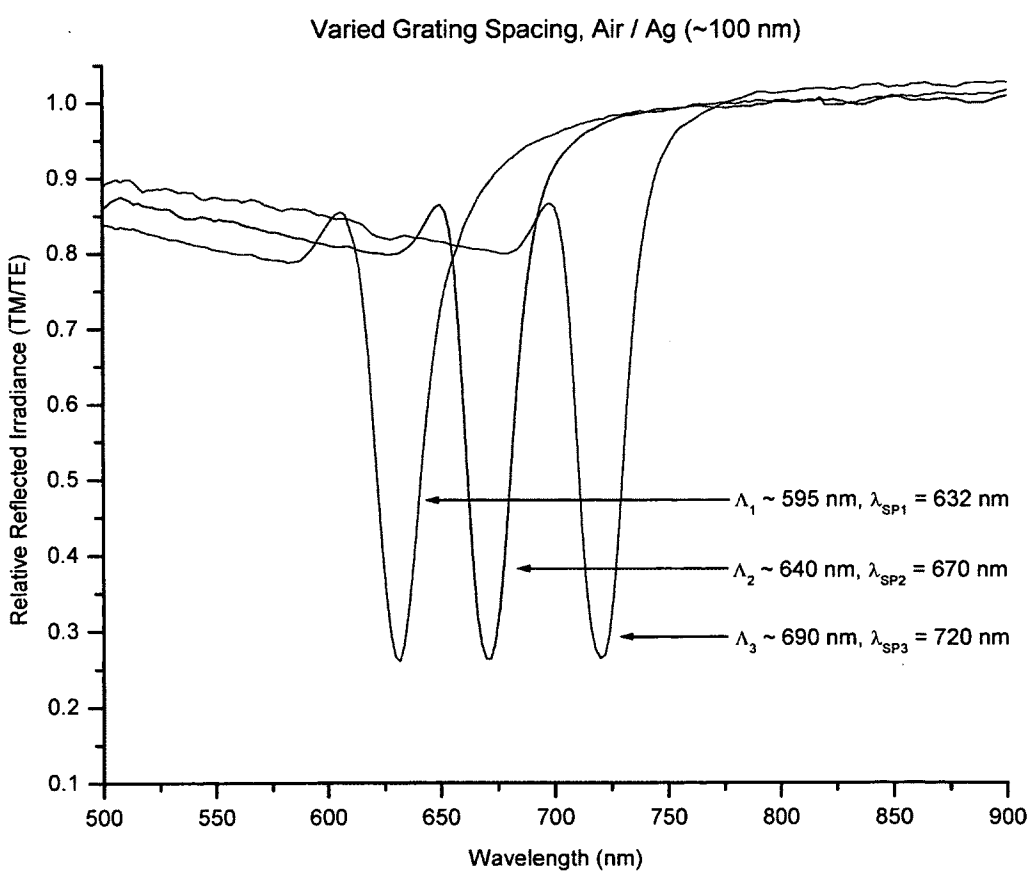

Figure 3.13. SPs at an air-Ag interface at $\theta_i = 0$ for varied grating spacing.

One can see from figure 3.13 that as predicted, the SP excitation wavelength is directly proportional to the grating spacing, $\lambda_{SP} \propto \Lambda$. Also, as the wavelength, λ, approaches the grating spacing, Λ, more and more of the light is diffracted from the 0th order, and thus the relative response is seen as slightly, yet constantly, decreasing. As λ becomes larger than Λ no light is diffracted, and the relative response begins its return to unity, until the SP excitation condition is met ($\lambda = \lambda_{SP}$) and the sharp troughs appear (destructive interference). As λ becomes larger than λ_{SP}, the relative response continues its return to unity (~ 1). At normal incidence, only one value of λ_{SP} exists which satisfies the $k_{light} = k_{SP}$ condition.

As seen in table 3.1, theoretical approximations at normal incidence were in good agreement with experimental results shown in figure 3.13. Discrepancies can be attributed to approximations which ignore non-flat surfaces, frequency dependence and losses.

Table 3.1. Theoretical and experimental comparison of λ_{SP} at $\theta_i = 0$.

Grating Spacing, Λ (nm)	**Theoretical λ_{SP} (nm)**	**Experimental λ_{SP} (nm)**
595	611	632
640	657	670
690	709	720

Once control of λ_{SP} at normal incidence was demonstrated, the effect of varying the grating depth was explored. For a fixed grating spacing at normal incidence, grating depths were varied by adjusting the exposure time during grating inscription. Figure 3.14 illustrates a plot of the relative (TM/TE) reflected irradiance at normal incidence for varied grating depths at an air-Ag interface for a fixed grating spacing of $\Lambda \approx 635$ nm.

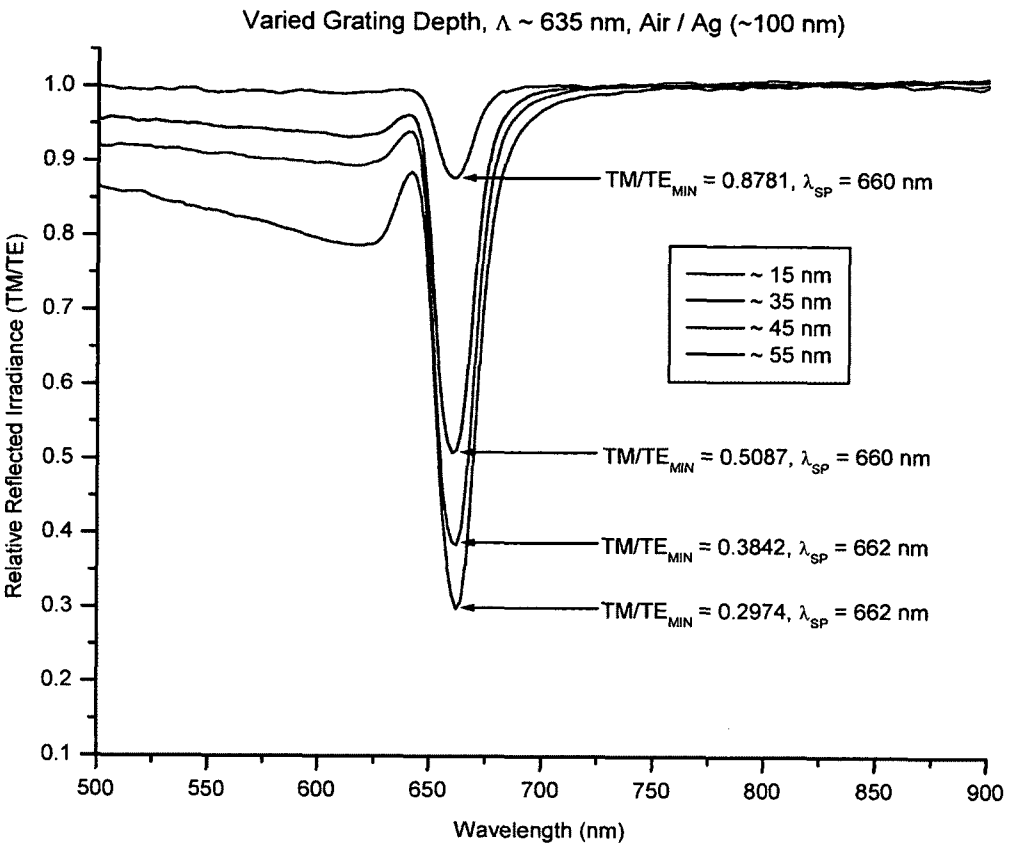

Figure 3.14. SPs at an air-Ag interface at $\theta_i = 0$ for varied grating depths ($\Lambda \approx 635$ nm).

While varying the grating depths had no effect on λ_{SP}, it did have a significant effect on the relative (TM/TE) reflected irradiance. As seen in figure 3.14, as the grating depth increases from ~15 to ~55 nm, the corresponding TM/TE_{MIN} decreases. This was expected since deeper gratings generally correspond to greater diffraction efficiency. The smallest possible TM/TE_{MIN} was desired, since it corresponded to an increase in SP excitation (i.e. more destructive interference → more re-radiated light → more SP excitation). It was found that grating depths beyond ~55 nm yielded characteristic band gaps in the SP resonance [5]. For the sake of simplicity, SP band gaps were avoided by only using gratings with depths less than ~55 nm.

Once the effects of grating spacing and depths were examined, trials involving varying angles of incidence were carried out. Figure 3.15 illustrates a nine-panel plot of the relative (TM/TE) reflected irradiance of a single grating air-Ag interface for varied angles of incidence (8° to -8°) with a fixed grating spacing of $\Lambda \approx 640$ nm and depth of ~55 nm. Here the normal incidence $\lambda_{SP} = 672$ nm.

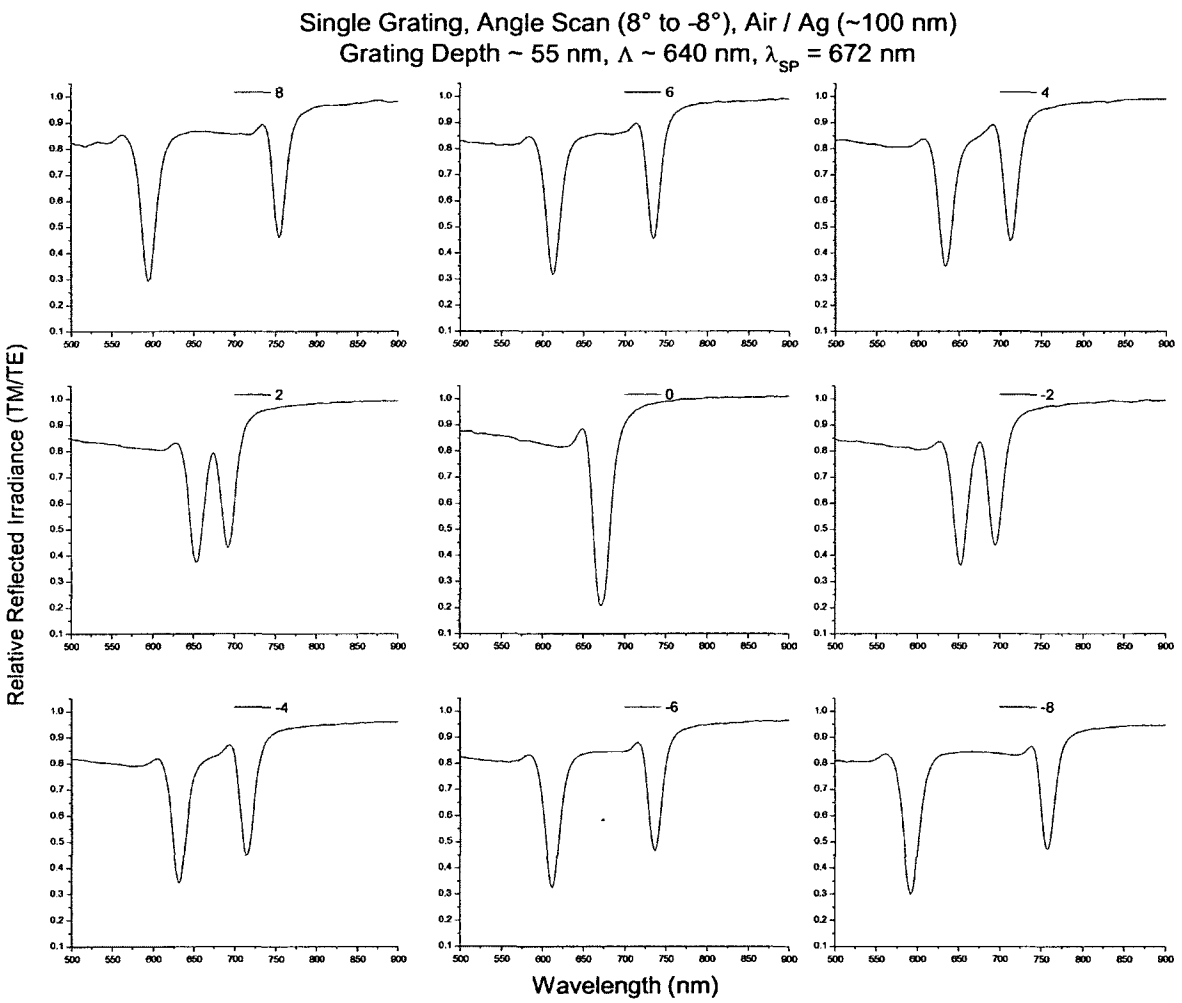

Figure 3.15. SPs at a single grating air-Ag interface for varied θ_i.

As seen in figure 3.15, as the angle of incidence was increased from zero, two values of λ_{SP} emerged which satisfied the $k_{light} = k_{SP}$ condition given by $\lambda_{SP} \approx$

$(1.027 \mp \sin\theta_i)\Lambda$. These values of λ_{SP} corresponded to the $\pm 1^{st}$ orders of diffraction, and were seen in the graphical results as a splitting of the SPs excited at normal incidence. Theoretical approximations were again in good agreement with experimental results. At $\theta_i = 8°$, theory predicted λ_{SP} values of 568 nm and 746 nm, whereas experimental results yielded λ_{SP} values of 594 nm and 778 nm.

Figure 3.16 illustrates an intensity plot of the relative (TM/TE) reflected irradiance of a single grating air-Ag interface for varied incident angles (10° to -10°) with a fixed grating spacing of $\Lambda \approx 640$ nm and depth of ~55 nm. This is the same test sample as was analyzed in figure 3.15.

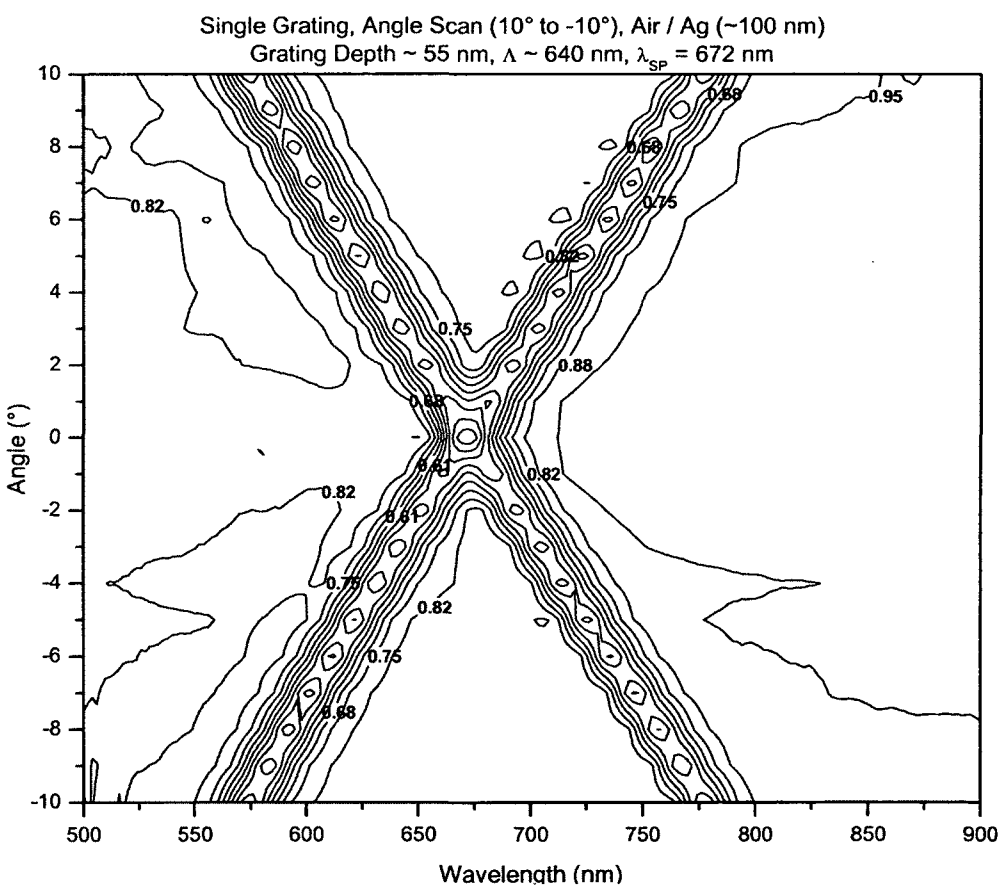

Figure 3.16. SPs at a single grating air-Ag interface for varied θ_i contour.

Figure 3.17 illustrates the same intensity plot shown in figure 3.16, but with colour. One can see from figure 3.17 that generally more SPs were excited (deeper troughs) for $\lambda < 672$ nm compared to $\lambda > 672$ nm. It is believed that this may be due to the wavelength-dependency of the dielectric permittivity. Another possible cause may be a slightly blazed diffraction grating, creating asymmetrical diffraction throughout its orders.

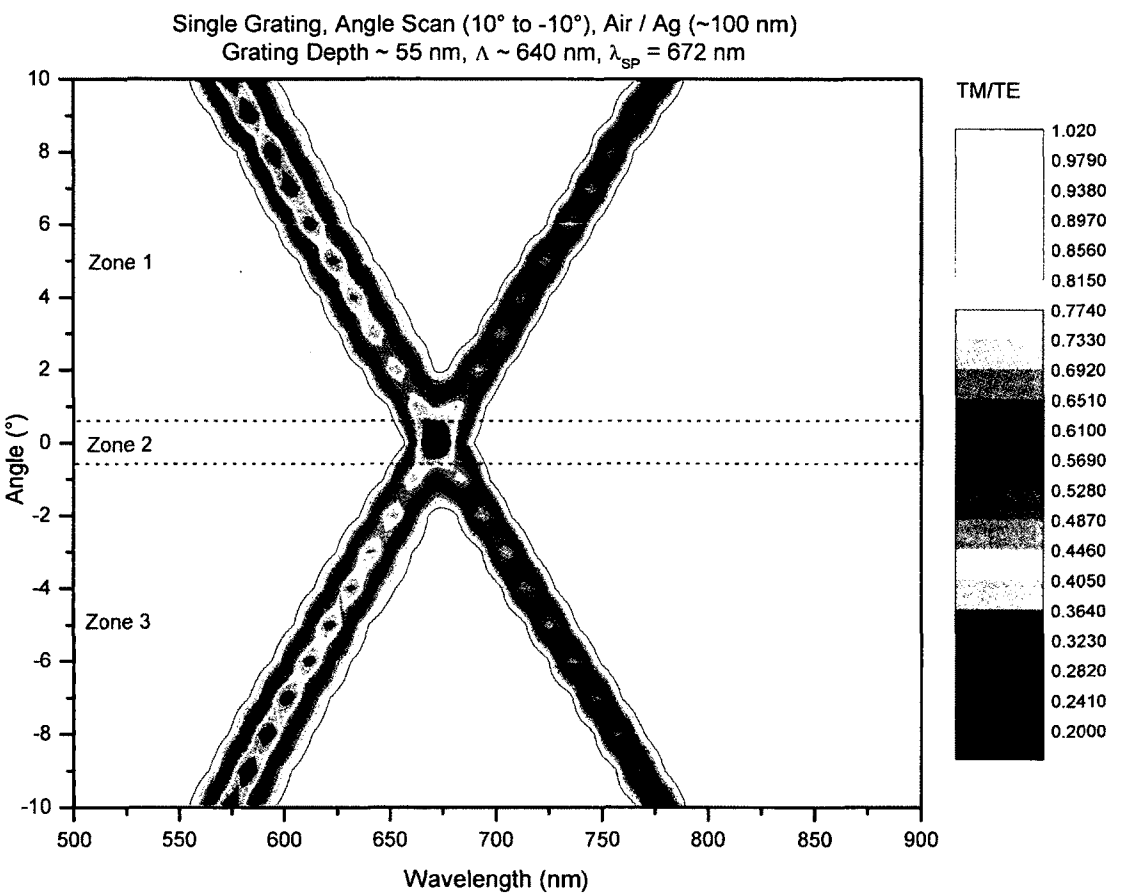

Figure 3.17. SPs at a single grating air-Ag interface for varied θ_i colour.

The zones highlighted in figure 3.17 correspond to the cases illustrated in figure 3.18. Recall that the order diffracted to the right of the 0th order is the $+1^{st}$ order, whereas that diffracted to the left is the -1st order. Also, as the wavelength of light increases, so

too does its angle of diffraction (relative to the 0th order). Thus, looking at the grating geometry of zone 1, the $+1^{st}$ order will couple to the SPs at a shorter wavelength than the -1st order ($\lambda_{SP,+1} < \lambda_{SP,-1}$), yielding two different values of λ_{SP}. As the angle of incidence further increases, the orders sweep in a CW-direction, yielding a decreasing $\lambda_{SP,+1}$, but an increasing $\lambda_{SP,-1}$. In zone 2 ($\theta_i = 0$), $\lambda_{SP,+1} = \lambda_{SP,-1}$ yields a standing wave, represented by a single value of λ_{SP}. This accounts for the most favourable TM/TE_{MIN} seen at $\theta_i = 0$, since it has overlapping contributions from both the $\pm 1^{st}$ orders. Looking at the grating geometry of zone 3, the -1st order will couple to the SPs at a shorter wavelength than the $+1^{st}$ order ($\lambda_{SP,-1} < \lambda_{SP,+1}$), yielding two different values of λ_{SP}. This is the reverse of what was occurring in zone 1. As the angle of incidence further decreases, the orders sweep in a CCW-direction, yielding a decreasing $\lambda_{SP,-1}$, but an increasing $\lambda_{SP,+1}$.

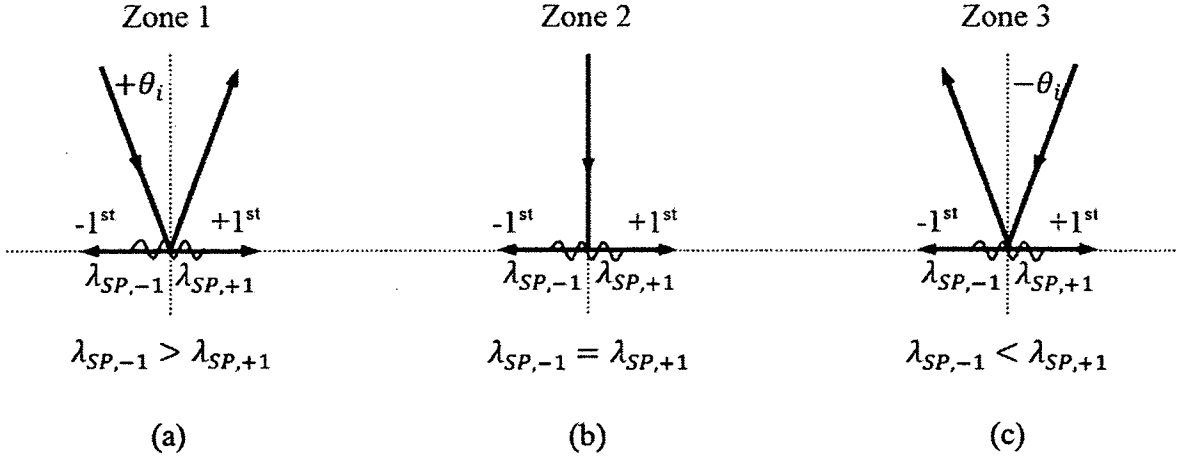

Figure 3.18. Explanation of zones (a) 1, (b) 2 and (c) 3 as highlighted in figure 3.17.

3.3.2 Crossed Grating Air-Silver (Ag) Interface

Following the analysis of single gratings, SPs at a crossed grating air-Ag interface were examined. The spacings of both gratings were equal. By limiting the exposure time of the second grating to $\sim 1/3$ that of the first grating, comparable relative reflected irradiance responses were obtained. Recall that in order for SPs to be excited, the incident light must have an $\vec{E}$-field component along the grating vector. For gratings oriented with the grating vector parallel to the plane of incidence, this condition is satisfied via TM polarized incident light only. However, using a crossed grating scheme, there exists grating vectors both parallel and perpendicular to the plane of incidence, and thus both TM and TE polarized incident light are capable of exciting SPs. In fact using crossed gratings, any incident light polarization will generate SPs [8]. A crossed grating can be thought of as a single grating simply extended to include SP excitation in all polarizations.

Since SPs were excited in all polarizations, a relative (TM/TE) irradiance response would not illustrate the excitation of SPs. Thus, an irradiance response relative to a polynomial fit was taken. The destructive interference troughs (corresponding to SP excitation) of the irradiance response were removed and a polynomial fit was computed. This allowed a clear indication of SP excitation over all polarizations. The gratings were oriented such that the initial grating written at full exposure time would generate SPs with TM polarized incident light (TM active grating – grating vector parallel to the plane of incidence), whereas the second grating written at $\sim 1/3$ the exposure time would generate SPs with TE polarized incident light (TE active grating – grating vector

perpendicular to the plane of incidence). Results of the TM active grating will be provided first.

Figure 3.19 illustrates a nine-panel plot of the relative (TM/polynomial fit) reflected irradiance of a crossed grating air-Ag interface for varied incident angles (8° to -8°) with a fixed TM active grating spacing of $\Lambda \approx 640$ nm and depth of ~55 nm.

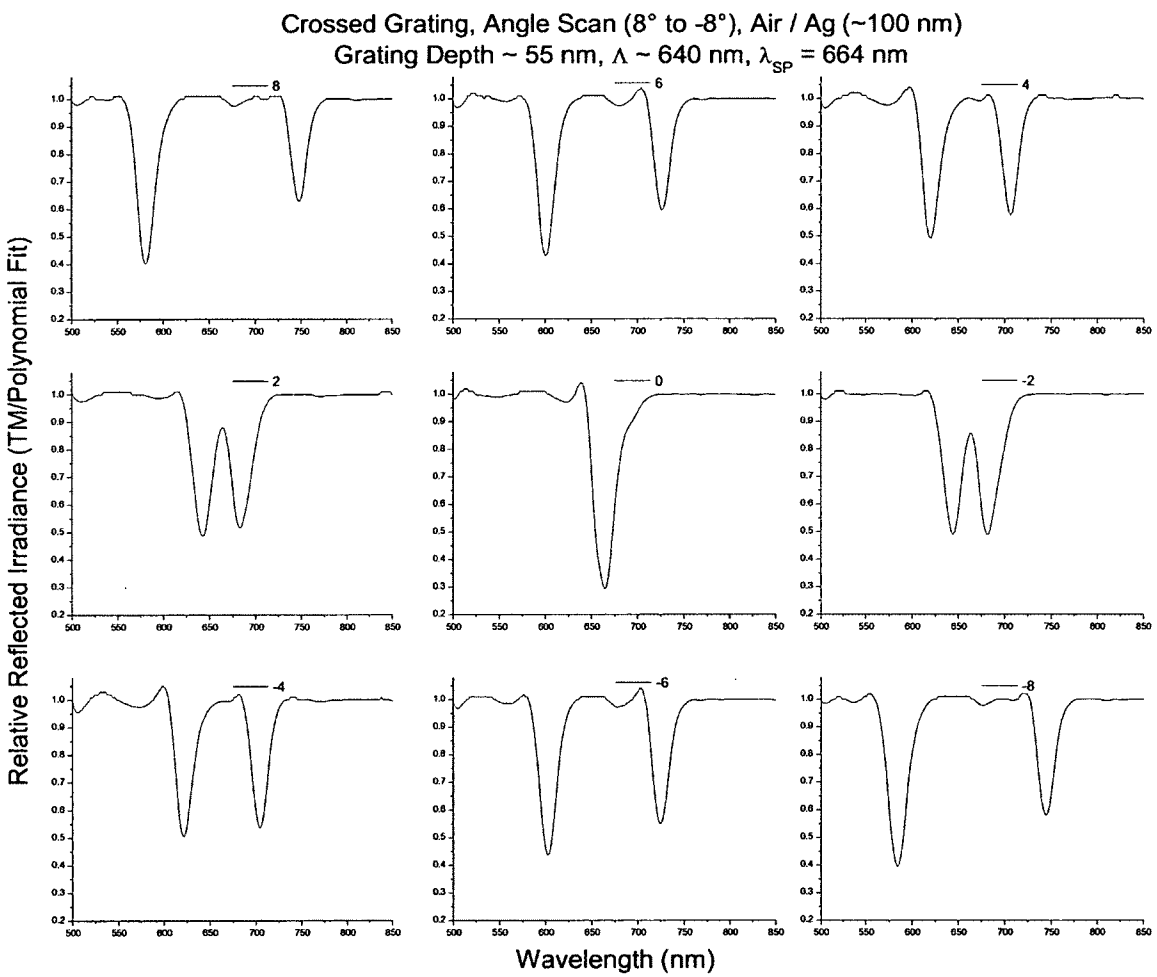

Figure 3.19. TM SPs at a crossed grating air-Ag interface for varied θ_i.

At normal incidence, one value of λ_{SP} ($\lambda_{SP} = 664$ nm) excited SPs. As the angle of incidence was increased from zero, two values of λ_{SP} emerged which satisfied the

$k_{light} = k_{SP}$ condition. These values of λ_{SP} corresponded to the $\pm 1^{st}$ orders of diffraction, and were seen in the graphical results as a splitting of the SPs excited at normal incidence.

Figure 3.20 illustrates an intensity plot of the relative (TM/polynomial fit) reflected irradiance of a crossed grating air-Ag interface for varied incident angles (10° to -10°) with a fixed TM active grating spacing of $\Lambda \approx 640$ nm and depth of ~55 nm. This is the same test sample as was analyzed in figure 3.19.

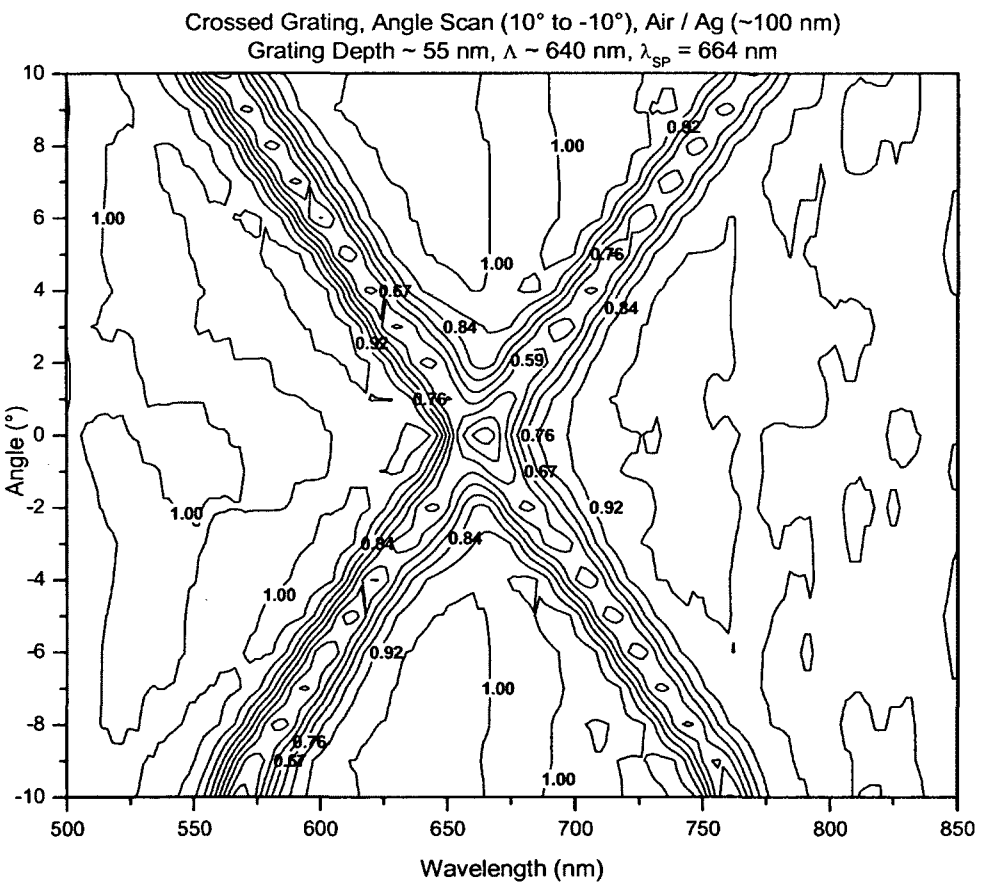

Figure 3.20. TM SPs at a crossed grating air-Ag interface for varied θ_i contour.

Figure 3.21 illustrates the same intensity plot shown in figure 3.20, but with colour. Again, one can see that generally more SPs were excited for $\lambda < 664$ nm compared to $\lambda > 664$ nm.

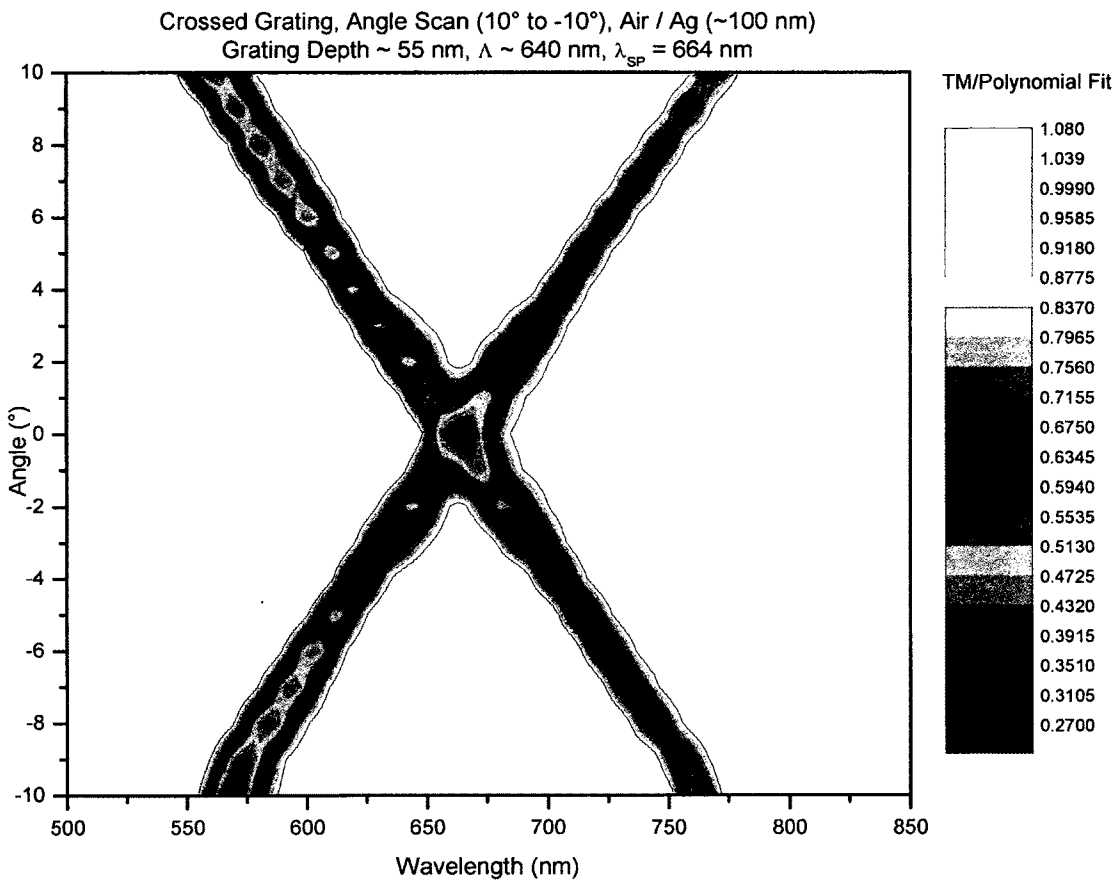

Figure 3.21. TM SPs at a crossed grating air-Ag interface for varied θ_i colour.

In order to examine SPs excited via the 'TE' active grating, the test sample had to be physically turned 90°. This was necessary due to the slight inclination given to the test sample in order for its reflection to bypass the polarizer. Figure 3.22 illustrates a nine-panel plot of the relative (TE/polynomial fit) reflected irradiance of a crossed grating air-Ag interface for varied incident angles (8° to -8°) with a fixed TE active grating spacing of $\Lambda \approx 640$ nm and depth of ~25 nm. At normal incidence, $\lambda_{SP} = 662$ nm. This grating was written at $\sim 1/3$ the exposure time of the TM active grating, accounting for the grating depth of ~25 nm.

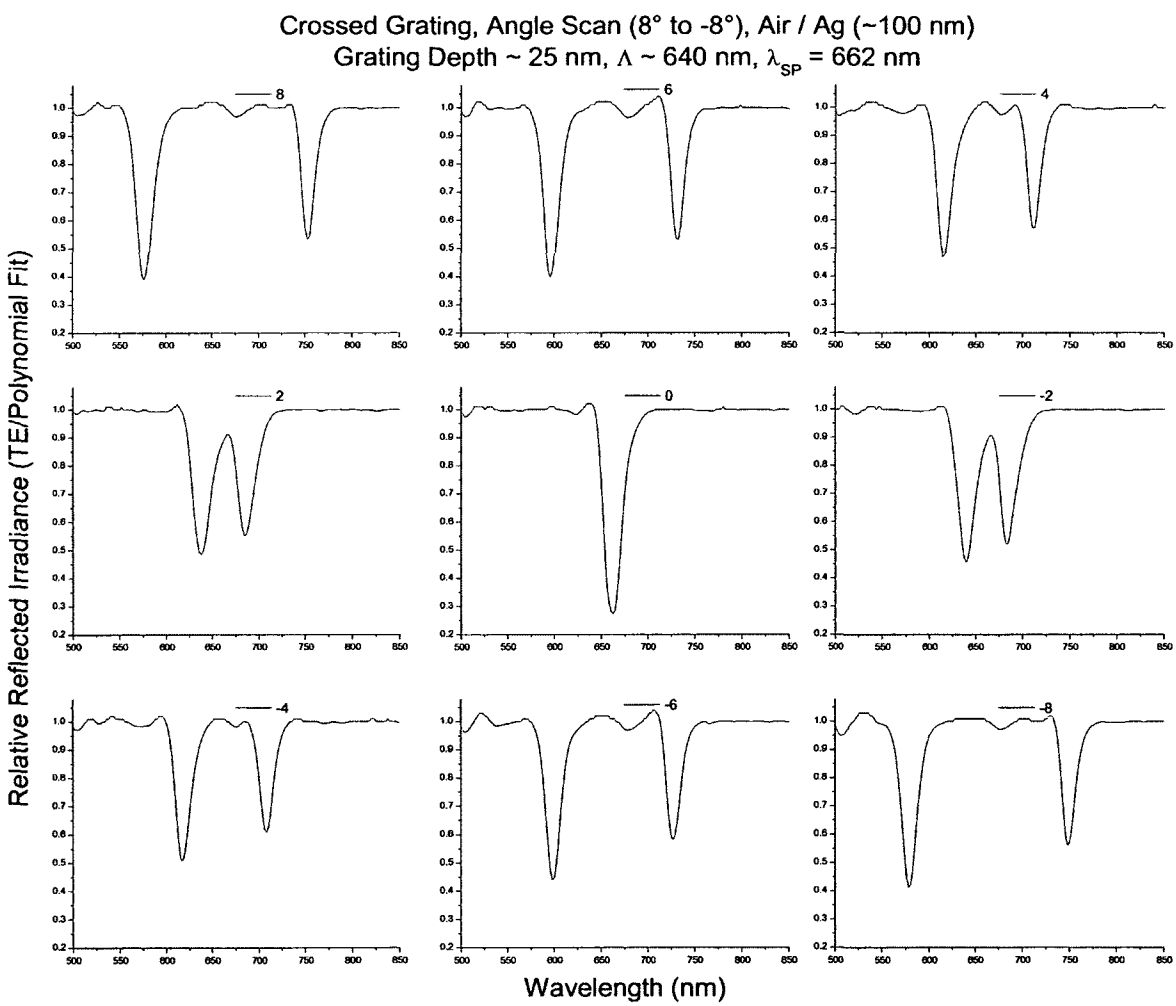

Figure 3.22. TE SPs at a crossed grating air-Ag interface for varied θ_i.

Figure 3.23 illustrates an intensity plot of the relative (TE/polynomial fit) reflected irradiance of a crossed grating air-Ag interface for varied incident angles (10° to -10°) with a fixed TE active grating spacing of $\Lambda \approx 640$ nm and depth of ~25 nm. This is the same test sample as was analyzed in figure 3.22.

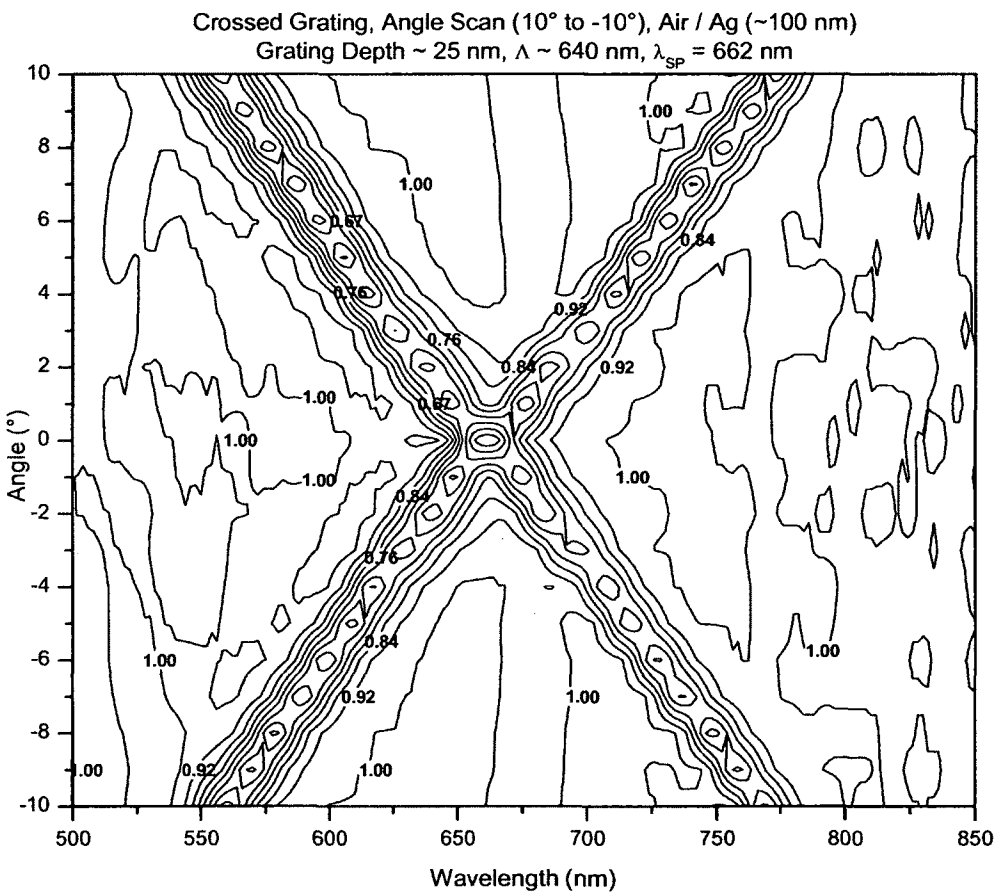

Figure 3.23. TE SPs at a crossed grating air-Ag interface for varied θ_i contour.

Figure 3.24 illustrates the same intensity plot shown in figure 3.23, but with colour. Given that the TE active grating depth was less than half that of the TM active grating, the former was slightly weaker in the excitation of SPs.

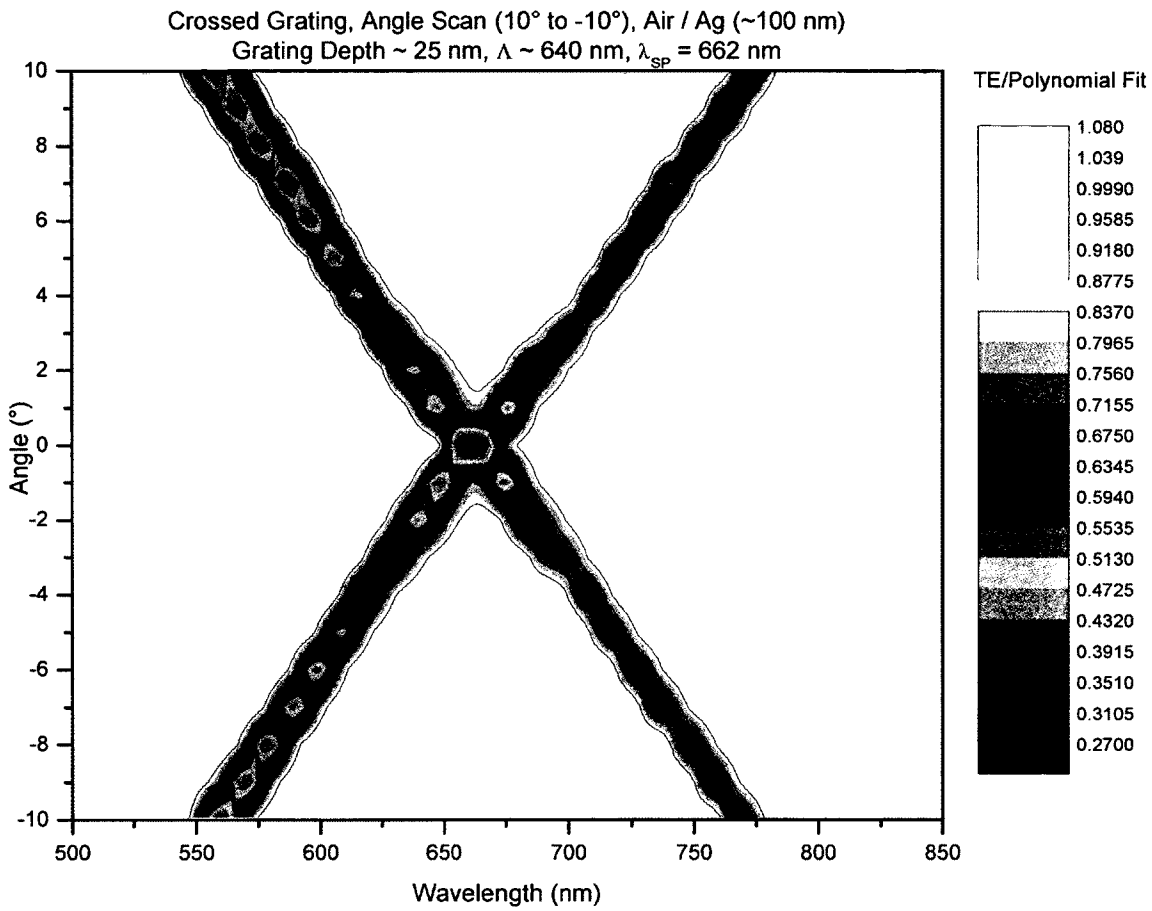

Figure 3.24. TE SPs at a crossed grating air-Ag interface for varied θ_i colour.

3.3.3 Parallel Grating Air-Silver (Ag) Interface

Following the analysis of crossed gratings, SPs at a parallel grating air-Ag interface were examined. The larger grating was first written, followed by the smaller grating, i.e. $\Lambda_1 > \Lambda_2$. By limiting the exposure time of the second grating to $\sim 1/2$ that of the first grating, comparable SP irradiance responses were obtained. Figure 3.25

illustrates a nine-panel plot of the relative (TM/TE) reflected irradiance of a parallel grating air-Ag interface for varied incident angles (8° to -8°) with fixed grating spacings of $\Lambda_1 \approx 700$ nm and $\Lambda_2 \approx 600$ nm. The depth of each grating, Λ_1 and Λ_2, was ~55 nm and ~35 nm respectively. Given that the first grating (Λ_1) was deeper than the second (Λ_2), the former was slightly stronger in the excitation of SPs.

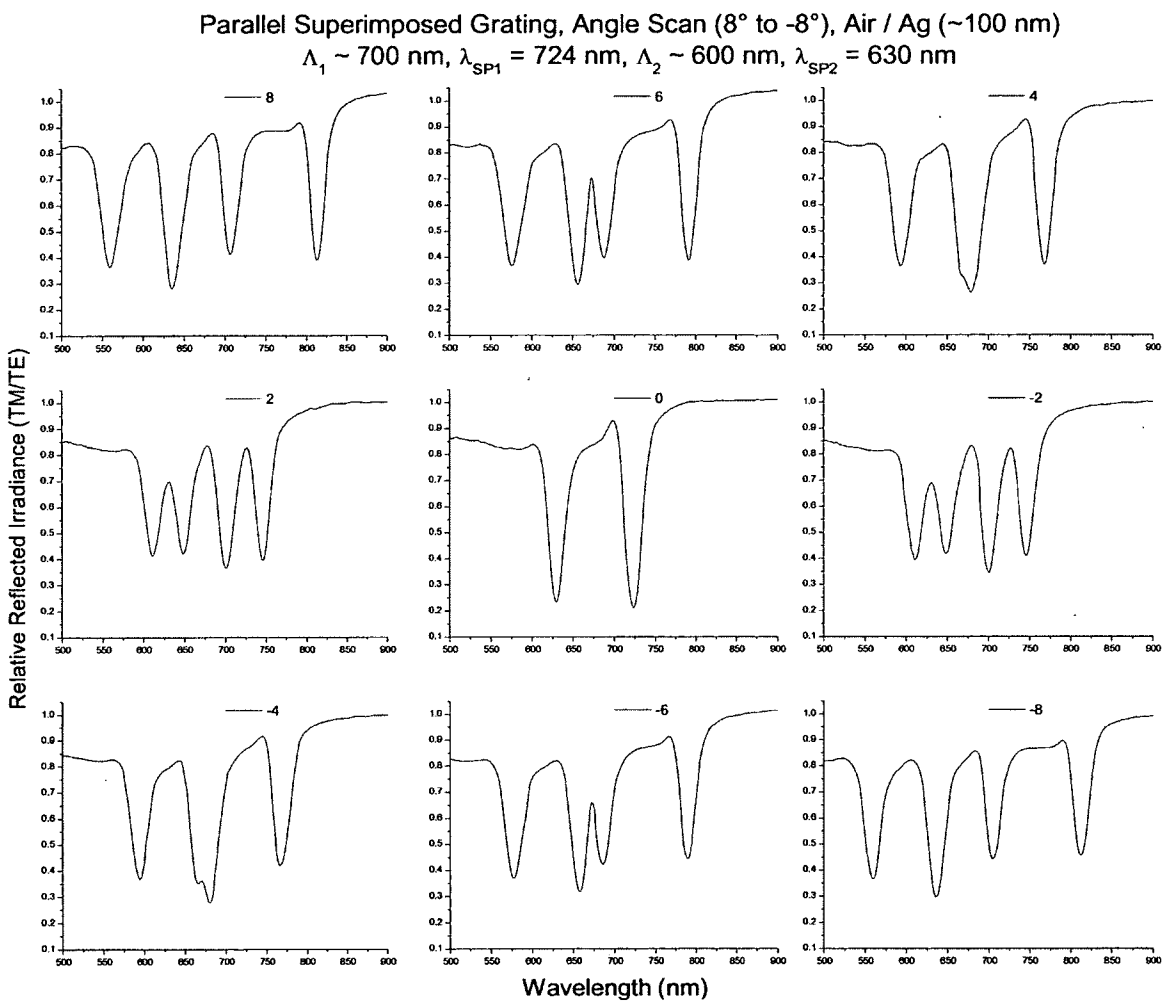

Figure 3.25. SPs at a parallel grating air-Ag interface for varied θ_i.

Recall that for parallel gratings their exists two grating vectors, K_1 (Λ_1) and K_2 (Λ_2), and as such the effective grating vector – limited to $\pm 1^{st}$ orders – can be any

combination of $\pm m_1 K_1 \pm m_2 K_2$. As seen in figure 3.25, at normal incidence, two values of λ_{SP} ($\lambda_{SP} = 630$ nm and 724 nm) excited SPs (representing two standing waves). These values corresponded to the $\pm 1^{st}$ orders of each grating separately, i.e. $m_1 = \pm 1$, $m_2 = 0$ ($K_{\pm 1,0}$), and $m_1 = 0$, $m_2 = \pm 1$ ($K_{0,\pm 1}$). As the incident angle was increased from zero, four values of λ_{SP} emerged which satisfied the $k_{light} = k_{SP}$ condition. These values of λ_{SP}, seen in the graphical results as a splitting of the SPs excited at normal incidence, again corresponded to the $\pm 1^{st}$ orders of each grating separately, i.e. $m_1 = \pm 1$, $m_2 = 0$ ($K_{\pm 1,0}$), and $m_1 = 0$, $m_2 = \pm 1$ ($K_{0,\pm 1}$). Therefore, within the spectral range of 500 – 900 nm, parallel gratings of spacings, $\Lambda_1 \approx 700$ nm and $\Lambda_2 \approx 600$ nm, can be treated as two separate gratings, and the SP excitation wavelength approximation holds true, i.e. $\lambda_{SP} \approx (1.027 \mp \sin\theta_i)\Lambda$. In order to see SPs excited by the grating vector combination $m_1 = 1$, $m_2 = 1$ ($K_{1,1}$), or $m_1 = -1$, $m_2 = -1$ ($K_{-1,-1}$), an ultraviolet (UV) spectral scan would be necessary. Similarly, in order to see SPs excited by the grating vector combination $m_1 = 1$, $m_2 = -1$ ($K_{1,-1}$), or $m_1 = -1$, $m_2 = 1$ ($K_{-1,1}$), an infrared (IR) spectral scan would be necessary. In order to predict the SP excitation wavelengths in the UV and IR bands, another SP excitation wavelength approximation would have to be derived accounting for the combined grating vector effects.

Figure 3.26 illustrates an intensity plot of the relative (TM/TE) reflected irradiance of a parallel grating air-Ag interface for varied incident angles (10° to -10°) with fixed grating spacings of $\Lambda_1 \approx 700$ nm and $\Lambda_2 \approx 600$ nm. The depth of each grating, Λ_1 and Λ_2, was ~55 nm and ~35 nm respectively. This is the same test sample as was analyzed in figure 3.25.

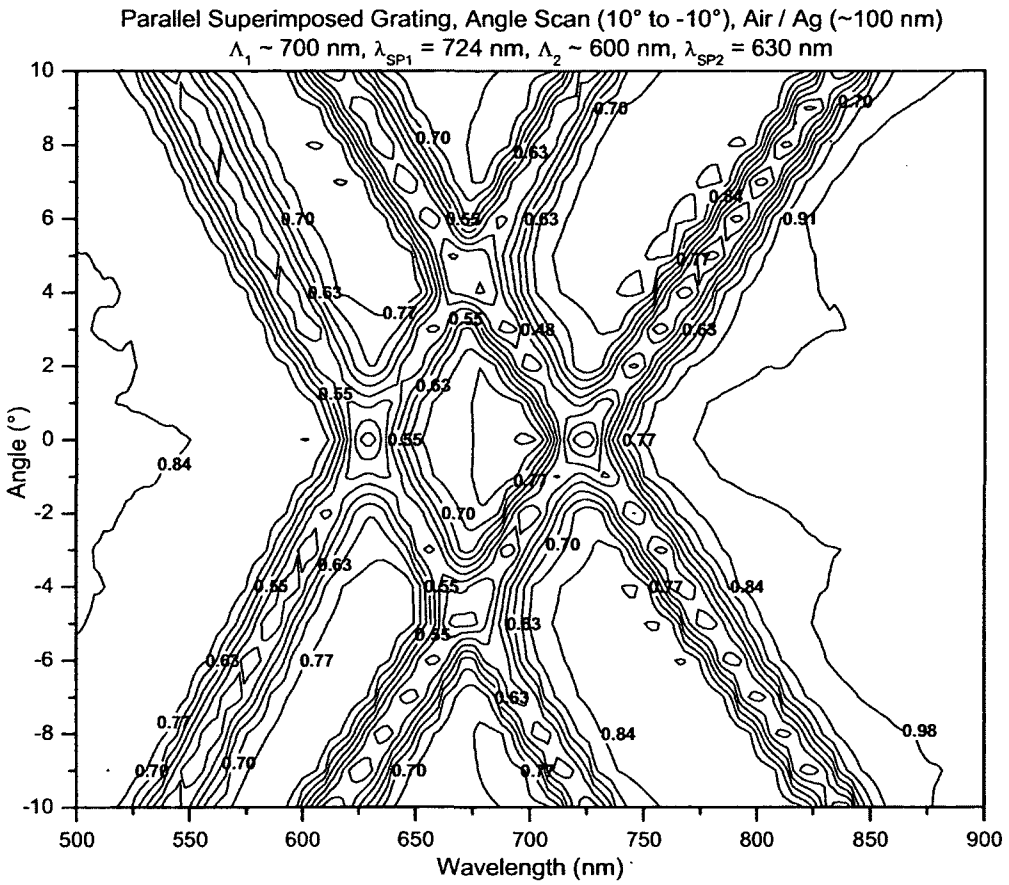

Figure 3.26. SPs at a parallel grating air-Ag interface for varied θ_i contour.

Figure 3.27 illustrates the same intensity plot shown in figure 3.26, but with colour. One can see that the larger grating Λ_1 is slightly stronger than the smaller grating (Λ_2). At normal incidence, only two values of λ_{SP} ($\lambda_{SP,(0,\pm1)}$ and $\lambda_{SP,(\pm1,0)}$) will excite SPs, whereas at oblique incidence, four values of λ_{SP} ($\lambda_{SP,(0,1)}$, $\lambda_{SP,(1,0)}$, $\lambda_{SP,(0,-1)}$, and $\lambda_{SP,(-1,0)}$) will excite SPs.

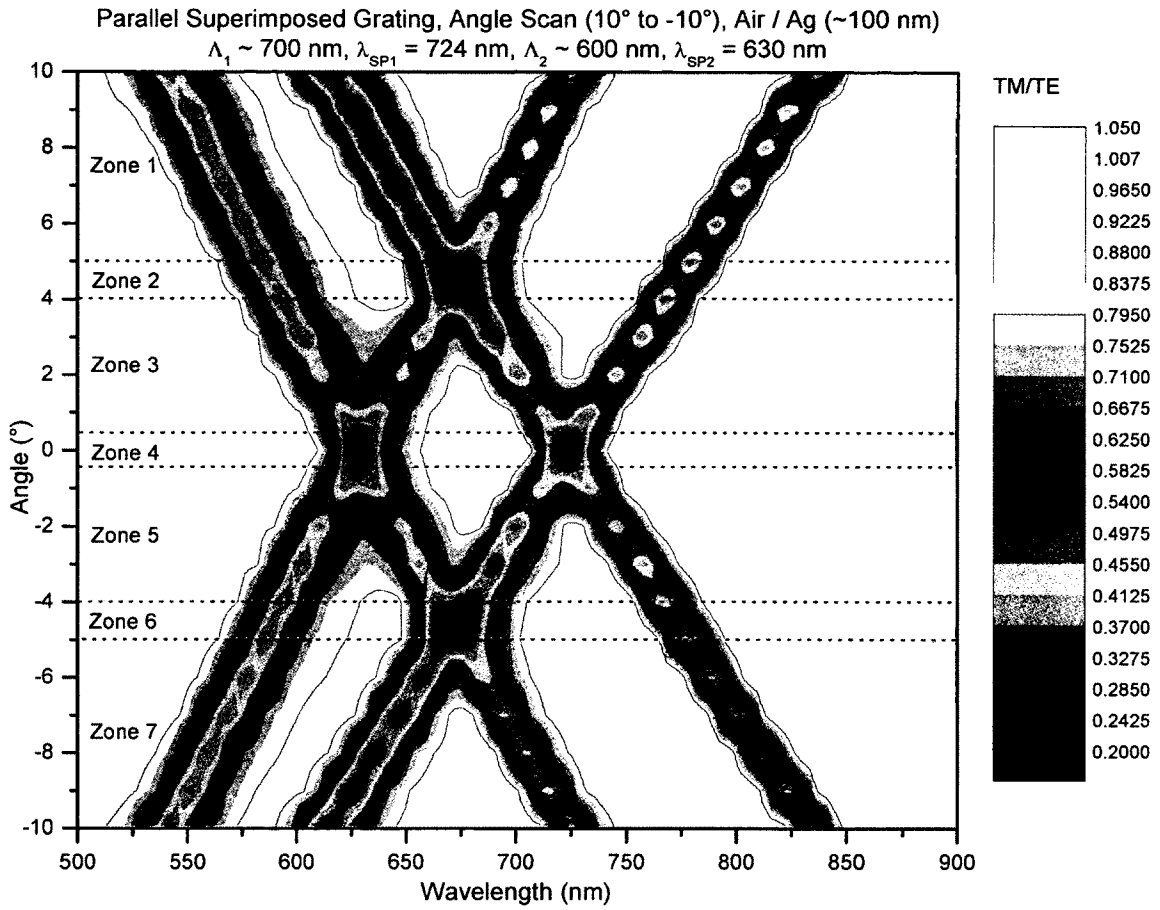

Figure 3.27. SPs at a parallel grating air-Ag interface for varied θ_i colour.

The zones highlighted in figure 3.27 can be visualized by looking at the parallel grating SP excitation plot as illustrated in figure 3.28 (recall that $\omega \propto \lambda^{-1}$). In zone 1 ($\theta_i > 5°$), $\lambda_{SP,(0,1)} < \lambda_{SP,(1,0)} < \lambda_{SP,(0,-1)} < \lambda_{SP,(-1,0)}$ yielding four different values of λ_{SP}. The +1st orders will excite SPs at a shorter λ (larger ω) than the -1st orders, i.e. $\lambda_{SP,(0,1)} < \lambda_{SP,(0,-1)}$ and $\lambda_{SP,(1,0)} < \lambda_{SP,(-1,0)}$. As the angle of incidence further increases, the orders sweep in a CW-direction, yielding decreasing $\lambda_{SP,(0,1)}$ and $\lambda_{SP,(1,0)}$, but increasing $\lambda_{SP,(0,-1)}$ and $\lambda_{SP,(-1,0)}$. This is the actual condition represented in figure 3.28. In zone 2 ($4° < \theta_i < 5°$), $\lambda_{SP,(0,1)} < \lambda_{SP,(1,0)} \approx \lambda_{SP,(0,-1)} < \lambda_{SP,(-1,0)}$ yielding

three values of λ_{SP}. This accounts for the favourable TM/TE$_{\text{MIN}}$ seen in the central trough, since it has overlapping contributions from both the $(m = 1, 0)$ and $(m = 0, -1)$ orders. Looking at figure 3.28 this makes sense, since the angle of incidence (and thus the $k \sin\theta_i$ term) has decreased compared to zone 1. In zone 3 ($0° < \theta_i < 4°$), $\lambda_{SP,(0,1)} < \lambda_{SP,(0,-1)} < \lambda_{SP,(1,0)} < \lambda_{SP,(-1,0)}$ yielding four different values of λ_{SP}. This is the same condition as in zone 1, except now $\lambda_{SP,(0,-1)} < \lambda_{SP,(1,0)}$. In zone 4 ($\theta_i = 0°$), $\lambda_{SP,(0,1)} = \lambda_{SP,(0,-1)} < \lambda_{SP,(1,0)} = \lambda_{SP,(-1,0)}$, yielding two different values of λ_{SP} (two standing waves). At normal incidence the $k \sin\theta_i$ term in figure 3.28 disappears. This accounts for the most favorable values of TM/TE$_{\text{MIN}}$ seen at $\theta_i = 0$, since they have overlapping contributions from both the $(m = 0, \pm 1)$ and $(m = \pm 1, 0)$ orders. Zone 5 ($-4° < \theta_i < 0°$), is the reverse of what was occurring in zone 3, $\lambda_{SP,(0,-1)} < \lambda_{SP,(0,1)} < \lambda_{SP,(-1,0)} < \lambda_{SP,(1,0)}$. The -1st orders will excite SPs at a shorter wavelength than the +1st orders (i.e. $\lambda_{SP,(0,-1)} < \lambda_{SP,(0,1)}$ and $\lambda_{SP,(-1,0)} < \lambda_{SP,(1,0)}$). As the angle of incidence further decreases, the orders sweep in a CCW-direction, yielding decreasing $\lambda_{SP,(0,-1)}$ and $\lambda_{SP,(-1,0)}$, but increasing $\lambda_{SP,(0,1)}$ and $\lambda_{SP,(1,0)}$. In zone 6 ($-5° < \theta_i < -4°$), $\lambda_{SP,(0,-1)} < \lambda_{SP,(-1,0)} \approx \lambda_{SP,(0,1)} < \lambda_{SP,(1,0)}$ yielding three values of λ_{SP}. This accounts for the favourable TM/TE$_{\text{MIN}}$ seen in the central trough, since it has overlapping contributions from both the $(m = -1, 0)$ and $(m = 0, 1)$ orders. In zone 7 ($\theta_i < -5°$), $\lambda_{SP,(0,-1)} < \lambda_{SP,(-1,0)} < \lambda_{SP,(0,1)} < \lambda_{SP,(1,0)}$ yielding four different values of λ_{SP}. This is the same condition as in zone 5, except now $\lambda_{SP,(-1,0)} < \lambda_{SP,(0,1)}$.

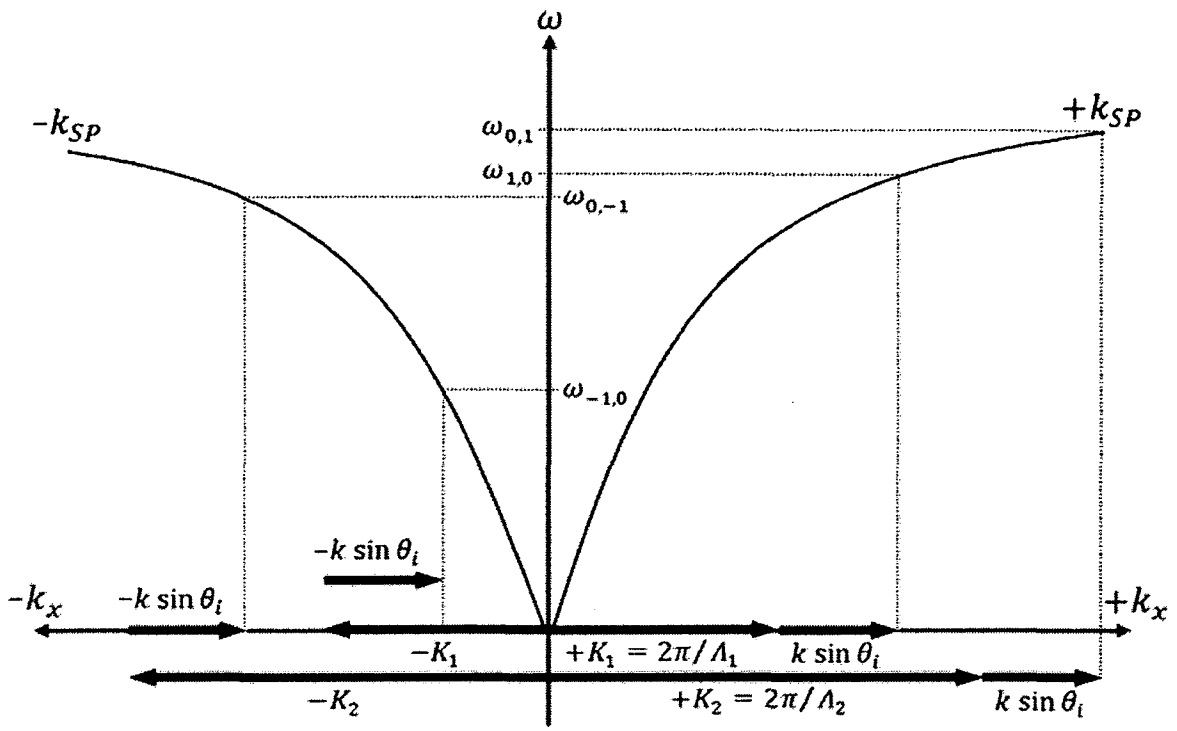

Figure 3.28. Parallel grating SP excitation plot.

3.4 Analysis of a Polyvinyl Alcohol (PVA)-Silver (Ag) Interface

3.4.1 Single Grating Polyvinyl Alcohol (PVA)-Silver (Ag) Interface

For the PVA-Ag interface analysis, at 650 nm, $n_d \approx 1.525$ [6], and $\tilde{\varepsilon}'_{r,m} \approx -19.552$ [7], and thus the SP excitation wavelength equation (2.54) took the form, $\lambda_{SP} \approx 1.525(1.065 \mp \sin\theta_i)\Lambda$. Initially, varied PVA thickness trials were carried out on a single grating in order to determine an optimal film thickness. It was necessary to vary the mix ratios from 3 to 5% in order to obtain the full range of film thicknesses. Varied film thicknesses were spin coated onto a cleaned BK7 glass slide and measured using the Dektak IIA surface profiler as illustrated in table 3.2.

Table 3.2. PVA thin film parameters.

Sloan Dektak IIA Surface Profiler	
Spin Coat RPM (% w/w mix ratio)	**Film Thickness (nm)**
3000 (5)	446 ± 11
1000 (4)	400 ± 15
1200 (4)	337 ± 14
1500 (4)	279 ± 8
3000 (4)	223 ± 6
1500 (3)	191 ± 10
1700 (3)	158 ± 8
3000 (3)	114 ± 6
5000 (3)	76 ± 5

Once the appropriate thickness parameters were determined, PVA thin films varying from ~75 to ~450 nm were spin coated onto the Ag gratings and subsequently analyzed. Figure 3.29 illustrates a nine-panel plot of the relative reflected irradiance (TM/TE) at normal incidence for varied film thicknesses (~75 to ~450 nm) at a single grating PVA-Ag interface with a fixed grating spacing of $\Lambda \approx 400$ nm and depth of ~55 nm.

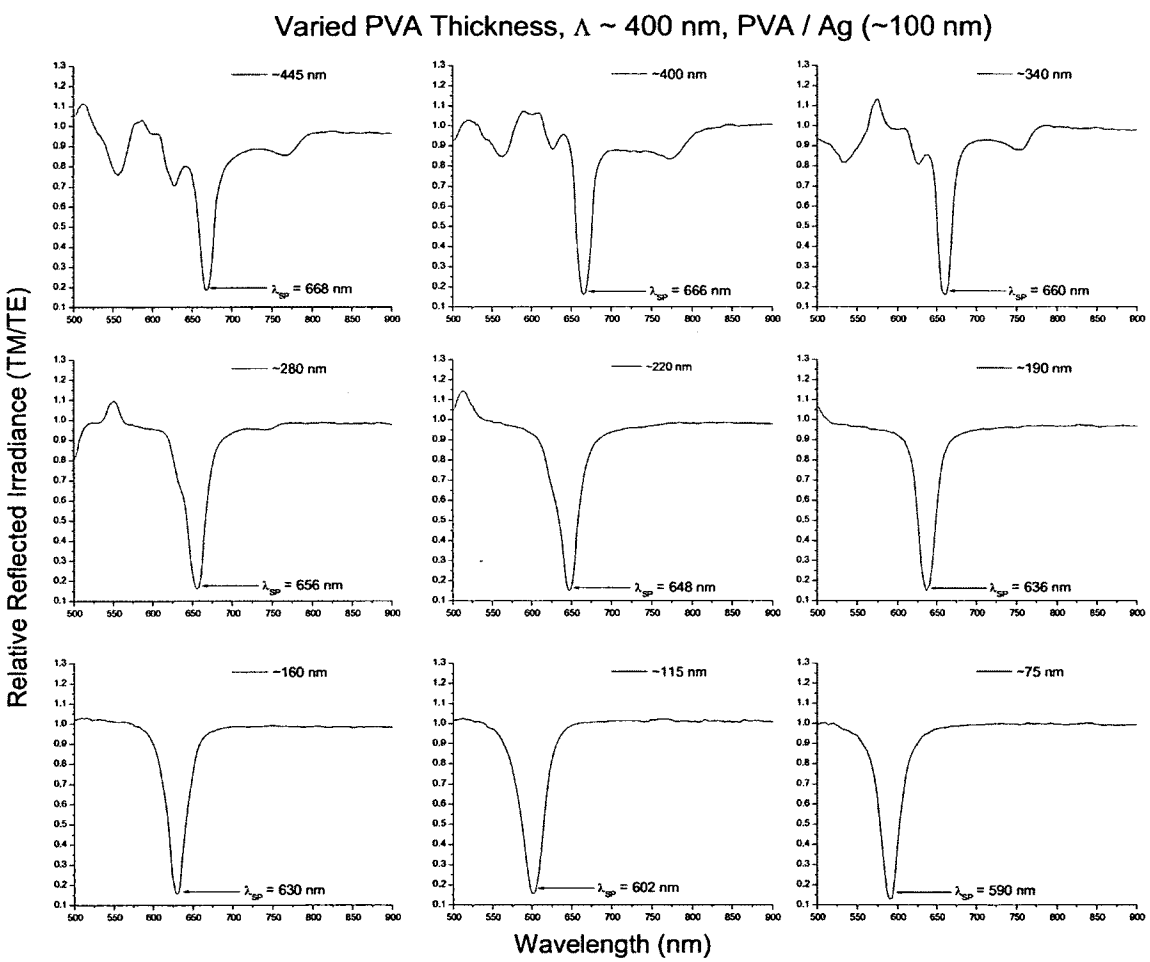

Figure 3.29. SPs at a PVA-Ag interface at $\theta_i = 0$ for varied film thicknesses.

Based on the SP excitation wavelength approximation at normal incidence, one would think that for a fixed grating spacing ($\Lambda \approx 400$ nm), λ_{SP} would remain constant.

However, as seen in figure 3.29, depending on the PVA thickness, this may not always be the case. Recall that SPs are evanescent waves which propagate along the interface and extend into each adjacent media. Typically, the decay length at which the $\vec{E}$-field falls to $1/e$ of its initial value into the dielectric, δ_d, is on the order of half the wavelength of incident light [9]. Thus, for film thicknesses below the $\vec{E}$-field decay length, the evanescent tail of the SP extends beyond the PVA thin film, and the effective refractive index of the dielectric used in the SP excitation wavelength approximation, becomes some combination of the refractive indexes of both air and PVA. This explains the changing λ_{SP} seen in figure 3.29 for varying PVA film thicknesses. One can see that at ~400 nm, λ_{SP} more or less stabilizes, indicating that the adjacent SP $\vec{E}$-field is mostly decayed. Figure 3.30 illustrates the SP $\vec{E}$-field decay length into the dielectric, δ_d.

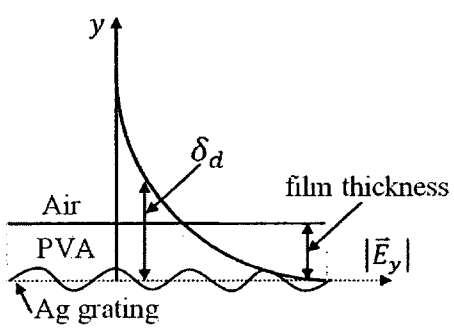

Figure 3.30. SP $\vec{E}$-field decay into the dielectric, δ_d.

As seen in figure 3.29, as PVA film thicknesses increased, non-SP related peaks and troughs became apparent in the irradiance response of the test sample. These peaks and troughs are credited to thin film coupling effects, and can become cumbersome when trying to highlight purely SP-related effects. These coupling effects, by themselves, have actually been proven to enhance photocurrent generation in OSCs [10], however in order

to keep the analysis evident and purely SP-based, it was decided that a PVA film thickness of ~180 nm would be used for further analysis. This would allow for a nice portion of the adjacent, decaying SP $\vec{E}$-field to be encompassed within the PVA thin film.

3.4.2 Crossed Grating Polyvinyl Alcohol (PVA)-Silver (Ag) Interface

Following the analysis of single gratings, SPs at a crossed grating PVA-ag interface were examined. The spacings of both gratings were equal. The gratings were oriented such that the initial grating written at full exposure time would generate SPs with TM polarized incident light, whereas the second grating written at $\sim 1/3$ the exposure time would generate SPs with TE polarized incident light.

Figure 3.31 illustrates a nine-panel plot of the relative (TM/polynomial fit) reflected irradiance of a crossed grating PVA-Ag interface for varied incidence angles (16° to -16°) with a fixed TM active grating spacing of $\Lambda \approx 430$ nm and depth of ~55 nm. At normal incidence, $\lambda_{SP} = 670$ nm.

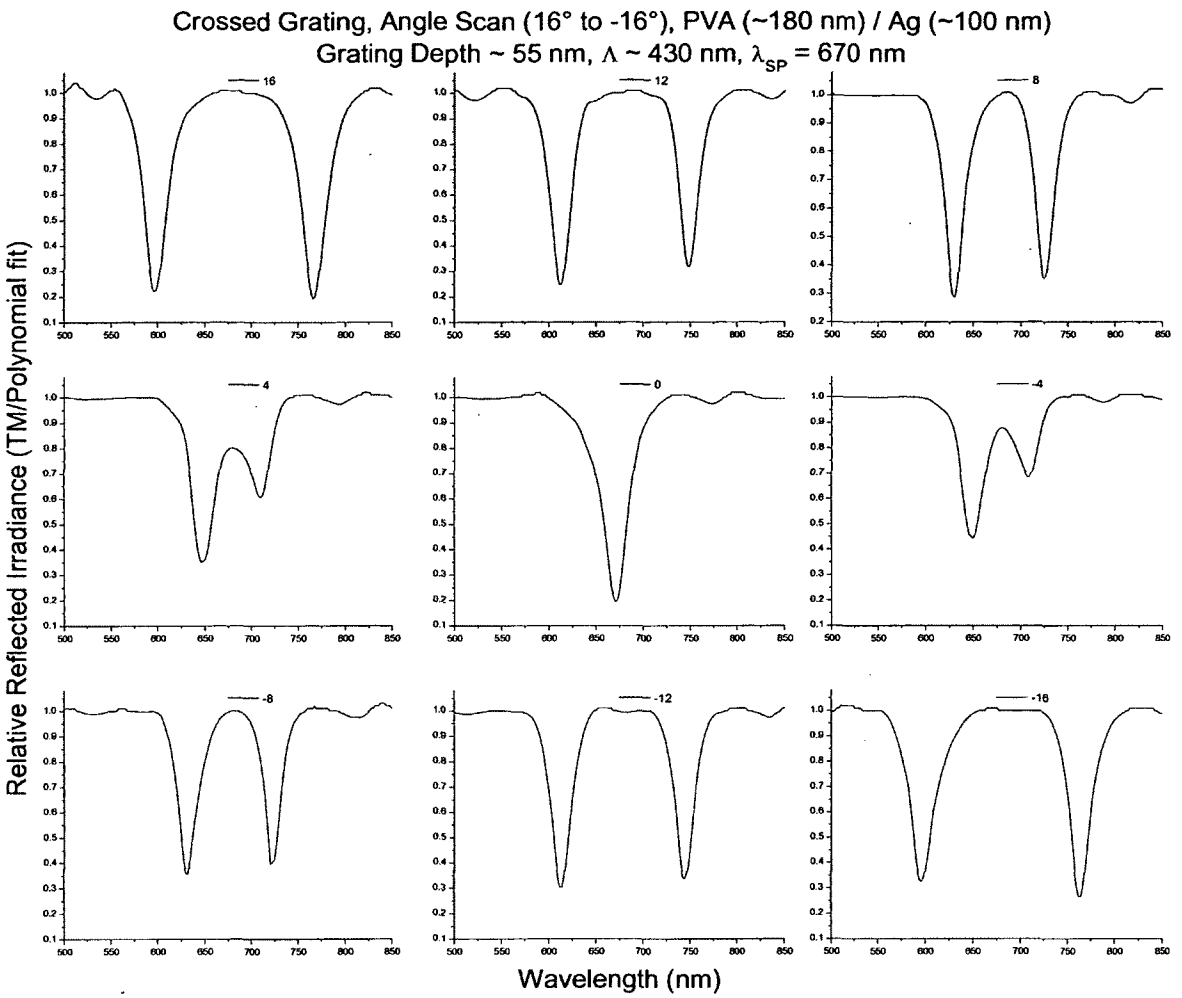

Figure 3.31. TM SPs at a crossed grating PVA-Ag interface for varied θ_i.

Figure 3.32 illustrates an intensity plot of the relative (TM/polynomial fit) reflected irradiance of a crossed grating PVA-ag interface for varied incident angles (16° to -16°) with a fixed TM active grating spacing of $\Lambda \approx 430$ nm and depth of ~55 nm. This is the same test sample as was analyzed in figure 3.31.

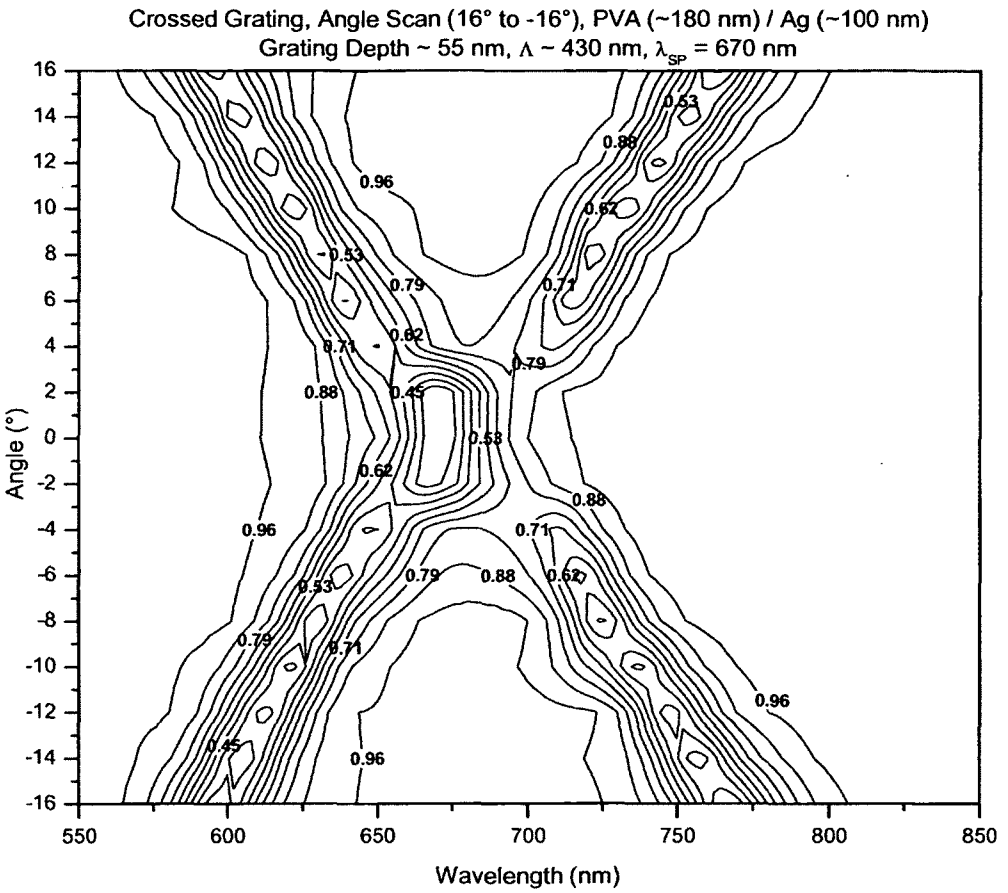

Figure 3.32. TM SPs at a crossed grating PVA-Ag interface for varied θ_i contour.

Figure 3.33 illustrates the same intensity plot shown in figure 3.32, but with colour. One can see that at $\theta_i = 0°$, only one value of λ_{SP} will excite SPs (standing wave), whereas at oblique incidence, two values of λ_{SP} will excite SPs (corresponding to $\pm 1^{st}$ orders).

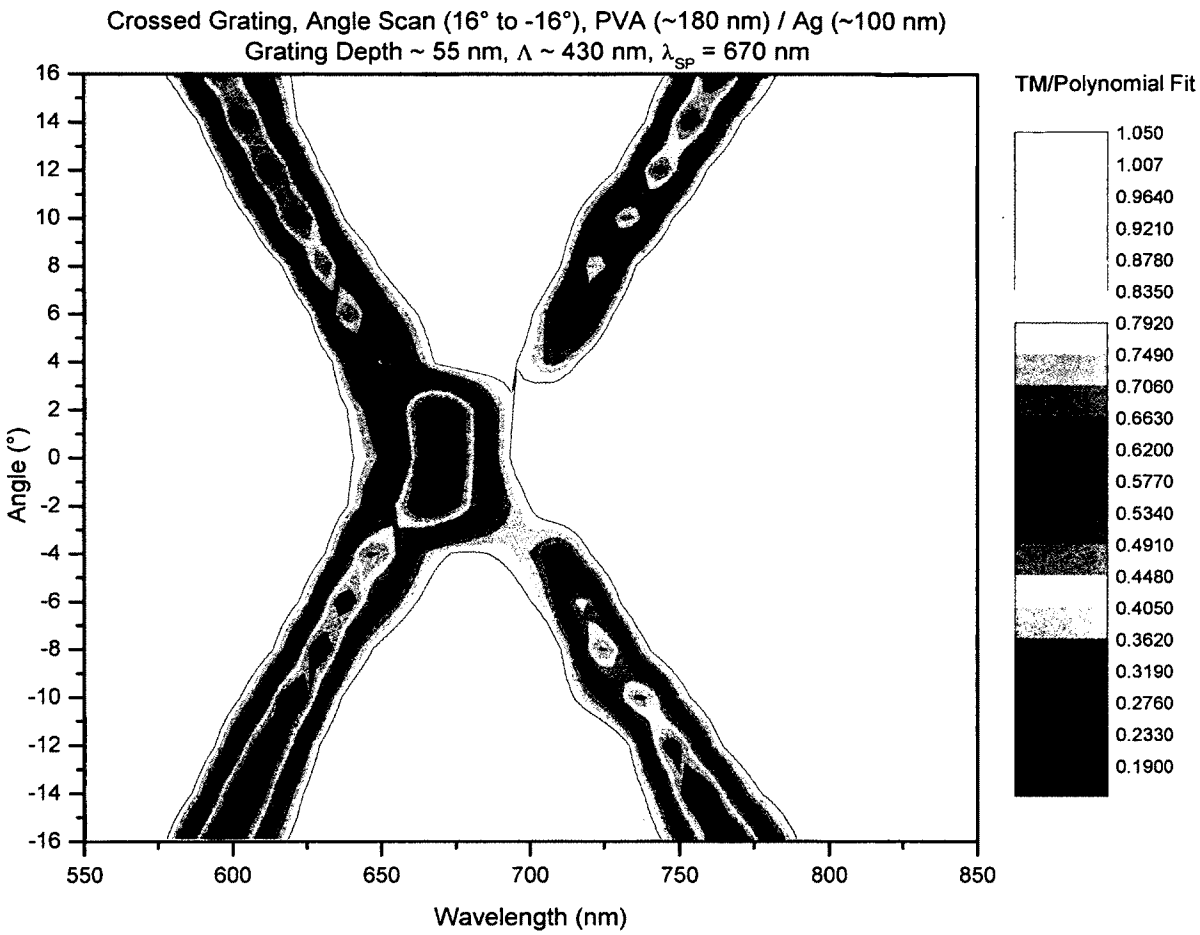

Figure 3.33. TM SPs at a crossed grating PVA-Ag interface for varied θ_i colour.

For the TE active grating, the sample had to be physically turned 90°. Again, this was necessary due to the slight inclination given to the test sample in order for the reflection to bypass the polarizer. Figure 3.34 illustrates a nine-panel plot of the relative (TE/polynomial fit) reflected irradiance of a crossed grating PVA-Ag interface for varied incident angles (16° to -16°) with a fixed TE active grating spacing of $\Lambda \approx 430$ nm and depth of ~25 nm. This grating was written at ~ $1/3$ the exposure time of the TM active grating, accounting for the grating depth of ~25 nm. At normal incidence, $\lambda_{SP} = 674$ nm.

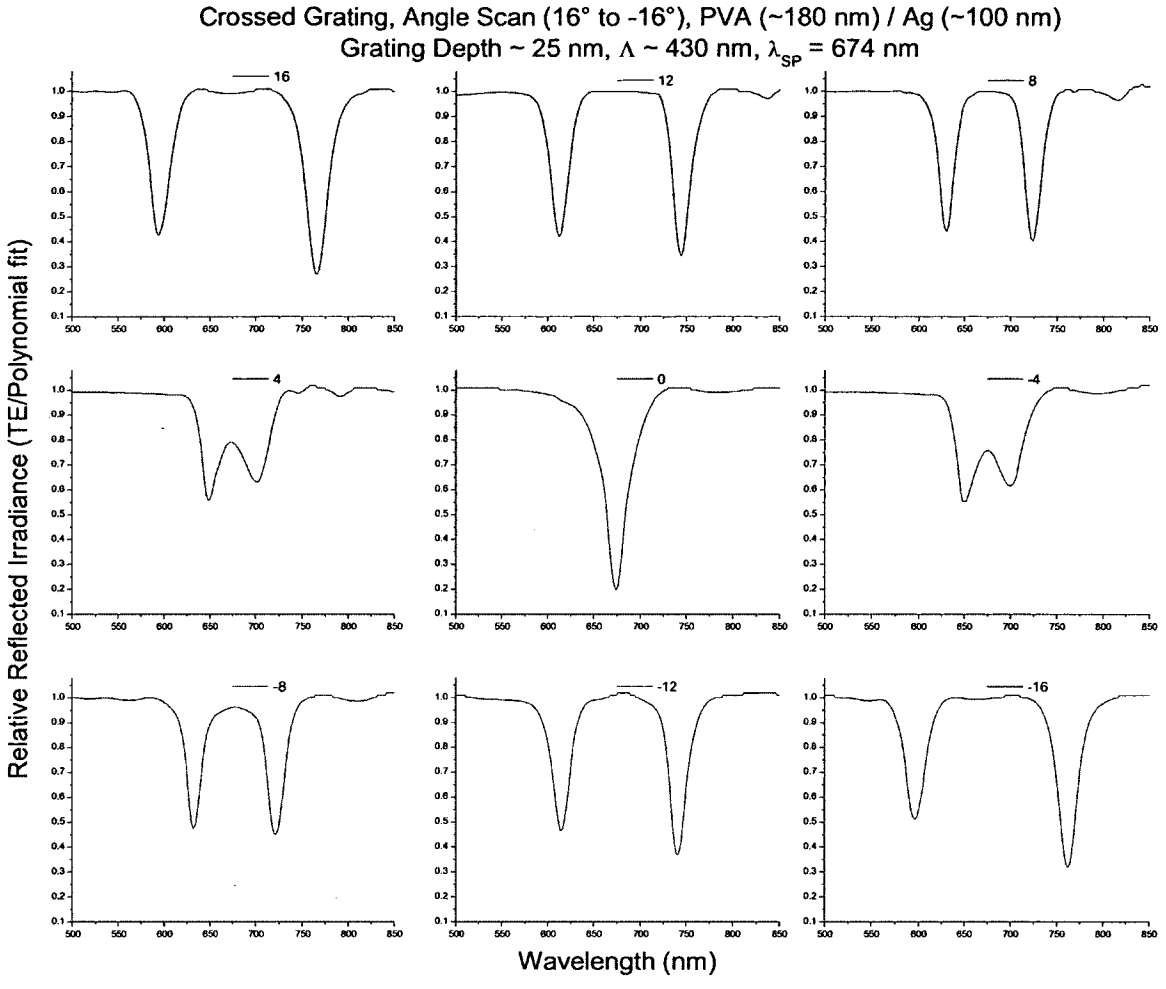

Figure 3.34. TE SPs at a crossed grating PVA-Ag interface for varied θ_i.

Figure 3.35 illustrates an intensity plot of the relative (TE/polynomial fit) reflected irradiance of a crossed grating PVA-Ag interface for varied incident angles (16° to -16°) with a fixed TE active grating spacing of $\Lambda \approx 430$ nm and depth of ~25 nm. This is the same test sample as was analyzed in figure 3.34.

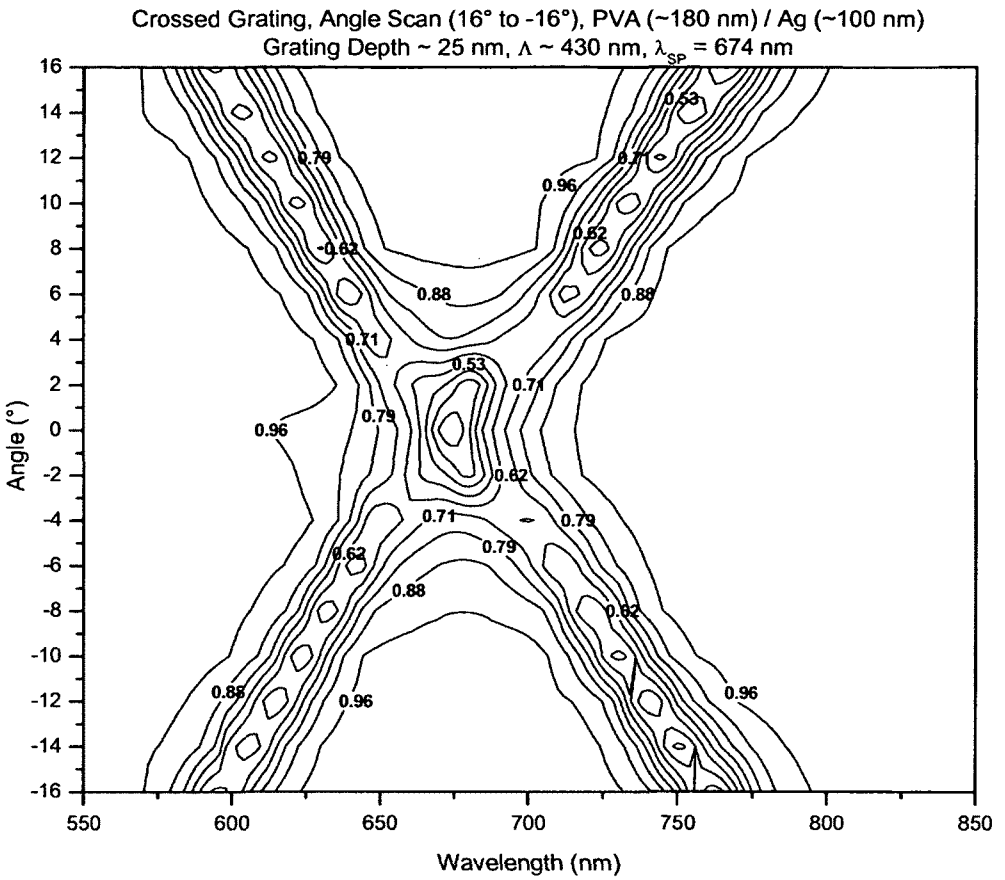

Figure 3.35. TE SPs at a crossed grating PVA-Ag interface for varied θ_i contour.

Figure 3.36 illustrates the same intensity plot shown in figure 3.35, but with colour. Again, given that the TE active grating depth was less than half that of the TM active grating, the former was slightly weaker in the excitation of SPs.

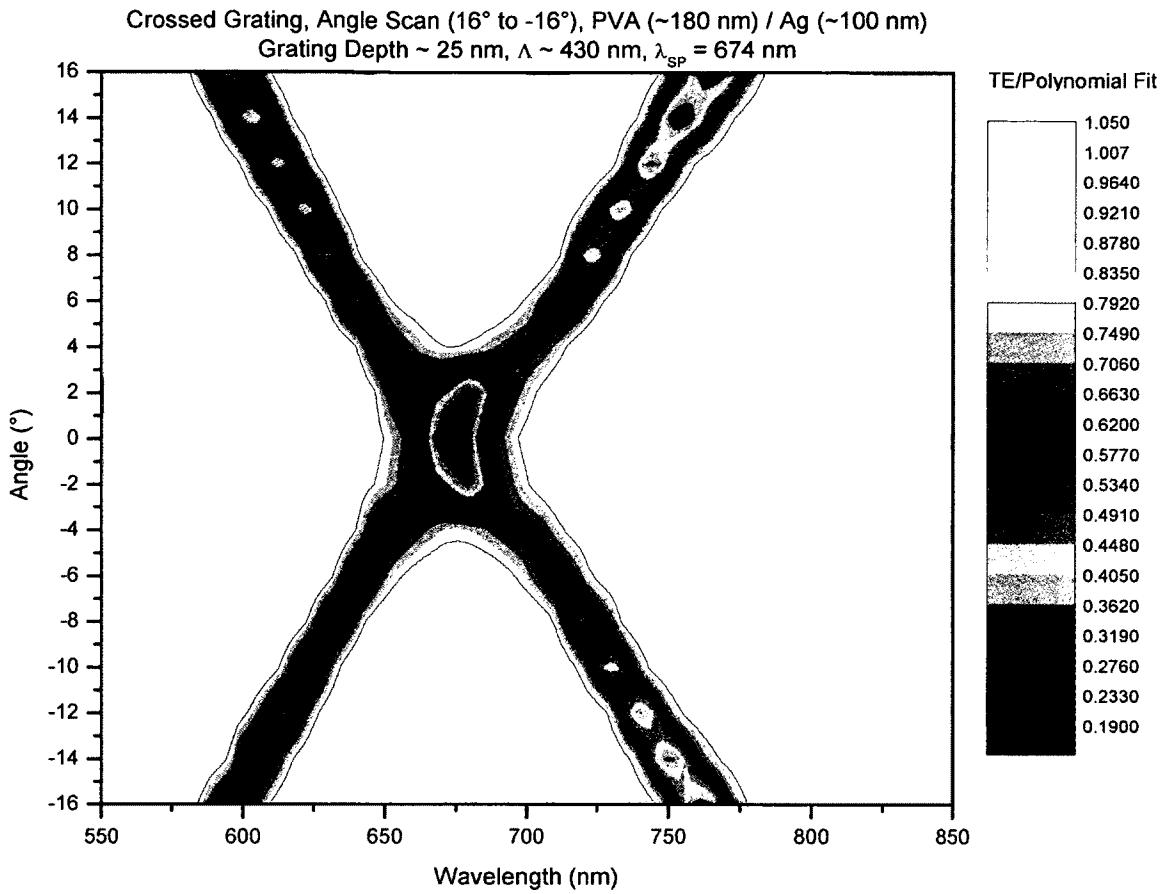

Figure 3.36. TE SPs at a crossed grating PVA-Ag interface for varied θ_i colour.

3.4.3 Parallel Grating Polyvinyl Alcohol (PVA)-Silver (Ag) Interface

Following the analysis of crossed gratings, SPs at a parallel grating PVA-Ag interface were examined. Figure 3.37 illustrates a nine-panel plot of the relative (TM/TE) reflected irradiance of a parallel grating PVA-Ag interface for varied incident angles (14° to -14°) with fixed grating spacings of $\Lambda_1 \approx 460$ nm and $\Lambda_2 \approx 400$ nm. The depth of each grating, Λ_1 and Λ_2, was ~55 nm and ~35 nm respectively. Given that the first grating (Λ_1) was deeper than the second (Λ_2), the former was slightly stronger in the excitation of SPs. At normal incidence, two values of λ_{SP} ($\lambda_{SP} = 626$ nm and 694 nm) excited SPs (representing two standing waves). As the angle of incidence was increased

from zero, four values of λ_{SP} emerged satisfying the $k_{light} = k_{SP}$ condition. These values of λ_{SP} were seen in the graphical results as a splitting of the SPs excited at normal incidence. Compared to an air-Ag interface, this splitting occurred at a much slower rate. This was attributed to both the higher index of the PVA, as well as the smaller spacing of the gratings.

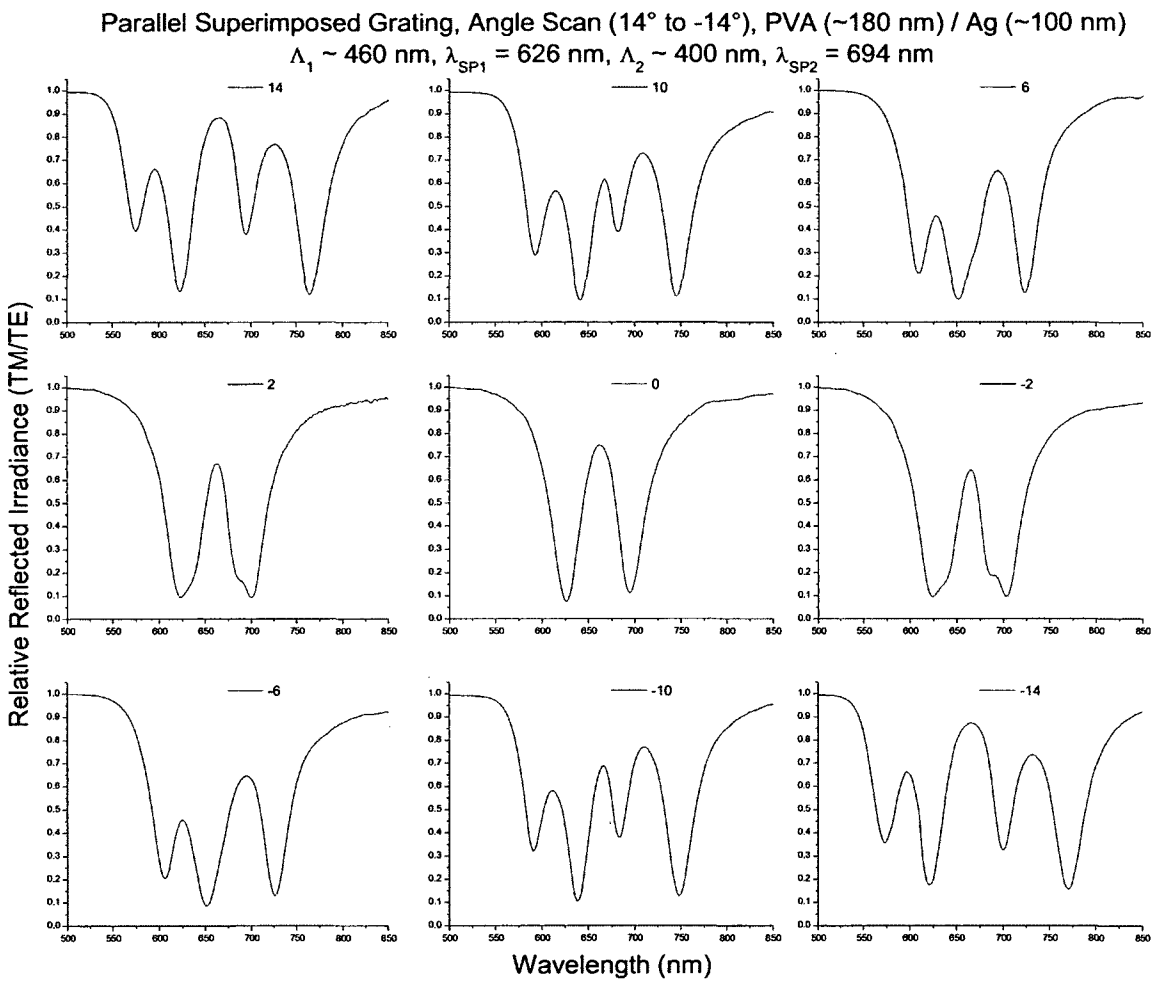

Figure 3.37. SPs at a parallel grating PVA-Ag interface for varied θ_i.

Figure 3.38 illustrates an intensity plot of the relative (TM/TE) reflected irradiance of a parallel grating PVA-Ag interface for varied incident angles (14° to -14°) with fixed grating spacings of $\Lambda_1 \approx 460$ nm and $\Lambda_2 \approx 400$ nm. The depth of each

grating, Λ_1 and Λ_2, was ~55 nm and ~35 nm respectively. This is the same test sample as was analyzed in figure 3.37.

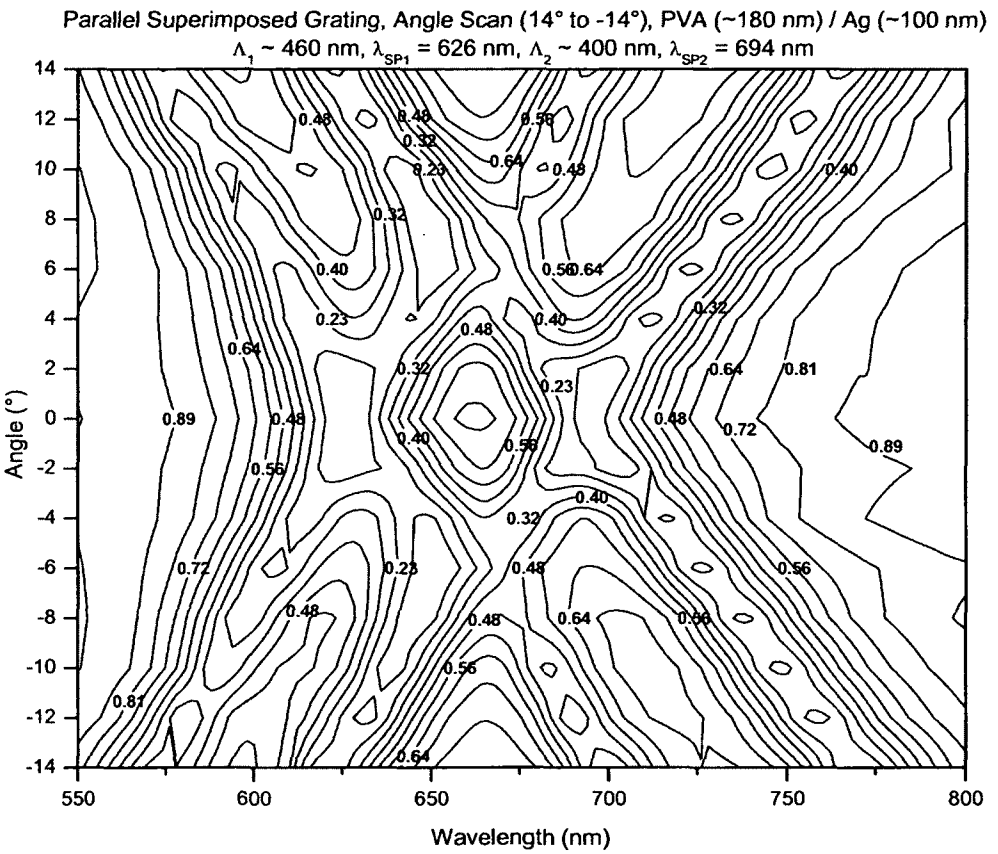

Figure 3.38. SPs at a parallel grating air-Ag interface for varied θ_i contour.

Figure 3.39 illustrates the same intensity plot shown in figure 3.38, but with colour. One can see that the larger grating Λ_1 is slightly stronger than the smaller grating (Λ_2). At normal incidence, only two values of λ_{SP} ($\lambda_{SP,(0,\pm1)}$ and $\lambda_{SP,(\pm1,0)}$) will excite SPs, whereas at oblique incidence, four values of λ_{SP} ($\lambda_{SP,(0,1)}$, $\lambda_{SP,(1,0)}$, $\lambda_{SP,(0,-1)}$, and $\lambda_{SP,(-1,0)}$) will excite SPs. The zoning explanation given for a parallel grating air-Ag interface holds true for the parallel grating PVA-Ag interface shown in figure 3.39.

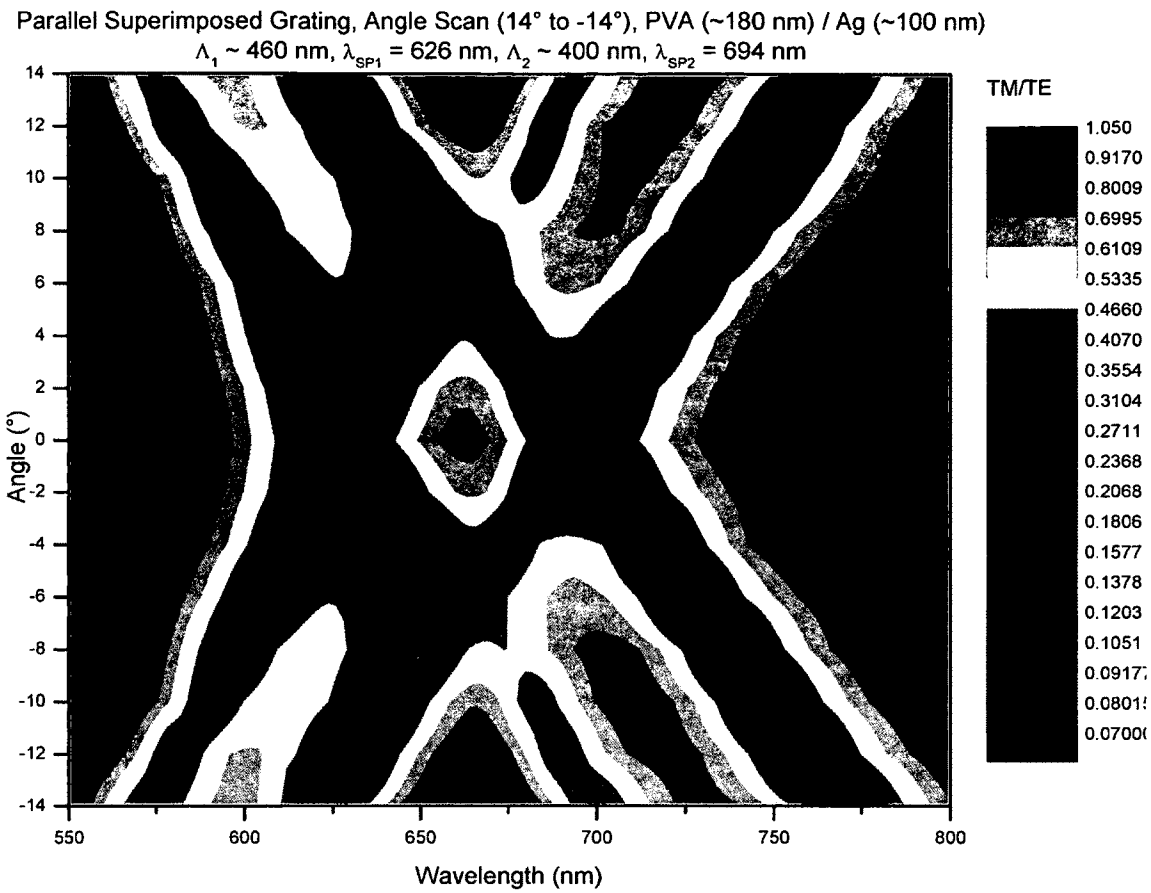

Figure 3.39. SPs at a parallel grating air-Ag interface for varied θ_i colour.

From both air-Ag and PVA-Ag analysis, it was determined that the grating depth and film thickness would be held constant at ~55 nm and ~180 nm respectively, throughout P3HT-PCBM OSC trialing. Also, for both crossed and parallel gratings, the appropriate exposure time rules would remain. These were deemed as the optimal parameters for yielding pure, SP-based photocurrent enhancements in thin film OSCs. For grating depths and film thicknesses beyond these optimal values, band gaps and coupling effects become quite apparent. Furthermore, grating spacings would be chosen based on the desired location of SP excitation.

REFERENCES

[1] P. Rochon and E. Batalla, "Optically Induced Surface Gratings on Azoaromatic Polymer Films," *Applied Physics Letter,* vol. 66, no. 2, pp. 136-138, 1995.

[2] X. Li, A. Natansohn, S. Kobayashi and P. Rochon, "An Optically Controlled Liquid Crystal Device Using Azopolymer Films," *Journal of Quantum Electronics,* vol. 36, no. 7, pp. 824-827, 2000.

[3] P. Rochon, "Optically Inscribed Volume or Surface Structures in Azobenzene Polymer Films," *Optics and Spectroscopy,* vol. 103, no. 6, pp. 858-861, 2007.

[4] L. Levesque and P. Rochon, "Surface Plasmon Photonic Bandgap in Azopolymer Gratings Sputtered with Gold," *Journal of the optical Society of America A,* vol. 22, no. 11, pp. 2564-2568, 2005.

[5] R. Sabat, M. Santos and P. Rochon, "Surface Plasmon-Induced Band Gap in the Photocurrent Response of Organic Solar Cells," *International Journal of Photoenergy,* vol. 2010, p. 698718, 2010.

[6] R. Kumar, A. Singh, A. Kapoor and K. Tripathi, "Fabrication and Characterization of Polyvinyl-Alcohol-based Thin-Film Optical Waveguides," *Optical Engineering,* vol. 43, no. 9, pp. 2134-2142, 2004.

[7] M. Weber, Handbook of Optical Materials, Boca Raton: CRC Publishing, 2003.

[8] M. Sefunc, A. Okyay and H. Demir, "Plasmonic Backcontact Grating for P3HT:PCBM Organic Solar Cells Enabling Strong Optical Absorption Increased in all Polarizations," *Optics Express,* vol. 19, no. 15, pp. 14200-14209, 2011.

[9] W. Barnes, "Surface Plasmon Subwavelength Optics," *Nature,* vol. 424, no. 6950, pp. 824-830, 2003.

[10] J. Müller, B. Rech, J. Springer and M. Vanecek, "TCO and Light Trapping in Silicon Thin Film Solar Cells," *Solar Energy,* vol. 77, no. 6, p. 917–930, 2004.

CHAPTER 4: THIN FILM ORGANIC SOLAR CELLS (OSCs)

Chapter four is designed to provide the reader with the methodology used, and results obtained, during the OSC trials. The entire experimental procedure will be discussed, beginning with the fabrication and continuing through to OSC result analysis. Generic manufacturing considerations and techniques will be discussed, followed by the presentation and discussion of results. The results will be arranged based on OSC grating schemes, with those relating to single gratings being provided first, followed by those relating to crossed and superimposed gratings. All unique manufacturing and analytical related apparatuses will be illustrated and discussed.

4.1 Organic Solar Cell (OSC) Fabrication Process

4.1.1 Grating Inscription and Verification

Surface-relief diffraction gratings were optically inscribed into pDR1M azopolymer films (~200 nm) using the same apparatus outlined in figure 3.1. This time however, light from a Spectra-Physics Stabilite 2017 argon laser with a wavelength of 458 nm and output power of 200 mW was filtered and collimated to ~3.4 cm in diameter, yielding a plane wave writing beam with an irradiance of ~22 $mW \cdot cm^{-2}$. The use of this shorter wavelength laser allowed gratings to be written with spacings as small as $\Lambda \approx 240$ nm. Due to its relatively low irradiance compared to the diode-pumped laser, exposure times required to achieve desired grating depths were much longer. For a grating of spacing, $\Lambda \approx 240$ nm, it was found that an exposure time of ~1500 secs yielded a grating depth of ~55 nm. Both grating spacings and depths were verified using an AFM.

4.1.2 Metal Deposits

Once the desired gratings were inscribed onto the azopolymer film, an ~100 nm thin layer of aluminum (Al) was evaporated onto the sample using a Key High Vacuum Products, Inc. Evaporator. The layer thickness was controlled by adjusting the evaporation power current, and made thick enough such that it was completely opaque to the majority of incident light being reflected. Evaporation is considered a non-intrusive method of depositing a thin metal layer, whereas sputter coating is considered intrusive. While not necessary during the deposit of the bottom (Al) electrode, evaporation was necessary during the deposit of the top (Au) electrode, since it avoided metal intrusion into the photoactive layer. In order to monitor the thickness of the electrode deposits in real-time, the resistance, R, of the deposit was measured using Fluke 25 multi-meter connected to each end of the electrode strip. The thickness of the deposit was predicted using the relationship given by equation 4.1 [1]:

$$R = \frac{\rho L}{A} = \frac{\rho L}{wt} \rightarrow t = \frac{\rho L}{wR} \tag{4.1}$$

where ρ is a measure of the material's ability to oppose electric current, known as its resistivity, L is the length of the deposit, and A is the cross-sectional area of the deposit ($A = wt$), as shown in figure 4.1.

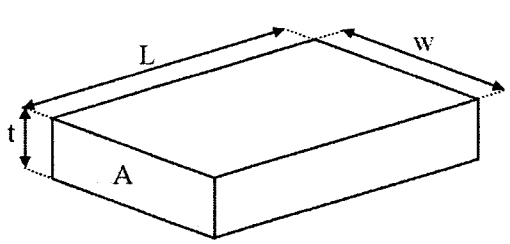

Figure 4.1. Dimensions of metal deposit.

Both the length and width of the electrode strips in all evaporations were fixed at $L = 3.5 \cdot 10^{-2}$ m and $w = 4.2 \cdot 10^{-3}$ m, respectively. The resistivity of Al at 20°C is $2.82 \cdot 10^{-8}$ Ω·m, whereas that of Au is $2.44 \cdot 10^{-8}$ Ω·m [2]. Thus, in order for an ~100 nm thin layer of Al to be evaporated, current was applied until the multi-meter measured a resistance of $R \approx 2.5$ Ω. Thicknesses predicted using this resistance monitoring system, were verified using a Sloan Dektak II surface profiler, and proved to be in good agreement with experimental measurements. Aluminum deposited to a real-time, multi-meter resistance of $R \approx 2.5$ Ω ($t = 100$ nm), yielded small discrepancies of $t = 111.3 \pm 5.2$ nm.

4.1.3 P3HT:PCBM Photoactive Blend

Once the bottom (Al) electrode was deposited, it was time to prepare and deposit the photoactive layer. Due to its availability and proven success [3], [4], [5], [6], the commonly used bulk hetero-junction blend of the polymer poly (3-hexylthiophene) (P3HT) and the fullerene [6,6]-phenyl C_{61}-butyric (PCBM) was chosen as the photoactive layer. The P3HT serves as the electron donor, while the PCBM serves as the electron acceptor [7]. Absorption of incident light photons result in charge separation and the subsequent formation of electron-hole pairs. The electrons are transported via the acceptor domains, and collected by the bottom (Al) electrode, whereas the holes are pulled in the opposite direction and collected by the top (Au) electrode, thus generating photocurrent [8], [9]. The metals Al and Au were chosen as the harvesting electrodes based on their proven success and compatibility with the P3HT:PCBM blend [6], [10], [11]. Figure 4.2 illustrates the P3HT:PCBM bulk hetero-junction layer sandwiched between the two harvesting electrodes. Notice the electron is donated by P3HT, accepted and transported

by the PCBM, and subsequently collected by the Al electrode. The hole is pulled in the opposite direction to the Au electrode.

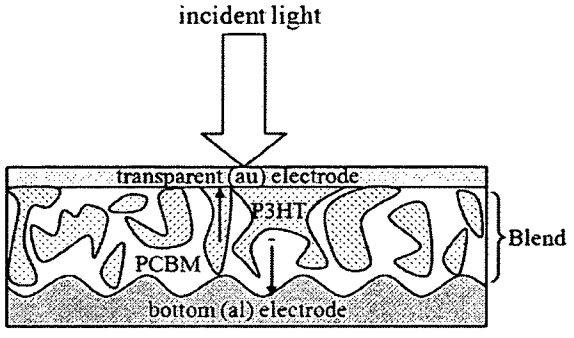

Figure 4.2. P3HT:PCBM bulk hetero-junction blend.

The energy, E, required for charge separation is provided by the incident light photons and given by equation 4.2:

$$E = hf = \frac{hc}{\lambda} \tag{4.2}$$

where h is known as Planck's constant, while the other parameters are as previously defined.

4.1.4 Organic Solar Cell (OSC) Architecture

A (1:1) P3HT:PCBM solution was diluted in chlorobenzene with a mix ratio of 5% weight/weight. This solution was thoroughly mixed using an ultrasonic bath and a mechanical shaker. The P3HT:PCBM blend was then spin-coated on top of the Al electrode with a thickness of ~180 nm, and annealed at 95°C for 1 hour under N_2 atmosphere. Annealing has been shown to improve the performance of P3HT-based OSCs [9]. Finally, a very thin layer of Au (~10 nm) was evaporated on top of the

P3HT:PCBM blend, to serve as the second, harvesting electrode. The completed SP-based, P3HT:PCBM OSC architecture was as illustrated in figure 4.3.

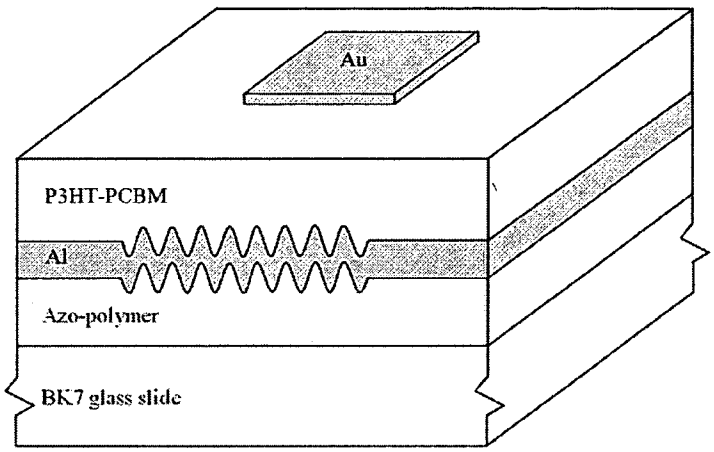

Figure 4.3. Architecture of a SP-based, P3HT-PCBM OSC.

4.2 Organic Solar Cell (OSC) Analysis

4.2.1 Organic Solar Cell (OSC) Analysis Apparatus

Once the OSCs were fabricated, they were placed on an analytical set-up as illustrated in figure 4.4. Light from a spectrometer was passed through a mechanical chopper and circularly polarized using a $\lambda/4$ plate. It was then collimated and reflected off of a concave mirror and through a polarizer, before being incident upon the OSC, which was located on a computer-controlled rotary mount. The signal from the OSC was amplified by a lock-in amplifier and recorded on a computer. The illuminated section of the P3HT:PCBM layer was $\sim 2 \times 4$ mm^2.

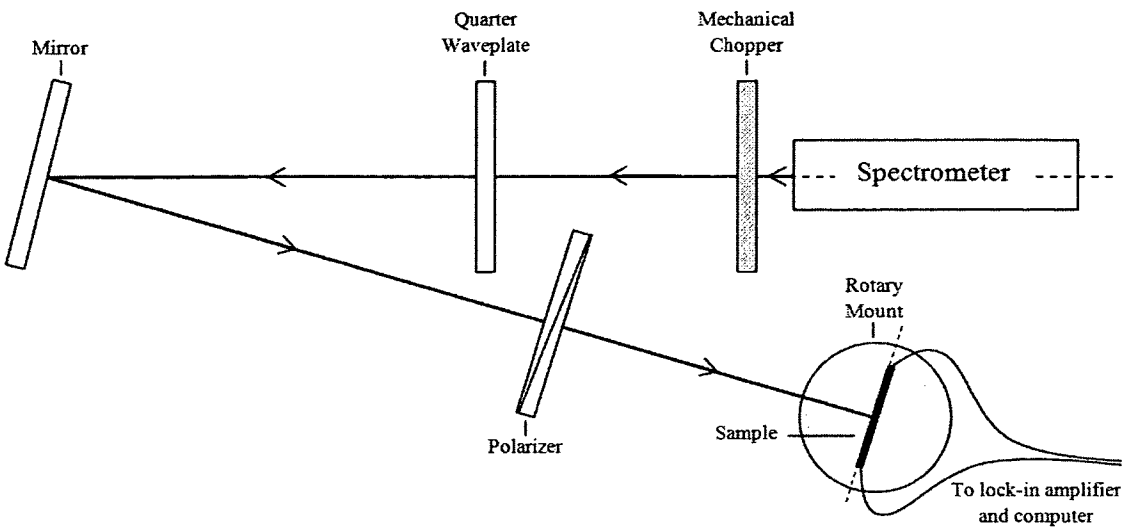

Figure 4.4. Overview of OSC analytical set-up.

During earlier air and PVA trials, SPs were being directly measured by viewing the irradiance response of the samples with a photo detector. With the OSCs, the sample becomes the photo detector, and its photocurrent response is measured. Enhancements in this response due to SP excitation are seen. Since no tilting of the sample was necessary during OSC analysis, TM and TE photocurrent responses were obtained by simply adjusting the polarizer accordingly for all grating configurations.

4.2.2 Organic Solar Cell (OSC) Photocurrent Response

Using the apparatus described above, the direct photocurrent response of OSCs was measured in amperes (A). In order to assess the performance of the OSCs in terms of A/W, it was first necessary to determine the characteristic wattage (W) curve of the spectrometer lamp within the desired optical regime. This was done by first obtaining the characteristic A/W curve of the photo detector from the manufacturer website (United Detector Technology Sensors, Inc.). This photo detector was then used to measure the

ampere (A) response of the lamp. The wattage (W) curve of the lamp was calculated by taking the characteristic A/W curve of the photo detector and dividing by the ampere (A) response of the lamp. Thus, the A/W curves of the OSCs were obtained by taking its photocurrent response (A) and dividing by the wattage curve (W) of the lamp. Photocurrent enhancements were seen as increases in both A and A/W curves of all SP-based, OSCs.

4.2.3 Single Grating Analysis

For a P3HT:PCBM-aluminum (dielectric-metal) interface at 600 nm, $n_d \approx 2.1$ [12], and $\tilde{\varepsilon}'_{r,m} \approx -51.1225$ [13], the SP excitation wavelength equation (2.54) becomes $\lambda_{SP} \approx 2.1(1.046 \mp \sin\theta_i)\Lambda$. Thus, at normal incidence, with a grating spacing of $\Lambda = 250$ nm, the SP excitation wavelength is $\lambda_{SP} \approx 549$ nm. Figure 4.5 illustrates the A/W response of a single grating, P3HT:PCBM OSC at normal incidence for both TM and TE polarized incident light. The thickness of the P3HT:PCBM layer is ~180 nm, and the grating spacing, $\Lambda \approx 250$ nm. The predicted SP excitation wavelength is represented in the figure as a vertical dotted line.

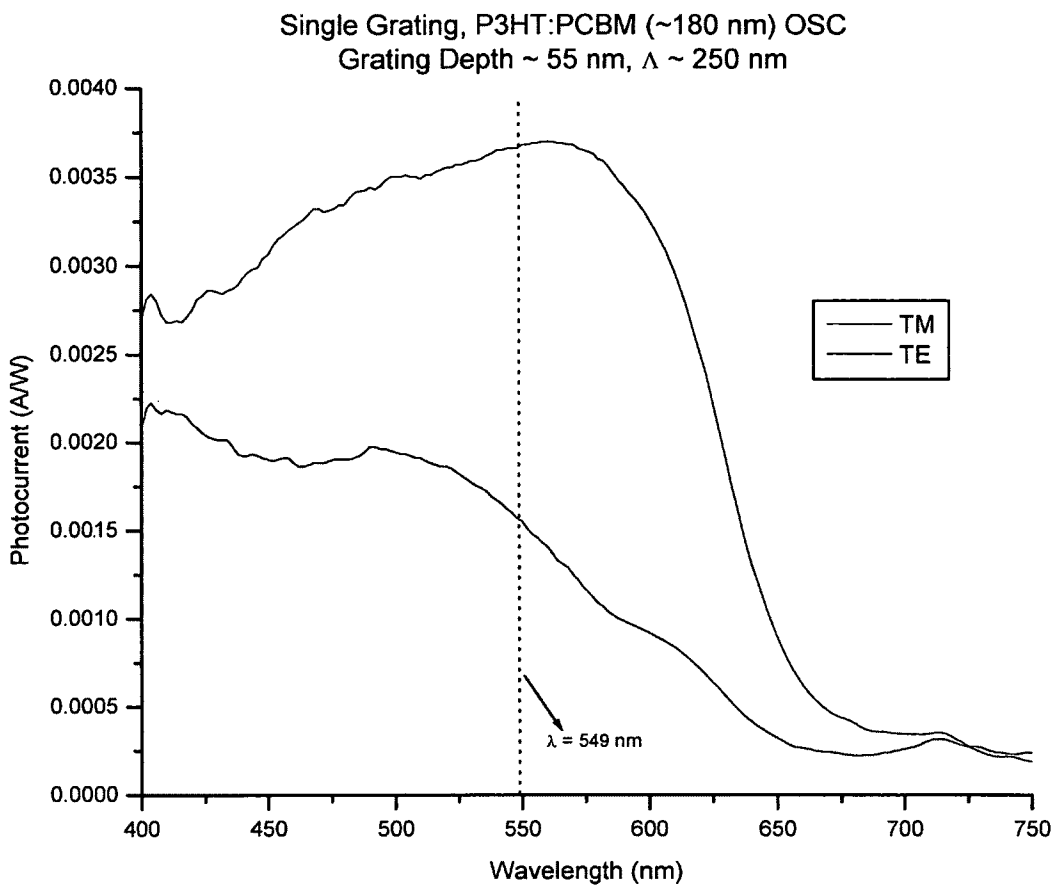

Figure 4.5. Photocurrent response of a single grating, P3HT:PCBM OSC at $\theta_i = 0$.

One can see from figure 4.5 that there is a noticeable increase in the photocurrent generation of the OSC in the TM response. This was expected, since the sample was oriented such that its grating would generate SPs with TM polarized incident light. Photocurrent enhancements were observed over a wide range of wavelengths. This may be attributed to the widely varying, wavelength-dependent, refractive index of the P3HT:PCBM blend over the desired optical regime (i.e. $1.58 < n < 2.17$) [12], making multiple SP excitation wavelengths possible. Another possible cause for these broad photocurrent enhancements may be attributed to the increased optical path length caused by the diffraction of light, resulting in improved light absorption. In any case, these

broad photocurrent enhancements somewhat disguised the SP excitation wavelengths throughout the experimental results, making them very difficult to pinpoint, especially at oblique incidence.

Figure 4.6 illustrates the relative photocurrent response (TM/TE) of OSCs at normal incidence for two different, single grating spacings. The thickness of the P3HT:PCBM layer is ~180 nm, and the grating spacings are, $\Lambda \approx 250$ nm and $\Lambda \approx 280$ nm.

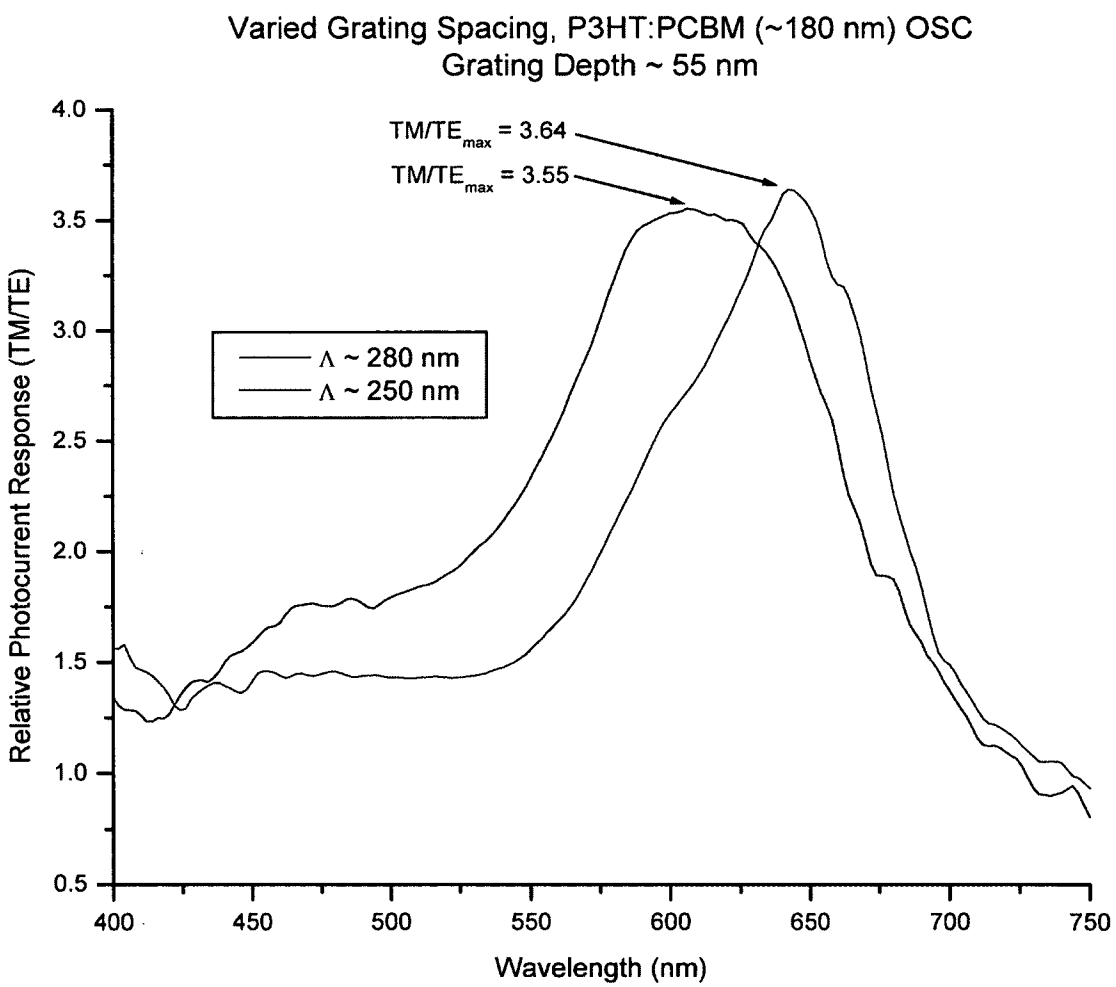

Figure 4.6. Relative photocurrent response at $\theta_i = 0$ for different single grating spacings.

One can see from figure 4.6 that for a single grating spacing of $\Lambda \approx 250$ nm and $\Lambda \approx 280$ nm, relative photocurrent enhancements of 3.55 and 3.64 were observed, respectively. As expected, enhancements due to the larger grating (i.e. $\Lambda \approx 280$ nm) were observed at higher wavelengths compared to that of the smaller grating (i.e. $\Lambda \approx 250$ nm).

Figure 4.7 illustrates the photocurrent response of a single grating OSC for varied angles of incidence (0° to 20°) with a fixed grating spacing of $\Lambda_1 \approx 250$ nm. The predicted SP excitation wavelength at normal incidence is represented in the figure as a black vertical dotted line, whereas those predicted for an angle of incidence of $\theta_i = 10°$ are represented as two red vertical dotted lines (i.e. $\lambda_{SP} \approx 458$ and 640 nm). The predicted SP excitation wavelengths for an angle of incidence of $\theta_i = 20°$ fall outside of the absorption range of the P3HT:PCBM blend (i.e. $\lambda_{SP} \approx 370$ and 728 nm).

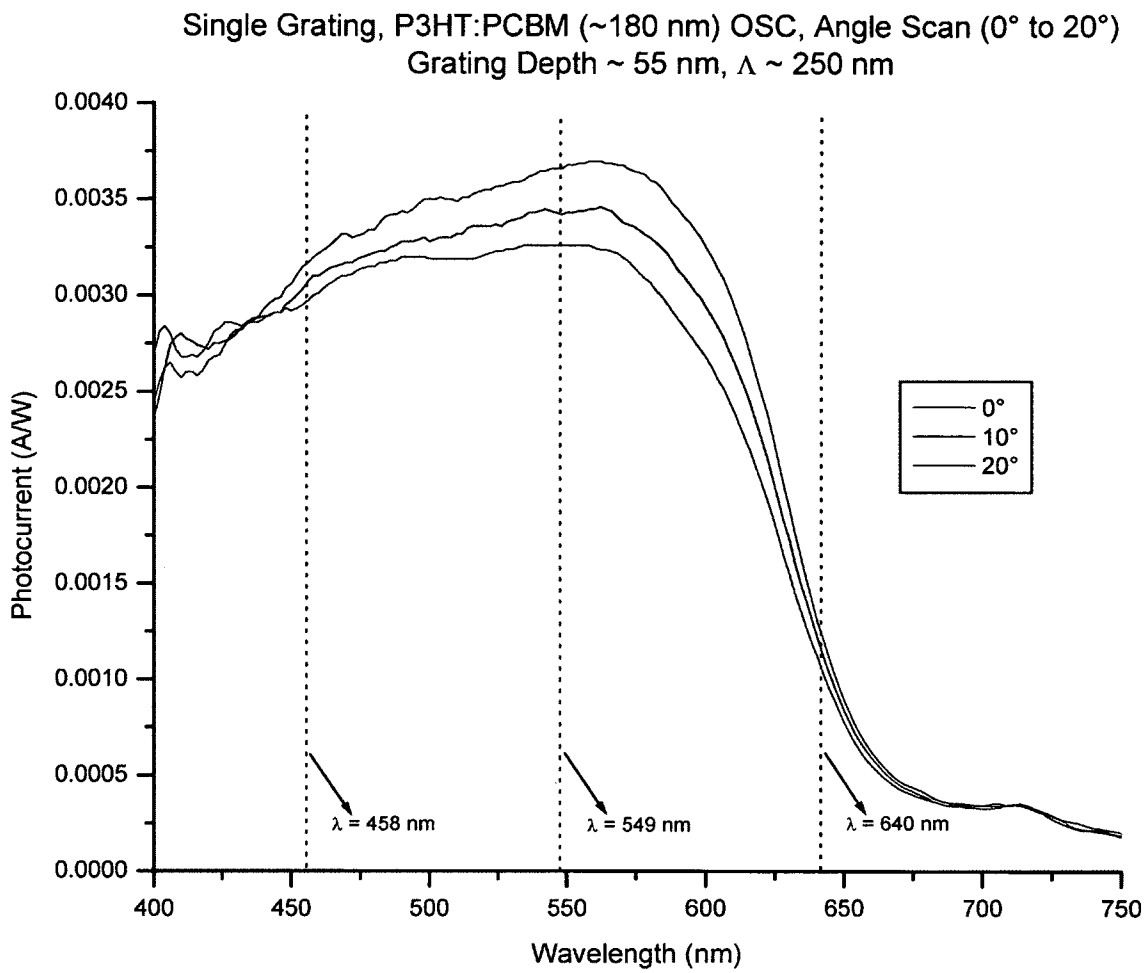

Figure 4.7. Photocurrent response of a single grating OSC for varied θ_i.

As seen in figure 4.7, larger photocurrent enhancements are present at normal incidence. This is believed to be due to the overlapping contributions from both the $\pm 1^{st}$ orders present in the standing wave. The characteristic SP splitting previously seen in air and PVA trials were not evident in OSC results. This may be due to several factors, including the fact that indirect, as opposed to direct, SP effects were being measured during OSC experimentation, making their presence less apparent. Another possible factor may be the aforementioned broad range over which photocurrent enhancements

were observed, also making them less apparent, especially at oblique incident where no standing wave is present.

4.2.4 Crossed Grating Analysis

Following the analysis of single grating OSCs, crossed grating OSCs were examined. The spacings of both TM and TE active gratings were equal, with the exposure time of the latter being $\sim 1/3$ that of the former. Figure 4.8 illustrates the A/W response of a crossed grating OSC at normal incidence for both TM and TE polarized incident light. The A/W response of a non-grating OSC at normal incidence is also provided for comparison. The thickness of the P3HT:PCBM layer is ~180 nm, and the grating spacing is $\Lambda \approx 240$ nm. For a P3HT:PCBM-aluminum interface at normal incidence, with a grating spacing of $\Lambda = 240$ nm, the SP excitation wavelength is $\lambda_{SP} \approx 527$ nm. Given that that TE active grating depth was less than half that of the TM active grating, the former was slightly weaker producing photocurrent enhancements. The predicted SP excitation wavelength is represented in the figure as a vertical dotted line.

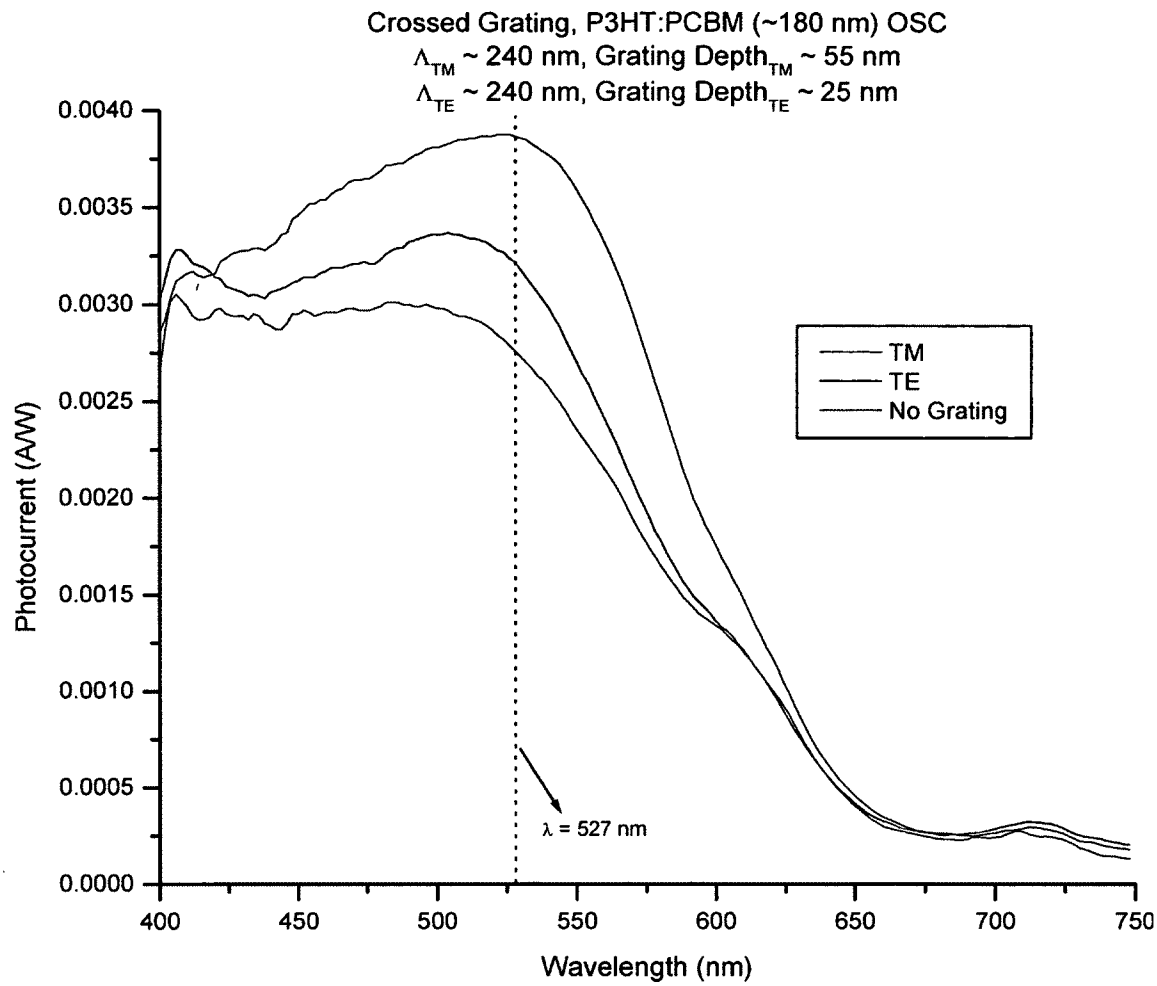

Figure 4.8. Photocurrent response of a crossed grating OSC at $\theta_i = 0$.

Figure 4.9 illustrates the relative photocurrent response (TM/TE) of a crossed grating OSC at normal incidence. This is the same OSC as was analyzed in figure 4.8. As expected, the relative response is near unity, and slightly favouring the TM polarized incident light.

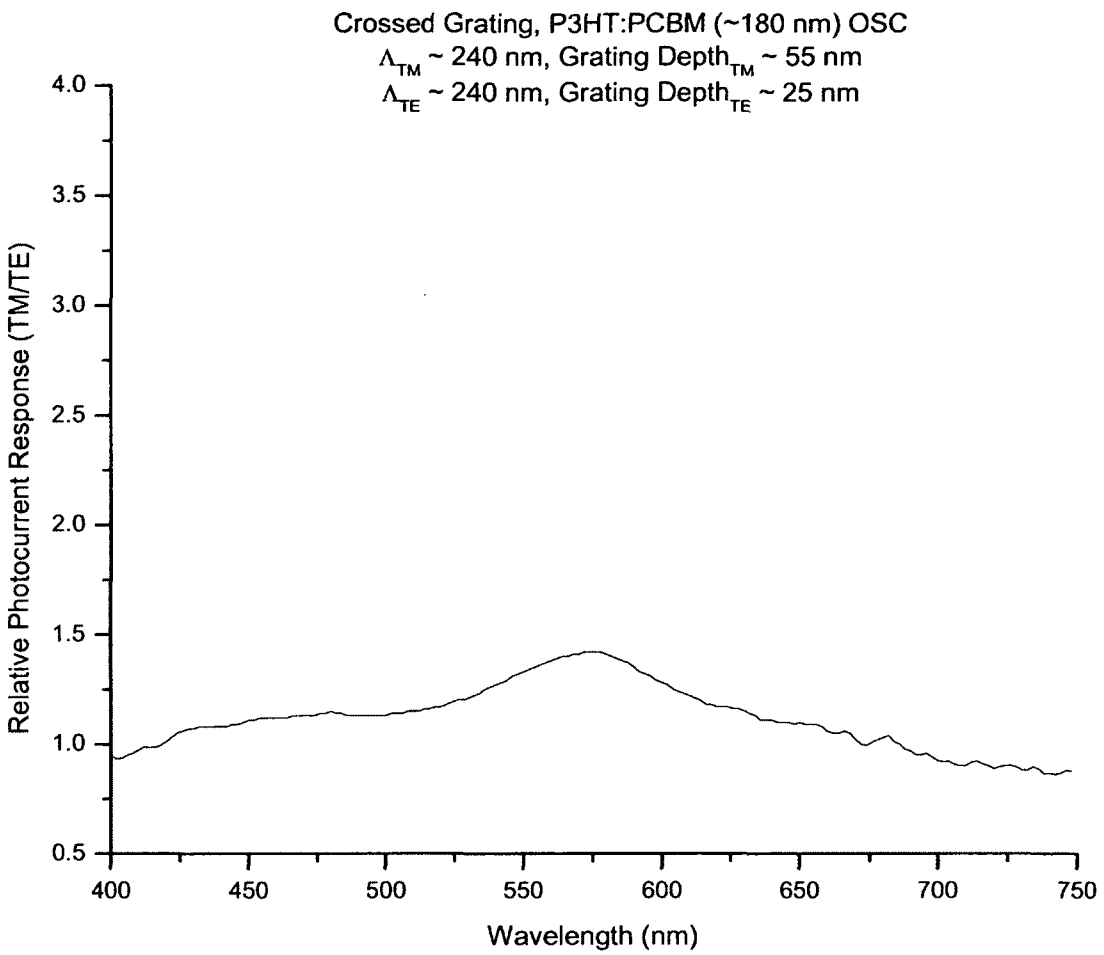

Figure 4.9. Relative photocurrent response of a crossed grating OSC.

4.2.5 Parallel Grating Analysis

Following the analysis of crossed grating OSCs, parallel grating OSCs were examined. The larger grating was first written, followed by the smaller grating, i.e. $\Lambda_1 > \Lambda_2$, with the exposure time of the smaller being $\sim 1/2$ that of the larger. Figure 4.10 illustrates the A/W response of a parallel grating OSC for both TM and TE polarized incident light. The grating spacings are $\Lambda_1 \approx 280$ nm and $\Lambda_2 \approx 240$ nm. The depth of each grating, Λ_1 and Λ_2, was ~55 nm and ~35 nm, respectively. The predicted SP excitation wavelength for a P3HT:PCBM-aluminum interface at normal incidence, with

grating spacings of $\Lambda_1 = 280$ nm and $\Lambda_2 = 240$ nm, are $\lambda_{SP,\Lambda_1} \approx 615$ nm and $\lambda_{SP,\Lambda_2} \approx 527$ nm, respectively. These values are represented in the figure as vertical dotted lines.

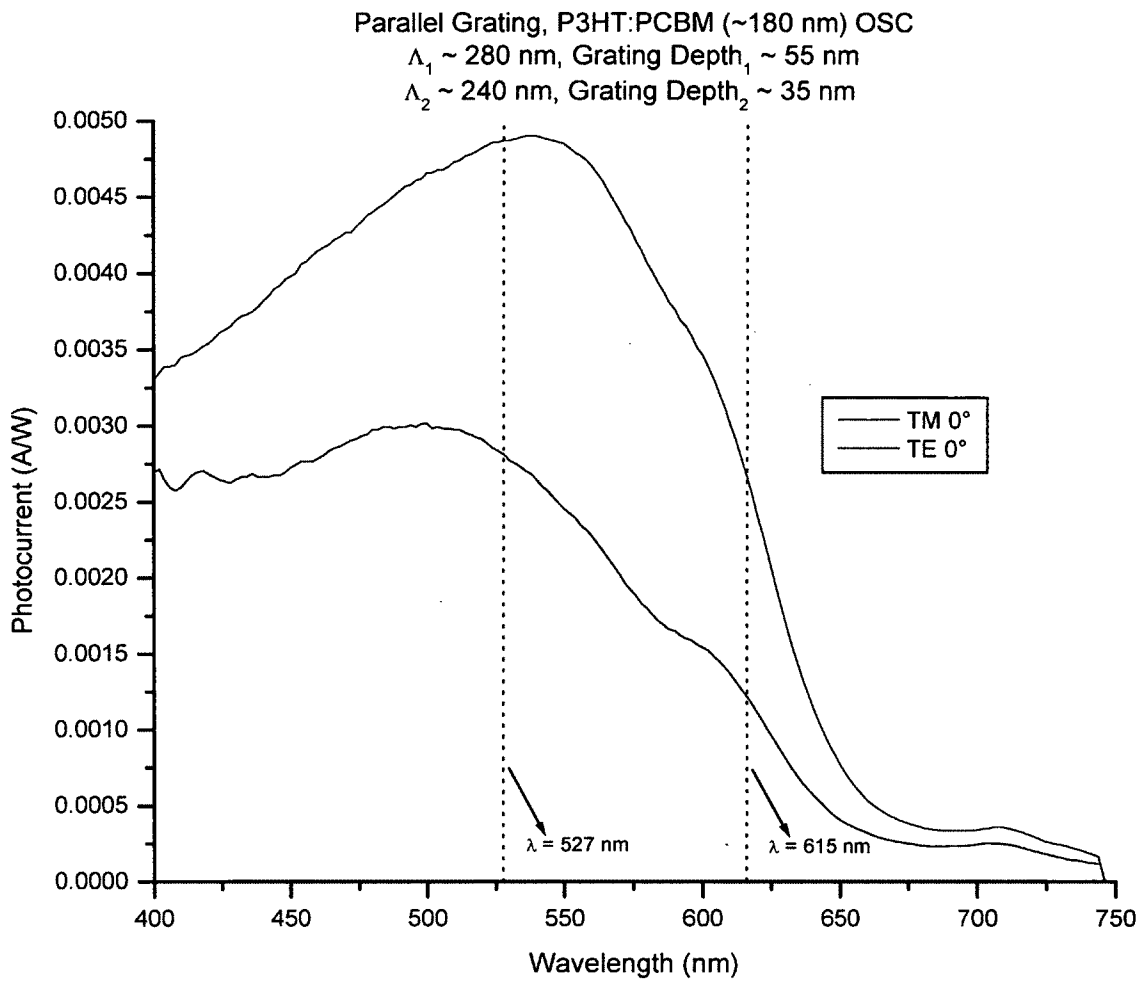

Figure 4.10. Photocurrent response of a parallel grating, P3HT:PCBM OSC.

Figure 4.11 illustrates the relative photocurrent response (TM/TE) of a parallel grating OSC compared to that of a single grating OSC, at normal incidence for TM polarized incident light. The grating spacings of the parallel grating are $\Lambda_1 \approx 280$ nm and $\Lambda_2 \approx 240$ nm, while that of the single grating is $\Lambda \approx 240$ nm. The depth of each

grating, Λ_1 and Λ_2, was ~55 nm and ~35 nm, respectively, while that of the single grating was ~55 nm.

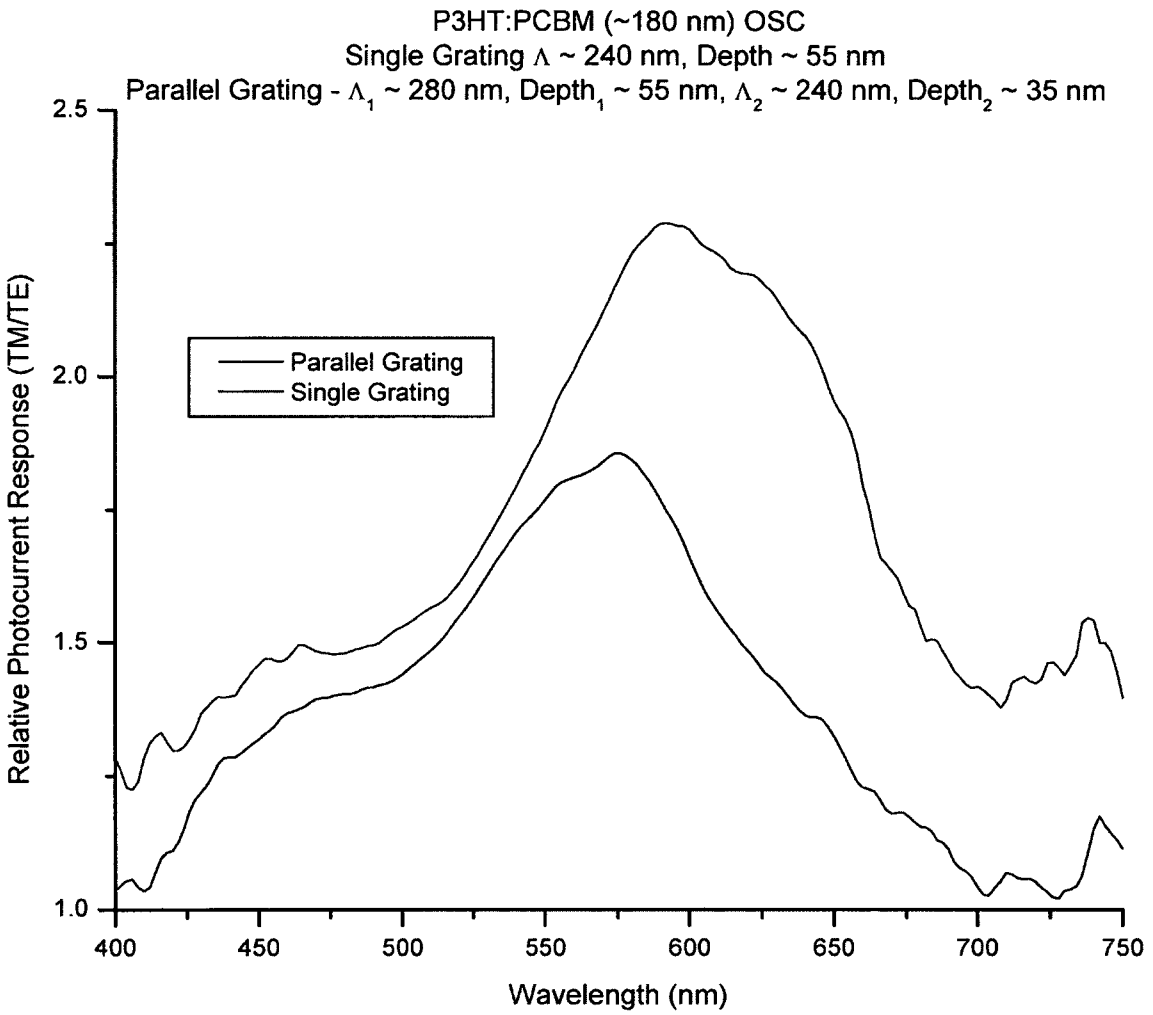

Figure 4.11. Relative photocurrent response at $\theta_i = 0$ for a single versus parallel OSC.

One can see that the relative photocurrent enhancement of the parallel grating is both larger and over a broader range of wavelengths, compared to that of the single grating OSC.

Figure 4.12 illustrates the A/W response of a parallel grating OSC compared to that of a single grating OSC, at normal incidence for TM polarized incident light. These

are the same OSCs as were analyzed in figure 4.11. The predicted SP excitation wavelength for a P3HT:PCBM-aluminum interface at normal incidence, with grating spacings of $\Lambda_1 = 280$ nm and $\Lambda_2 = 240$ nm, are $\lambda_{SP,\Lambda_1} \approx 615$ nm and $\lambda_{SP,\Lambda_2} \approx 527$ nm, respectively. These values are represented in the figure as vertical dotted lines.

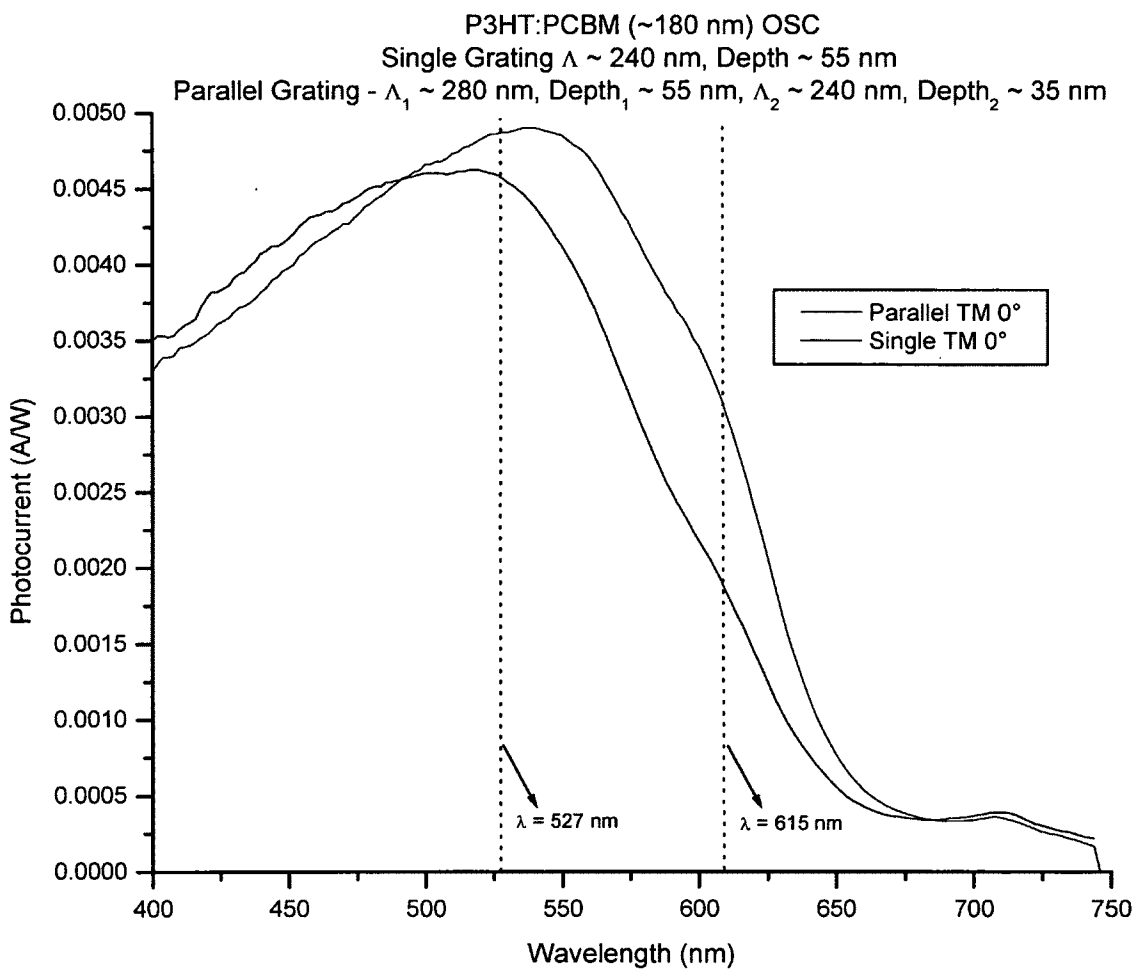

Figure 4.12. Photocurrent response of a single versus parallel grating OSC.

As seen in figure 4.12, the enhanced photocurrent response of the parallel grating OSC is over a broader range of wavelengths compared to that of a single grating. Both the single and parallel grating OSCs have a normal incidence $\lambda_{SP} \approx 527$ nm, however

the parallel grating OSC has an additional $\lambda_{SP} \approx 615$ nm attributed to the larger grating spacing (Λ_1). The broadening of the photocurrent response of the parallel grating is centered around this second λ_{SP}.

Figure 4.13 illustrates the relative photocurrent response (parallel OSC/single OSC) at normal incidence for TM polarized incident light. These are the same OSCs as were analyzed in figure 4.12.

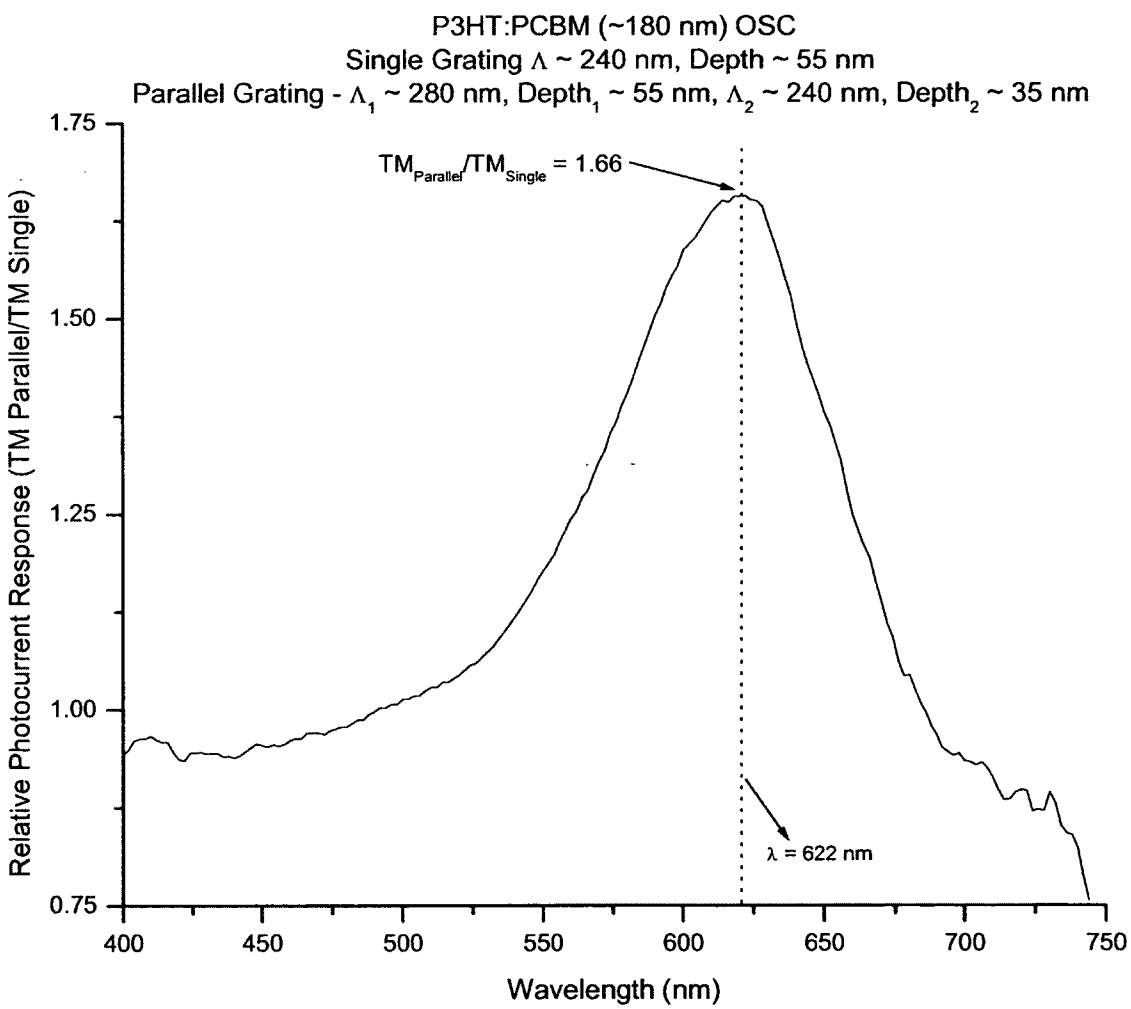

Figure 4.13. Relative photocurrent response of a single versus parallel grating OSC.

As seen in figure 4.13, the maximum relative photocurrent increase is 1.66 at a wavelength of $\lambda = 622$ nm. These results show the net photocurrent enhancement due to the parallel grating (compared to the single grating), and are in good agreement with theoretical predictions. While both the single and parallel grating OSCs show substantial photocurrent enhancements, when compared to one another, it is quite evident that the parallel grating OSC displays an enhanced photocurrent response over a broader range of wavelengths.

REFERENCES

[1] M. Sadiku, Elements of Electromagnetics, 4th Ed., New York: Oxford University Press, 2007.

[2] R. Serway, "Chapter 21: Current and Direct Current Circuits," in *Principles of Physics, 4th Ed.*, Toronto, Thomson Learning, 2006, p. 689.

[3] K. Tvingstedt, N. Persson and O. Inganäs, "Surface Plasmon Increase Absorption in Polymer Photovoltaic Cells," *Applied Physics Letters,* vol. 91, no. 11, p. 113514, 2007.

[4] S. Kim, S. Na, J.Jo, D. Kim and Y. Nah, "Plasmon Enhanced Performance of Organic Solar Cells using Electrodeposited Ag Nanoparticles," *Applied Physics Letters,* vol. 93, no. 7, p. 073307, 2008.

[5] S. Na, S. Kim, J. Jo, S. Oh, J. Kim and D. Kim, "Efficient Polymer Solar Cells with Surface Relief Gratings Fabricated by Simple Soft Lithography," *Advanced functional Materials,* vol. 18, no. 24, p. 3956–3963, 2008.

[6] R. Sabat, M. Santos and P. Rochon, "Surface Plasmon-Induced Band Gap in the Photocurrent Response of Organic Solar Cells," *International Journal of Photoenergy,* vol. 2010, p. 698718, 2010.

[7] K. Le, A. Abass, B. Maes, P. Bienstman and A. Alù, "Comparing Plasmonic and Dielectric Gratings for Absorption Enhancement in thin-film Organic Solar Cells," *Optics Express,* vol. 20, no. S1, pp. A39-A50, 2012.

[8] J. Nelson, "Organic Photovoltaic Films," *Current Opinion in Solid State and Materials Science,* vol. 6, no. 1, pp. 87-95, 2002.

[9] S. Günes, H. Neugebauer and N. Sariciftci, "Conjugated Polymer-Based Organic Solar Cells," *Chemical Reviews,* vol. 107, no. 4, pp. 1324-1338, 2007.

[10] K. Kim, J. Liu, M. Namboothiry and D. Carroll, "Roles of Donor and Acceptor Nanodomains in 6% Efficient Thermally Annealed Polymer Photovoltiacs," *Applied Physics Letters,* vol. 90, no. 16, p. 163511, 2007.

[11] M. Sefunc, A. Okyay and H. Demir, "Plasmonic Backcontact Grating for P3HT:PCBM Organic Solar Cells Enabling Stong Optical Absorption Increased in all Polarization," *Optics Express,* vol. 19, no. 15, pp. 14200-14209, 2011.

[12] A. Moulé and K. Meerholz, "Interference Method for the Determination of the Complex Refractive Index of Thin Polymer Layers," *Applied Physics Letters,* vol. 91, no. 6, pp. 061901: 1-3, 2007.

[13] M. Weber, Handbook of Optical Materials, Boca Raton: CRC Publishing, 2003.

[14] M. Zeman, "Delft University of Technology Solar Cell Course Reading - Chapter 1: Introduction to Photovoltiac Solar Energy," [Online]. Available: http://ocw.tudelft.nl/courses/microelectronics/solar-cells/readings/1-introduction-to-photovoltaic-solar-energy/. [Accessed 20 May 2011].

CHAPTER 5: CONCLUSION

Much research is being conducted on the integration of SP-based systems into existing OSC technologies. The substantial enhancements demonstrated by such systems cannot be ignored. Given that SP excitation can be realized through the addition of a single step to the design and fabrication process, the minimal efforts are well rewarded, with photocurrent enhancements of more than 300% having been demonstrated. Its complimentary nature is intended to improve upon the performance of conventional OSC schemes, and recently, multi-interfaced, SP excitation has been shown for double-layered, grating structures [1]. Integration of such systems within the numerous OSC configurations and architectures, as well as throughout the world of materials science and the ever evolving assortment of suitable organic, photoactive materials, is actively being explored. It is therefore imperative that SPs continue to be studied such that their science can be fully understood and their parameters further optimized in order to maximize potential OSC yields.

Within this thesis, diffraction grating excitation of SPs at various metal-dielectric interfaces has been demonstrated and thoroughly investigated. The fabrication of suitable test samples via the sequential depositing of thin azopolymer, metal, and dielectric layers, and subsequent analysis proved to be much more economical, both in terms of time and effort, compared to that of the OSCs, and thus the test samples served as a simulation tool, designed to better understand and predict SP behaviour. Optical spectral scans were carried out on test samples over various gratings schemes (single, crossed and parallel), grating spacings, grating depths, incidence angles, and film thicknesses. Theoretical predictions of SP behaviour proved to be in good agreement with measured results, with

the discrepancies being attributed to the assumption of non-wavelength dependent metal-dielectric parameters such as dielectric permittivity and refractive index, which were selected based on a central wavelength, as well as the flat-interface approximation, used to examine all metal-dielectric interfaces. The assumption of no losses also factored into these discrepancies. While absolute precision of SP behaviour was not essential throughout this thesis, improved computer-based, modeling tools incorporating the frequency dependent parameters, as well as accounting for the non-flat, interface, would indeed serve to expedite and more accurately predict SP behavior.

From these metal-dielectric test sample simulations, optimal parameters satisfying fixed criterion for SP excitation were determined. These parameters included grating spacings, depths, and film thicknesses, and were incorporated into the subsequent OSC design and fabrication process. A single, P3HT:PCBM, photoactive layer was sandwiched between two harvesting electrodes, with aluminum being used as the bottom electrode, and gold being used as the top electrode. The sandwiched architecture and photoactive and electrode materials used within the OSC were drawn from an existing design [2]. The aluminum electrode assumed the shape of single, crossed and parallel diffraction gratings of pre-determined spacing and depth. Optical spectral scans were carried out on OSCs structured on all grating schemes (single, crossed and parallel), as well as over various grating spacings and incidence angles.

Photocurrent enhancements were indeed demonstrated for each grating scheme. Enhancements shown on both single and crossed grating, SP-based, OSCs were in agreement with existing research studies [2], [3], [4], [5], with obvious increases for TM polarized incident light being present on single grating structures, and similar increases

for both TM and TE polarized incident light being present on crossed grating structures. Enhancements shown on parallel grating, SP-based, OSCs are believed to be novel, since no related existing research literature could be found. Substantial photocurrent enhancements on parallel grating, OSC structures were clearly demonstrated. When compared to the increases seen on single grating structures, those seen on parallel gratings were comparable in magnitude, but shown over a much broader optical band. This broadening of the optical band was centered on the theoretical SP resonance peak of the additional (second) grating contained within the parallel scheme. It is believed that the existence of this additional grating, accounts for the broader photocurrent enhancements seen within parallel grating structures.

Future considerations for work in SP-based systems include exploration of a blazed grating scheme for SP excitation. Blazed gratings shift the diffraction envelope maximum to a non-0th diffraction order, theoretically making improved SP excitation possible. Such studies could also focus on the efficiency with which various grating profiles excite SPs. Additional research focusing on SP-based systems structured on diffraction gratings of smaller spacings would also allow photocurrent enhancements to be exploited over the lower portion of the P3HT:PCBM absorption spectra. In this thesis, laser and writing angle limitations restricted grating spacings to a minimum of $\Lambda \approx 240$ nm. Lastly, the incorporation of standardized SC measuring parameters such as open circuit voltage, short circuit current, fill factor, etc into experimental results would be beneficial in the sense it would allow for direct comparisons to existing solar cell systems.

REFERENCES:

[1] N. Anttu, Z. Guan, U. Håkanson, H. Xu and H. Xu, "Excitations of Surface Plasmon Polaritons in Double Layer Metal Grating Structures," *Applied Physics Letters,* vol. 100, no. 9, pp. 091111-1-091111-3, 2012.

[2] R. Sabat, M. Santos and P. Rochon, "Surface Plasmon-Induced Band Gap in the Photocurrent Response of Organic Solar Cells," *International Journal of Photoenergy,* vol. 2010, p. 698718, 2010.

[3] K. Tvingstedt, N. Persson and O. Inganäs, "Surface Plasmon Increase Absorption in Polymer Photovoltaic Cells," *Applied Physics Letters,* vol. 91, no. 11, p. 113514, 2007.

[4] K. Le, A. Abass, B. Maes, P. Bienstman and A. Alù, "Comparing Plasmonic and Dielectric Gratings for Absorption Enhancement in thin-film Organic Solar Cells," *Optics Express,* vol. 20, no. S1, pp. A39-A50, 2012.

[5] M. Sefunc, A. Okyay and H. Demir, "Plasmonic Backcontact Grating for P3HT:PCBM Organic Solar Cells Enabling Stong Optical Absorption Increased in all Polarization," *Optics Express,* vol. 19, no. 15, pp. 14200-14209, 2011.

BIBLIOGRAPHY

J. Bittencourt, The Fundamentals of Plasma Physics, New York: Springer-Verlag, 2004.

E. Hecht, Optics, 4th Ed., San Francisco: Pearson Addison-Wesley, 2002.

J. Lourtioz, H. Benisty, D. Pagnoux, V. Berger, J. Gerard and D. Maystre, "Photonic Crystals: Towards Nanoscale Photonic Devices, 2nd Ed.," Springer-Verlag, Berlin, 2008.

L. Novotny and B. Hecht, Principles of Nano-Optics, Cambridge: Cambridge University Press, 2006.

C. Palmer, Diffraction Grating Handbook, 5th Ed., Rochester: Richardson Grating Laboratory, 2002.

F. Pedrotti, L. Pedrotti and L. Pedrotti, Introduction to Optics, 3rd Ed., San Francisco: Pearson Addison-Wesley, 2007.

H. Reather, Surface Plasmons on Smooth and Rough Surfaces and on Gratings, London: Springer-Verlag, 1988.

M. Sadiku, Elements of Electromagnetics, 4th Ed., New York: Oxford University Press, 2007.

D. Sarid and W. Challener, Modern Introduction to Surface Plasmons, Cambridge: Cambridge University Press, 2010.

R. Serway, Principles of Physics, 4th Ed., Toronto: Thomson Learning, 2006.

A. Tudos and R. Schasfoort, Handbook of Surface Plasmon Resonance, Cambridge: The Royal Society of Chemistry, 2008.

M. Weber, Handbook of Optical Materials, Boca Raton: CRC Publishing, 2003.

CURRICULUM VITAE

Justin Jefferies was born in Gander, NL on 29 June 1983 and grew up in Charlottetown, a small community located on the south-east coast of Labrador. During his senior year of high school in 2001, Justin was accepted into the Regular Officer Training Program at the Royal Military College of Canada (RMC) in Kingston, ON, where he earned a four-year undergraduate degree in Electrical Engineering.

Upon graduation from RMC in 2005, Justin began his career as an Aerospace Engineering (AERE) Officer. As a Second-Lieutenant, he split one year between 8 Air Maintenance Squadron (Sqn) in Trenton, ON and 435 Sqn in Winnipeg, MB gaining experience on the CC130 Hercules platform, before undertaking the AERE course in Borden, ON.

Following successful graduation from the AERE course in 2008, Justin was posted to 442 Search and Rescue (SAR) Sqn as the Deputy Aircraft Maintenance Officer for the fixed-wing, CC115 Buffalo fleet. During his time at 442 Sqn, Justin also served as the Sqn's Quality Manager, and was involved in the planning and execution of the Buffalo Avionics Life Extension modification, as well as the flight operations for the 2010 Vancouver Olympics.

Since 2010 Justin has been living in Kingston, ON with his wife, Courtney, and two daughters, Siena and Adley, where he has been undertaking a Master's of Science degree in Physics.